



Studies of steered arc motion and macroparticle production in PVD processing.

CRAVEN, Adrian Lewis.

Available from the Sheffield Hallam University Research Archive (SHURA) at:

<http://shura.shu.ac.uk/19510/>

A Sheffield Hallam University thesis

This thesis is protected by copyright which belongs to the author.

The content must not be changed in any way or sold commercially in any format or medium without the formal permission of the author.

When referring to this work, full bibliographic details including the author, title, awarding institution and date of the thesis must be given.

Please visit <http://shura.shu.ac.uk/19510/> and <http://shura.shu.ac.uk/information.html> for further details about copyright and re-use permissions.

LEARNING CENTRE
CITY CAMPUS, POND STREET,
SHEFFIELD, S1 1WB.

101 617 344 X



REFERENCE

ProQuest Number: 10694391

All rights reserved

INFORMATION TO ALL USERS

The quality of this reproduction is dependent upon the quality of the copy submitted.

In the unlikely event that the author did not send a complete manuscript and there are missing pages, these will be noted. Also, if material had to be removed, a note will indicate the deletion.



ProQuest 10694391

Published by ProQuest LLC (2017). Copyright of the Dissertation is held by the Author.

All rights reserved.

This work is protected against unauthorized copying under Title 17, United States Code
Microform Edition © ProQuest LLC.

ProQuest LLC.
789 East Eisenhower Parkway
P.O. Box 1346
Ann Arbor, MI 48106 – 1346

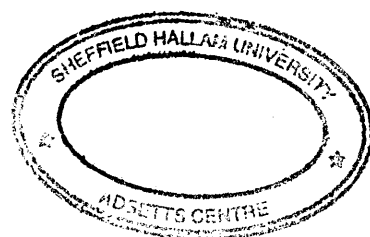
Studies of steered arc motion and macroparticle production in PVD processing

Adrian Lewis Craven, BSc(Hons)

A thesis submitted in partial fulfilment of the requirements of
Sheffield Hallam University
for the degree of Doctor of Philosophy

March 2000

The Materials Research Institute, Sheffield Hallam University



Abstract

During the past decade the production industry has constantly strived to improve performance and cut costs, this has been aided by the development of high performance tools. The advancement of these tools has been accomplished by the application of hard wearing, low friction, coatings. A key process in the production of such coatings is Physical Vapour Deposition(PVD). Interest in such thin films has led to much research effort, both academic and industrial, being devoted to the area. In order that these advancements in technology continue, research into the fundamental aspects of PVD is required.

This thesis describes research and experimental studies which have been performed to study the effect of "steering" an electric arc on various aspects of its behaviour. "Steering" of the arc is achieved by applying external magnetic fields which allow the guidance of the path of the arc. Work by earlier authors has aimed to control the arc more fully. The research presented here is based on a novel electromagnetic three coil steering array of cylindrical geometry. With such coils it is possible to vary the field profiles to a greater degree than has been previously achieved, permitting a greater range of steering arrangements/fields to be applied. The research presented is divided into two distinct areas:

Firstly a number of experiments were performed to assess the effectiveness of the new steering coils on the motion of the arc. A personal computer was used here along with new arc motion monitoring electronics. This enabled the simultaneous measurement of the orbital transit times and also the degree of travel perpendicular to the steered direction of motion of the arc, as it traversed the surface of the cathode. Such information was then used to produce values for standard deviation of the arc from its steered path, velocity of the arc and a diffusion constant related to the motion of the arc. Such values then allowed evaluation of the stochastic model of arc motion proposed by Care[†].

Secondly the effect of changes in magnetic field on the production, ejection angle and size of macroparticles (small molten droplets of the cathode material) was studied. This was accomplished by the design, production and usage of new sample holding equipment. This equipment allowed the coating of highly polished samples at a number of angles in relation to the cathode, with all samples being held equidistant from the arc track. Once such sample coatings had been produced they were then analysed using a Scanning Electron Microscope(SEM) to give macroparticle density figures.

Acknowledgements

Firstly I would like to thank my supervisory team at the University, Dr R New, Professor C M Care and Dr J Cawley, for their time in the form of discussions and English lessons. Of the above I would like to single out Dr R New for special thanks as all along he provided me with encouragement and helpful advice and never gave up on me. I would also like to thank Messrs R Day and G Robinson for making mechanical masterpieces out of my scribbings, all the technical staff in the Division of Applied Physics and the MRI. In addition I would like to acknowledge the part of my fellow PhD researchers for making my time such a memorable one.

I would also like to thank the myriad of organisations(too many to list) who made the conference visit possible by sponsoring me.

Finally I would like to acknowledge my family for supporting my endeavours during this long struggle, from my Granny who never gave up, to my Mum who has helped so immensely during my life and my Father(deceased) who sadly did not live to see what an achievement I have made.

Contents

Chapter One:	INTRODUCTION TO PHYSICAL VAPOUR DEPOSITION	1
1.1	Arc Coating Methods	
1.1.1	Random arc	
1.1.2	Steered arc	
1.2	Present Work	
Chapter Two:	ARC MOTION	9
2.1	The Cathode Spot	
2.1.1	What is the cathode spot	
2.1.2	Life cycle of the cathode spot	
2.1.3	Type of spots	
2.1.4	Size and current density of a cathode spot	
2.1.5	Experimental data on spot motion	
2.2	Models Of Arc Motion	
2.2.1	Motion of the cathode spot considered as a random walk	
2.2.2	motion of the cathode spot under the influence of a magnetic field	
Chapter Three:	MACROPARTICLES	38
3.1	What Are Macroparticles	
3.2	Reduction/ Removal Of Macroparticles	
3.2.1	Reduction of macroparticles	
Chapter Four:	EXPERIMENTAL SETUP	52
4.1	Development Of Electromagnetic Control Of The Arc	
4.1.1	Control of the arc	
4.1.2	The two coil electromagnetic steering array	
4.1.3	The three coil electromagnetic steering array	
4.2	Development Of New Hardware For The Vacuum Rig	
4.2.1	The three coil electromagnetic steering array	
4.2.2	Water cooled anode	
4.2.3	Substrate shield	
4.2.4	Water cooled substrate holder	

- 4.3 Apparatus Used
 - 4.3.1 Main chamber and pumping system
 - 4.3.2 The power supplies
 - 4.3.3 The gas control system

Chapter Five: EXPERIMENTAL STUDIES OF ARC MOTION

76

- 5.1 Introduction To The Stochastic Model
- 5.2 Analysis Of The Arc Motion
- 5.3 Measurement Of The Arc Confinement
 - 5.3.1 Introduction
 - 5.3.2 Experimental details
 - 5.3.3 Results
- 5.4 Measurement of The Distribution Of Orbital Transit Times
 - 5.4.1 Introduction
 - 5.4.2 Experimental details
 - 5.4.3 Distribution of spot transit times
 - 5.4.4 Fitting of the data to the theoretical distribution
 - 5.4.5 Results

Chapter Six: EXPERIMENTAL STUDIES OF MACROPARTICLE DISTRIBUTION

118

- 6.1 Method Of Investigation
- 6.2 Sample Preparation
- 6.3 Analysis Method
 - 6.3.1 Modes of operation of the SEM
- 6.4 Analysis Of Macroparticle Properties
 - 6.4.1 Angular distribution
 - 6.4.2 Size distribution
- 6.5 Experimental Results
 - 6.5.1 Angular distribution
 - 6.5.2 Size distribution

Chapter Seven: SUMMARY AND FURTHER WORK

139

- 7.1 Summary Of Results Presented
- 7.2 Recommendations For Further Work

Appendix A:	MATHEMATICS OF THE THREE COIL ELECTROMAGNETIC STEERING ARRAY	146
Appendix B:	PROGRAM DOCUMENTATION	150
Appendix C:	DESIGNS FOR ADDITIONAL EQUIPMENT FOR THE VACUUM SYSTEM	175

1.0 INTRODUCTION TO PHYSICAL VAPOUR DEPOSITION

Industry constantly demands improvement in components whether it be cosmetic or performance related. To satisfy these demands scientists and engineers have devised numerous methods of producing coatings, Fig 1.1, each with different areas of usage and expertise.

One main area of research, at present, is centred on the use of such coating system to produce films which will allow components to operate under extreme conditions, e.g. drills and dies. The idea being that by modifying the surface, using a film, it is possible to produce a resultant tool which performs better than a piece consisting of either the substrate or coating material alone[2].

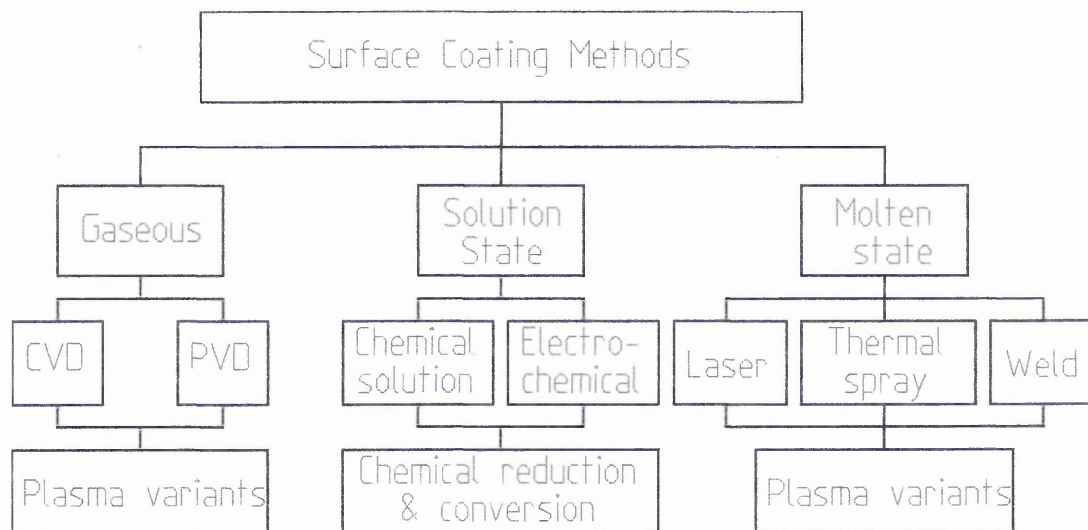


Fig 1.1, Schematic illustrating the different methods of producing coatings, after [1]

The coating methods shown in Fig 1.1 are categorised into three broad areas. These

three methods of coating can be classified into two types of coating production as shown below:

"Wet treatments" – Solution state

Currently the usage of these methods is vast, ranging from painting to electroplating systems. They show good reliability and reproducibility, but do have environmental problems.

"Dry treatments" – Gaseous and molten states

Such methods have been developed over the past 30 years and use mainly plasmas to deposit the materials. Their main advantage is that the coating composition and growth rate can be controlled, which is critical for the areas of usage e.g. semiconductor industry. The majority of these processes involve treatment under vacuum in the presence of either a reactive or inert gas, meaning a wide range of coatings can be achieved.

One such method of producing the coatings is physical vapour deposition(P.V.D). PVD has been used since the 1970's to produce metal films for coating tools[4,5]. Although, as mentioned above, the main purpose of the process is to increase efficiency and longevity of work pieces, other areas such as decorative finishes are also possible. Uses for such coatings range from spectacle frames to CDs and turbine blades to drill bits, showing that this technique generates a wide range of products. The term PVD encompasses a large variety of coating mechanisms which all have a common element, they are performed under partial vacuum, Fig 1.2. The type of process investigated in this thesis is called cathodic arc, or sometimes vacuum arc, PVD and uses a high current low voltage electrical discharge to evaporate the cathode material.

The first coatings produced using cathodic arc PVD had one distinct disadvantage, the incorporation of droplets of cathode materials in the film. These droplets, usually referred to as macroparticles, are produced when the arc interacts with the cathode surface. Due to the nature of the arc a large current density is brought to bear on a very small area of the cathode leading to a rapid rise in the local surface temperature, thus vaporising the cathode material. A high velocity jet is produced containing macroparticles, metal ions and neutrals, see Fig 1.3. If the macroparticles are enclosed in

the subsequent coating then degradation and premature failure of the film and work piece can occur.

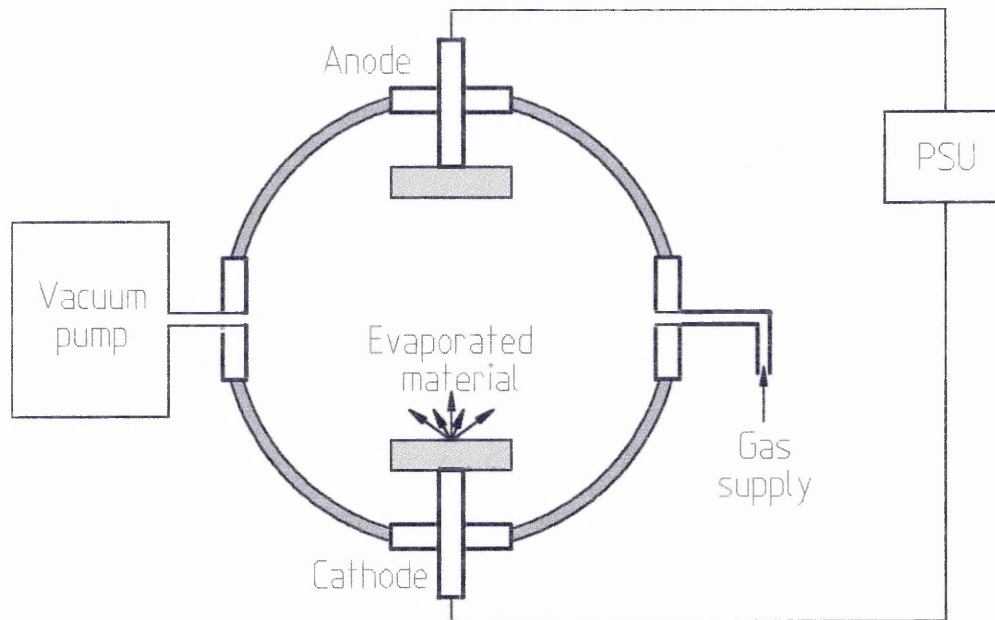


Fig. 1.2, Sketch of a PVD system, after [3]

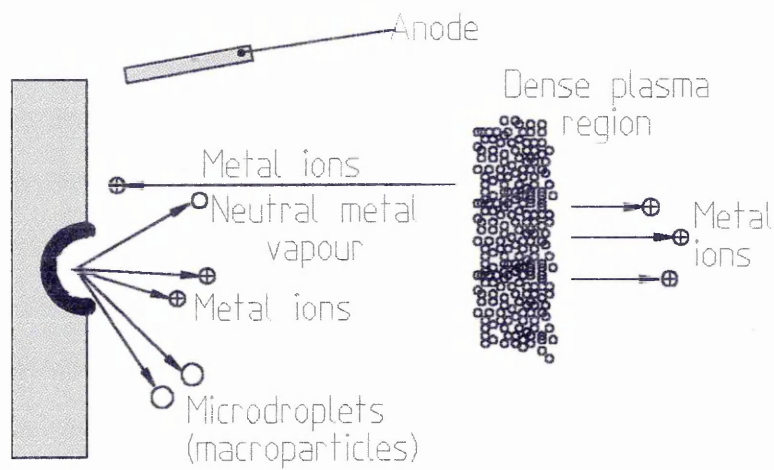


Fig 1.3, Illustration of the elements produced by an arc discharge

1.1 Arc Coating Methods

There are two coating techniques which utilise the cathodic arc. They are named according to the arc motion employed to evaporate the cathode, random and steered.

1.1.1 RANDOM ARC

The random arc method involves the striking of an arc on the cathode and allowing it to traverse the surface freely. This technique was developed in the United States[6] and the Soviet Union[5] in the early 1970's and was used to produce hard, durable and well adhered thin films. Unfortunately the use of this process is limited by the fact that the arc is not guided and can therefore dwell on some spots longer than others. This extra time spent evaporating the cathode leads to an increase in the production of macroparticles. The random movement of the arc also means that the ion flux from the cathode spot varies, leading to problems with the production of reliable uniform compound films.

1.1.2 STEERED ARC

Here the motion of the arc is controlled by an externally applied magnetic field produced by permanent magnets and/or electromagnets(see chapter 4 for more detail). The magnetic field forces the arc to follow a certain path, as well as affecting the velocity at which the arc moves. Some aspects of this control are understood whereas others; such as retrograde(non amperian) motion are not. The aims of this thesis are to improve the understanding of the influence of the magnetic fields on the motion of the arc and to investigate the effect of the fields on the macroparticle production rate (see chapter 3).

Ramalingham[7] used a permanent magnet placed behind the cathode to gain control of the arc. Interatom later developed this idea attaching the magnet to an arm and rotating it, using a motor, behind the cathode. Such a system increased cathode usage by producing a rosette pattern on the surface of the cathode(Fig 1.4). Further developments, by Morrison[8], led to the use of electromagnets to steer the arc. He developed a system which could move the arc along a rectangular trajectory, Fig 1.5, this

arrangement proved much more robust as there were no mechanical movements involved.

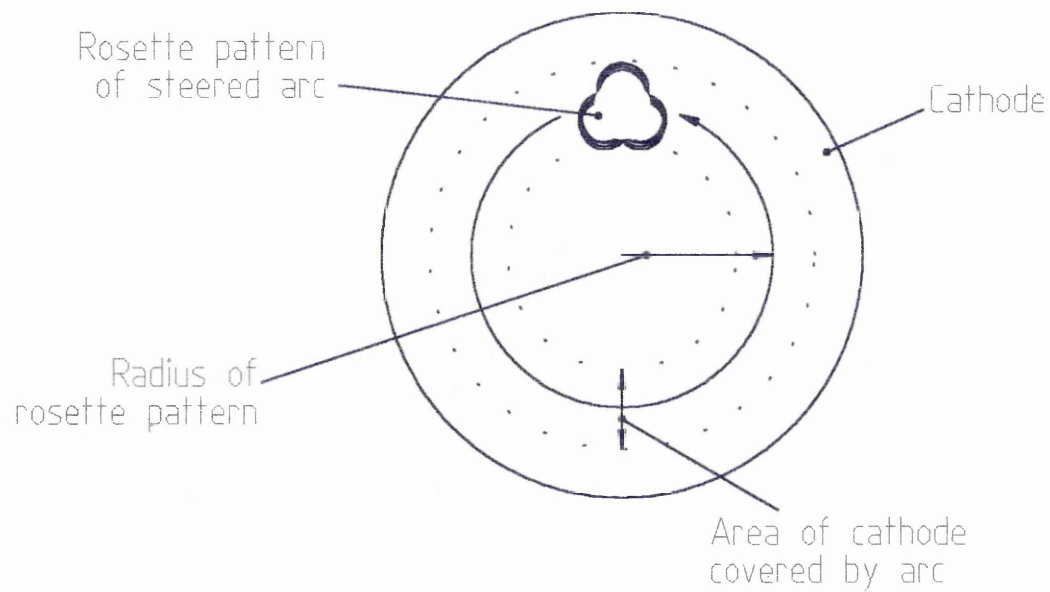


Fig 1.4, Sketch of the path followed by the arc on the surface of the cathode

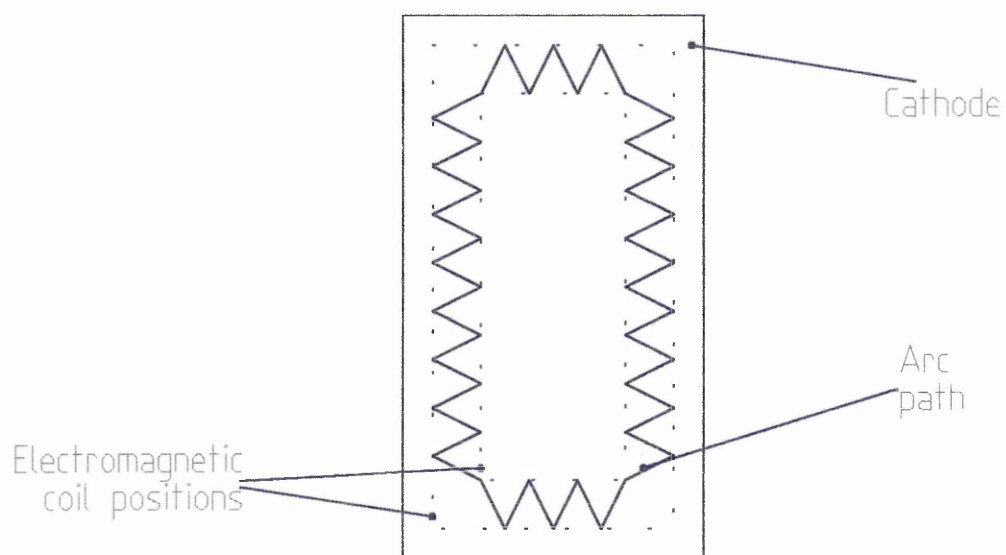


Fig 1.5, Sketch of the path of the arc in the Morrison system

1.2 Present Work

There are two main areas covered by work in this thesis. The first involves the investigation of the cathode spot under the influence of a magnetic field. This work is required as at present our knowledge of the importance of certain parameters is incomplete. There are many mathematical and phenomenological models of arc motion which try to explain the nature of the cathode spot and how it moves around the cathode. To fully assess the validity of these models we need to investigate certain areas further. Using the experimental results obtained it is possible to test these models. Secondly work has been undertaken to study the production and distribution of macroparticles as a function of magnetic field.

Considering the information presented here and the review of current literature(chapters 2 and 3), the following areas were identified which required further research:

- i. To develop novel electromagnetic steered arc control system, which will allow a greater degree of control to be exerted on the motion of the arc. The system allows a degree of independent variation of confinement, orbital velocity and orbital radius.
- ii. To use this steering system to perform experiments to determine certain spot parameters, such as spot confinement and velocity distributions.
- iii. To compare the experimental data with model predictions, for example those of Care[9], to give a clearer understanding of the effect of various elements of the magnetic field upon cathode spot parameters.
- iv. To use the steering array to perform experiments to determine the angular and size distributions of macroparticles as a function of spot parameters, and magnetic field.

This thesis describes the work performed in the above areas and is organised as follows:

- Chapter 2 is a review of the current literature regarding experimental knowledge of the cathode spot, including areas such as spot lifecycle, size and current densities and also mathematical models of arc motion.

- Chapter 3 is a review of macroparticle production. This chapter examines experimental data from current literature regarding the production of macroparticles, as well as operational parameters which affect this process.
- Chapter 4 is a description of the development of the experimental apparatus. Firstly the evolution of the novel steering array, including the design and implementation, and secondly the design and use of other new hardware developed to facilitate this research. Finally there is a description of the experimental system used, including details of the main chamber pumping system, power supplies used and details of the gas control system utilised in these experiments.
- Chapter 5 consists of a description of arc monitoring equipment used for this research, along with the results which were obtained from experiments. The results are then compared with those predicted by the model of Care[9].
- Chapter 6 consists of an explanation of the methods used to study the production of macroparticles, as well as the experimental results obtained.
- Chapter 7 contains a summary of the literature reviewed, research performed and conclusions drawn from this work. Finally suggestions are made of relevant areas for further research.

REFERENCES

- [1] L A Donohue
PhD Thesis, Sheffield Hallam University (1995)

- [2] D S Rickerby, A Mathews
"Advanced Surface Engineering", Blackie press (1991)

- [3] P J Walke
PhD Thesis, Sheffield Hallam University (1994)

- [4] Vacuum arcs, theory and applications
J M Lafferty(editor), Wiley Interscience (1980)

- [5] L P Sablev
US Patent No. 3, 783, 231 (1974)

- [6] A A Snaper
US Patent No.'s 3, 625, 848 (1971), 3, 836, 451 (1974)

- [7] S Ramalingham
US Patent No. 4, 673, 477 (1987)

- [8] J R Morrison
US Patent No. 4, 724, 058 (1987)

- [9] C M Care
Journal of Physics D: Applied Physics 25(12) (1992) 1841

2.0 ARC MOTION

Over the past few decades many authors[1, 2 ,3 , 4] have studied the motion of the cathode spot and a large amount of experimental data has been compiled. Unfortunately there are discrepancies between some experimental parameters measured by different authors. This is probably due to experimental difficulties associated with small spot size, high spot velocities and the obstruction of the view of the cathode spot which the plasma cloud causes.

This chapter summarises the experimental work performed in the field and covers a range of areas including:

- Spot life cycle
- Types of cathode spot observed
- The size and current density of the cathode spot
- Spot splitting
- Spot motion
- Models of arc motion

2.1 The Cathode Spot

2.1.1 WHAT IS THE CATHODE SPOT ?

“Cathode spot” is the term given to the point where the arc touches the cathode surface. This small area is heated, due to large current densities, emitting metal vapour into a cloud above the spot. As time passes the cathode is continuously eroded and a crater is formed. At some time the spot dies and another is formed.

2.1.2 LIFE CYCLE OF CATHODE SPOT

Guille and Jüttner [5] reviewed the life cycle of the cathode spot and suggested that it may be divided into four stages, as shown diagrammatically in Fig 2.1 and described as follows:

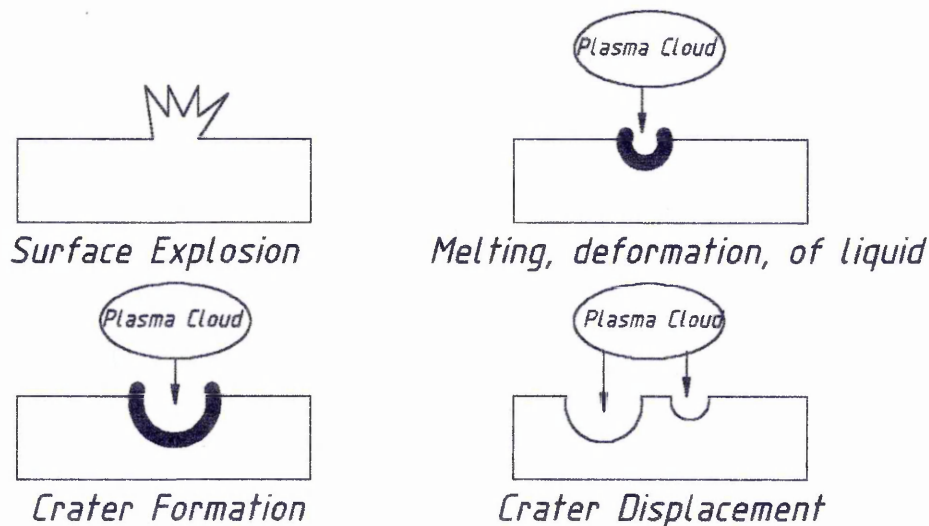


Figure 2.1, Diagrammatic representation of the life cycle of a cathode spot after[5]

(a) Surface Explosion

When a large potential is applied between the anode and the cathode this gives rise to the electrical breakdown of the vacuum and current flows to the cathode. Such a current leads to the rapid heating and evaporation of the surface, thus creating a plasma cloud. It is widely thought[6, 7, 8] that the arc is maintained by field emission, though it has been observed that the macroscopic field breakdown occurs at two orders of magnitude below the value at which the field emission would be expected to begin. It has also been noted that experiments using identical settings can produce differing breakdown voltages, these differences can be explained by one or both of the following:

- i) Since the surface of the cathode is not flat, but is instead made up of micro protrusions, at the tip of these micro protrusions the field will be intensified[9]. Hence this enhancement factor could be sufficient to provide the field gradients required for field emission.
- ii) The adsorption of gases from the chamber by the cathode will affect the work function of the cathode and thus increase the chance of electron emission.

(b) Melting and Deformation of the Liquid

The above leads to one of two outcomes, either the protrusion is totally obliterated leaving a flat surface, meaning that the plasma pressure alone creates a crater [5,10], alternatively the explosion could leave remnants of the protrusion. Ecker [11] believes that a combination of the plasma pressure and the surface tension then act on the remains of the protrusion to destroy it, leaving a molten pool which could be moved by the plasma pressure.

(c) Crater Formation and Steady State Operation of the Spot

The preceding steps represent only a small fraction of the lifetime of the emission site. Initially it is the pressure of the plasma which exerts itself on the surface of the cathode creating a crater, then most of the time is taken by evaporation of the cathode surface into the plasma cloud above it.

A considerable ion flux is emitted by the spot and most of the ions are multiply charged[12]. Plyutto [13] also observed that the ions emitted in the flux leaving the surface had larger energies than expected. There are 2 models which describe this anomaly, the Potential Hump model [14] and the Gas Dynamic model [15]. Both models are described by Sanders et al [16]. Experimentally neither totally explains the exact behaviour, but a combination of the two causing an averaging effect may provide a better description.

(d) Crater Displacement

Ecker [11] suggested that the creation of a new spot was due to localised heating of the cathode, causing a change in the resistance. At some time this resistance increases to such a level that a new site becomes more favourable. The new site will then begin to feed the plasma cloud until such time that the cloud moves and the old site extinguishes,

not having sufficient current density to evaporate any more material, and then the cycle repeats itself.

A more in depth review of the life cycle of a cathode spot can be obtained from the thesis of P Walke [17].

2.1.3 TYPES OF SPOTS

Rahkovskii et al[1] and also Jüttner et al[4] were the first to identify that there were two different “types” of spot, and have been supported by the experimental work of other authors[2, 3, 18, 19]. The existence of the two Types of cathode spot is of great importance when considering experimental data as the size, behaviour and appearance of the two Types are very different. The following are descriptions of the two Types of spots.

Type 1 Spot

Lyubimov and Rahkovskii[1] noted that a Type 1 spot only appears on "new" cathodes, and that it does not exhibit a high erosion rate. Bushik et al[2] believed that this description of the cathode spot was not accurate enough and added that the discharge was fed by absorbed gases such as hydrocarbons, water vapour, oxides, and gave supporting experimental evidence. This research consisted of "arcing" the cathode until no Type 1 spots were visible, then exposing the cathode to air for a short time followed by a return to vacuum. It was found that when an arc was struck on the exposed cathode then the Type 1 spots had reappeared.

The motion of Type 1 spots on the cathode is erratic as it jumps from site to site, with the distance between sites being larger than the radius of the crater produced by the cathode spot. It should also be noted that Type 1 spots do not emit light which is of the characteristic colour of the cathode material.

Type 2 Spot

Type 2 spots gradually appear on a cathode as it is being "arc cleaned" and coexist with Type 1 spots during this phase. Fang[20] noted that it took approximately 100 discharges for the velocity of the arc to reach a steady state value, indicating that the surface of the cathode had been purged of impurities. Type 2 spots have a higher erosion rate as they use thermal processes to evaporate the surface of the cathode, emitting a glow of a colour characteristic of the cathode material.

The spot traverses the cathode with a lower velocity than that of a Type 1 spot, since now the arc moves a distance of approximately the crater radius resulting in less erratic motion of the arc across the cathode.

More details on the two Types of cathode spot can be obtained from other literature[1, 2, 3, 4, 21].

2.1.4 SIZE AND CURRENT DENSITY OF A CATHODE SPOT

Size and current density of the spot are interrelated as the current density depends directly upon the active area of the cathode spot. The size of the spot is still a matter of contention as the two main methods by which its diameter has been measured give conflicting results:

a) Autograph Method[22, 23] - Here the tracks left by the arc on the surface of the cathode are measured and the width taken as the diameter of the cathode spot. This measurement has an inherent disadvantage as it cannot be performed in situ in the vacuum chamber, but it does have the highest resolution ($<0.1\mu\text{m}$).

b) High Speed Photography Method[3,24] - As the name suggests a high speed camera is used to capture the motion of the arc spot as it moves around the surface of the cathode. Using this method the luminous area is assumed to be the spot and can be measured. The resolution of this method is not as good as the first method being, $>10\mu\text{m}$ with framing speed of approximately 10ns. Authors using this technique believe it to be superior to the autograph method because the size of the spot is determined

directly from the image of the spot, as opposed to measuring the tracks left in the surface of the cathode.

Jüttner et al [25] proposed yet another way to determine the current density of the cathode spot. This method involves the measurement of the change of the arc current signal as it crosses a slit in the cathode. When this change was combined with measurement of spot velocity an estimate of the current density was produced which was of the same order as that obtained using the autograph method.

The two main methods of measuring the diameter of the cathode spot give rise to significantly different values; 10^{-5}m using the autograph method and 10^{-4}m using the high speed photography. This difference leads to estimates of current densities which range from 10^{11} to 10^{12}Am^{-2} and 4×10^8 to 10^{10}Am^{-2} . Greater detail into the search for the true spot size can be obtained from Daalder [22].

Spot Splitting

In 1970 Djakov and Holmes[26] presented observations which suggested that the spot was not a single entity but was instead made up of a number of smaller micro spots. Later[27] Djakov and Holmes studied the onset of spot splitting in a range of metals. It was noted that as the current increased then so did the number of spots as shown in Fig 2.2(a). Their results also indicated that the current at which the spot began to split was linked to the boiling point of the cathode material being used as shown in Fig 2.2(b). It was also noted that the "micro" spots initially tended to be clustered together, though as time evolved then they would spread out in a circular path. Djakov and Holmes explained this motion as each individual micro spot moving under the influence of its neighbours. It was thought that the cathode spot did not in fact move but instead the continual extinguishing and reigniting of new sites gave the impression of motion of the spot as a whole. Sherman et al [33] agreed with this idea and added that spots tend to cluster at positions where the azimuthal field was low, but noted that the confinement was not perfect. Harris [4] also treated the spot as consisting of a number of small plasma disks hovering a very small distance from the surface of the cathode.

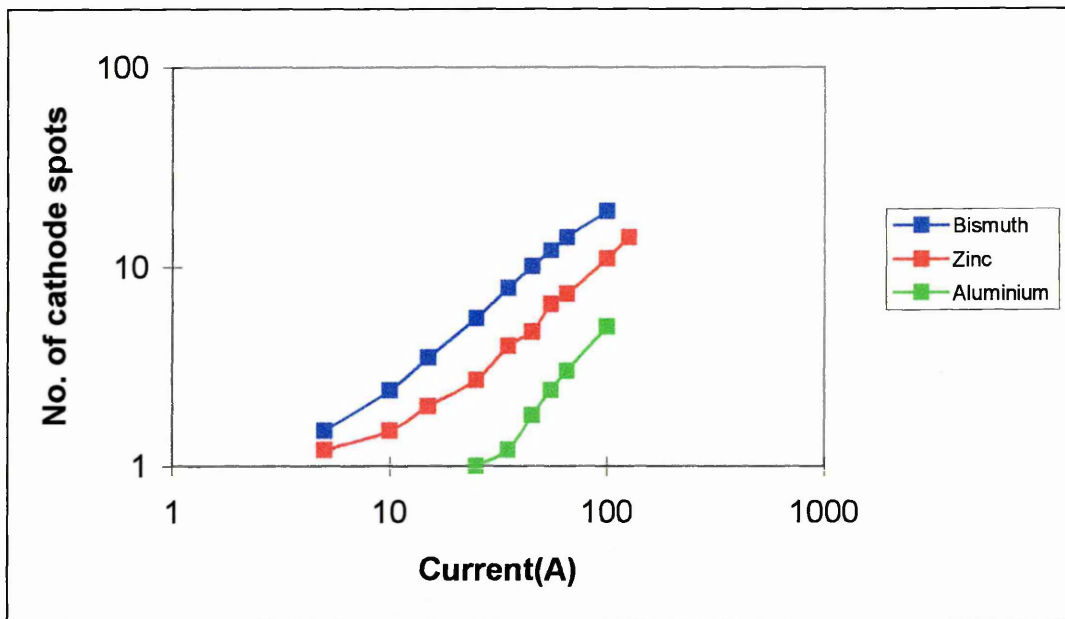
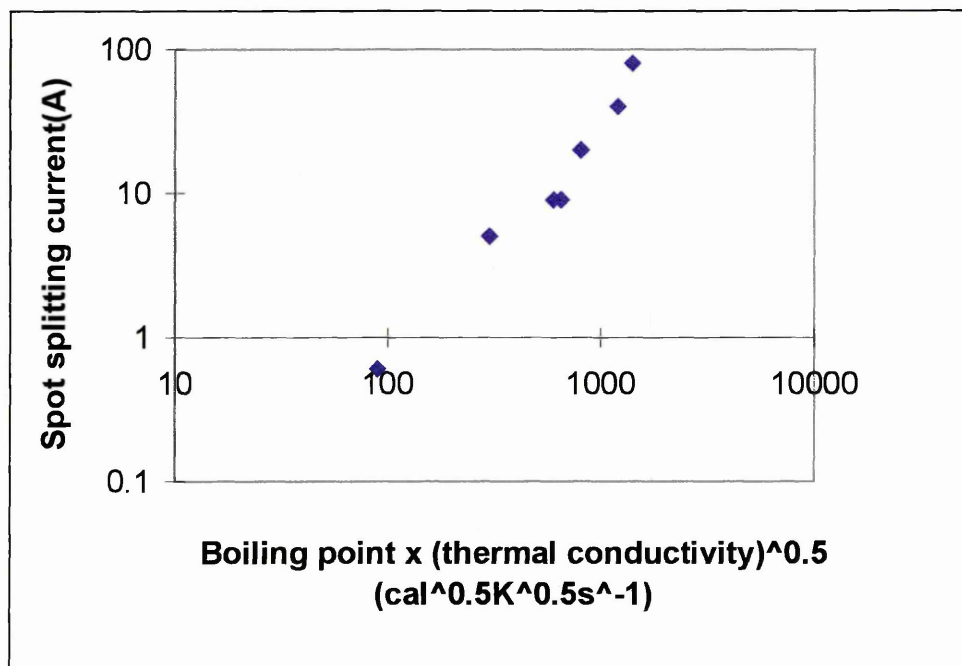


Fig 2.2(a), Plot of arc current vs. number of spots after[27]

Fig 2.2(b), Plot of spot splitting threshold current vs. thermal properties of cathode material after[27]



2.1.5 EXPERIMENTAL DATA ON SPOT MOTION

The aim of this section is to introduce the reader to the movement of the cathode spot around the surface of the cathode. The following are the most relevant experimental observations in the context of this thesis.

Random Arc Motion

This type of motion occurs in the absence of externally applied magnetic fields. The term random walk is used to describe the erratic movement of the arc as it traverses the surface of the cathode. Random arc operation is commonly used in commercial systems as a method of cleaning the surface of the cathode prior to a coating process being started.

Both Hantzche et al[28,38] and Daalder[39] treated the motion of the cathode spot as a random walk and produced the same expression/model, for the motion of the arc, independently of each other. Their models incorporated a spot diffusion constant whose value is dependent upon two parameters, the mean crater radius and a constant of spot displacement. A more detailed explanation of these models can be seen in 2.2.1. Equation 2.1 is an expression for the diffusion constant when considered in two dimensions

$$\alpha = \frac{(s')^2}{2\tau} \quad \text{EQ 2.1}$$

where s' is the mean spot displacement in two dimensions and τ is the mean elementary time step. Hence the diffusion constant increases for larger crater radii.

The expression for α can be further expanded if we assume that s' is proportional to the crater radius, r , i.e.

$$s' = \gamma r, \quad \text{where } \gamma \text{ is the constant of spot displacement}$$

Substituting this expression for s' into EQ 2.1 gives

$$\alpha = \frac{\gamma^2 r^2}{2\tau} \quad \text{EQ 2.2}$$

Hence if r , α and γ are known then an estimate of the spot life can be obtained. The values used for γ in EQ 2.2 were disputed by Hantzche, Jüttner[28] and Daalder[29] due

to different experimental arrangements. It appears that the major disagreement is on spot displacement, which it seems is strongly linked to the surface contamination.

Steered arc motion

The term steered arc is applied to the motion of the cathode spot under the influence of an external magnetic field. It is well known, e.g. [30], that between certain ranges of chamber pressure and magnetic field that the arc moves in the retrograde, non amperian, direction i.e. in the direction of $-\underline{j} \wedge \underline{B}$.

Velocity of the arc

The velocity at which the arc traverses the surface of the cathode has been found to be dependent upon a number of parameters. During the 1950's Galagher[31], working with a mercury pool cathode(and other materials), defined three parameters to which the velocity of the arc was related:

- *GAS PRESSURE*

As mentioned previously, between certain pressures the arc moves in the retrograde direction. Galagher noted that the velocity decreases linearly with respect to an increase in the chamber pressure. If however a threshold level was reached then the arc would revert to motion in the amperian direction. He used a variety of different cathode materials, and backing gases, and found that this threshold level was dependent upon the type of cathode used. This point is also illustrated by work performed by Drouet[32] in which the pressure of the background gas, argon, was increased and changes in the velocity noted.

- *SPECIES OF BACKING GAS*

Galagher also found that the type of backing gas being used sharply affected the pressure at which the arc's motion was reversed. From his experiments it was possible to plot the reversing pressure of the arc vs. the first resonance potential, Fig 2.3, where the first resonance potential is taken as a rough estimate of the cathode voltage drop. As can be seen there is a considerable difference between the various species of gases.

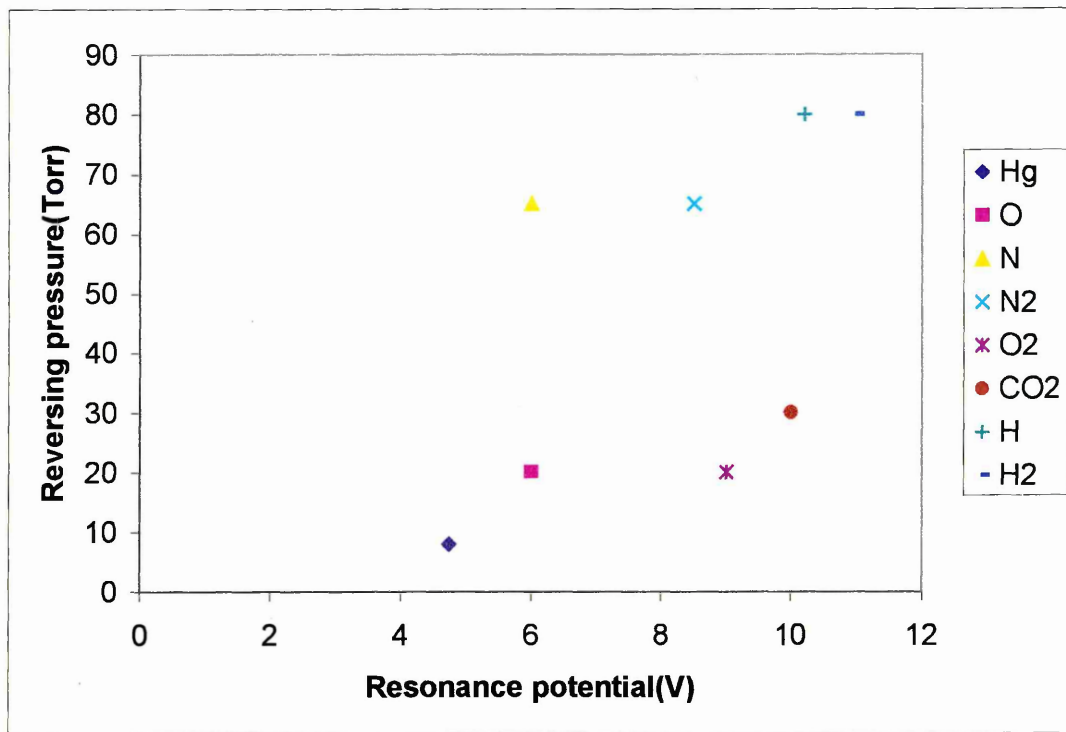


Fig 2.3, Plot of reversing pressure vs. resonance potential for various backing gases, after [31]

- *MAGNETIC FIELD AND ARC CURRENT*

Galagher performed experiments to determine the velocity of the arc at various currents and magnetic fields, producing two plots. Figure 2.4(a) shows the velocity as a function of magnetic field; over the central portion the relationship is linear. Fig 2.4(b) shows the velocity as a function of the arc current, this plot shows a plateau ; above a certain current any increase leads to only a slight increase in velocity of the arc.

During the 1970's Sherman et al[33] studied the effect of magnetic flux density on the velocity of the arc. They noted that below 15m/s there was a linear relationship between the flux density and the arc velocity, but above this level a plateauing effect was observed, see Fig 2.5. Robson[34] also performed experiments investigating the dependence of velocity of the arc on the magnetic field. In his work much higher magnetic fields(up to 5T) were used. The results, Fig 2.6, clearly show that for their system the transition from retrograde to amperian was at a magnetic field of about 1 Tesla; above this threshold the velocity varies linearly with respect to the magnetic

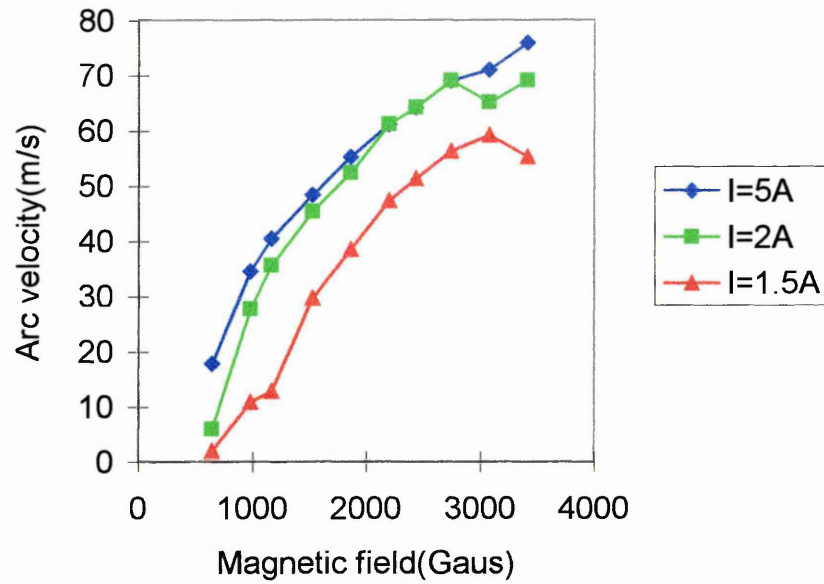


Fig 2.4(a), Plot of arc velocity as a function of magnetic field, after [31]

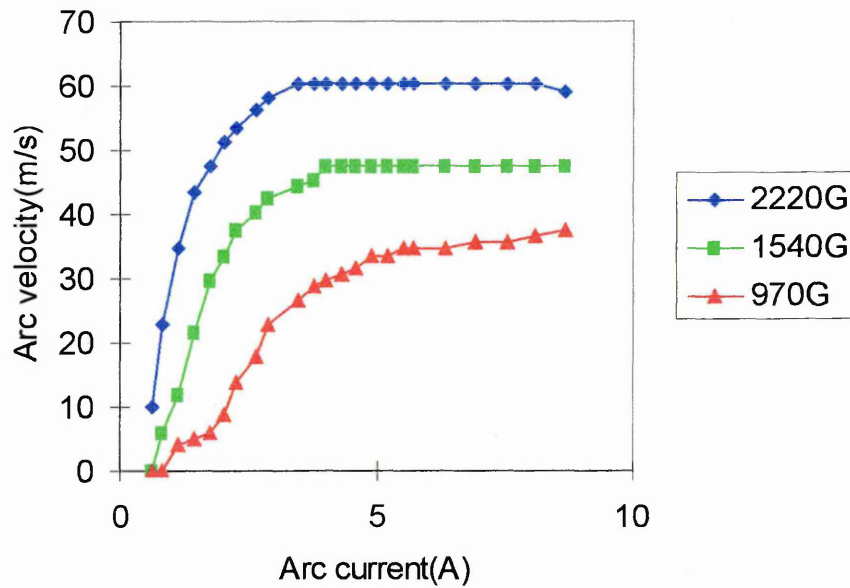


Fig 2.4(b), Plot of arc velocity as a function of arc current, after [31]

field. Swift et al [30] also investigated the relationship between magnetic field and arc motion. They observed that the arc followed the path at which the normal component of the magnetic field, B_N , was equal to zero. It was also noted that as the magnitude of the magnetic field was increased then the confinement of the arc, to the $B_N=0$ path, was greater. The work by Swift et al is discussed in greater detail in 4.1.

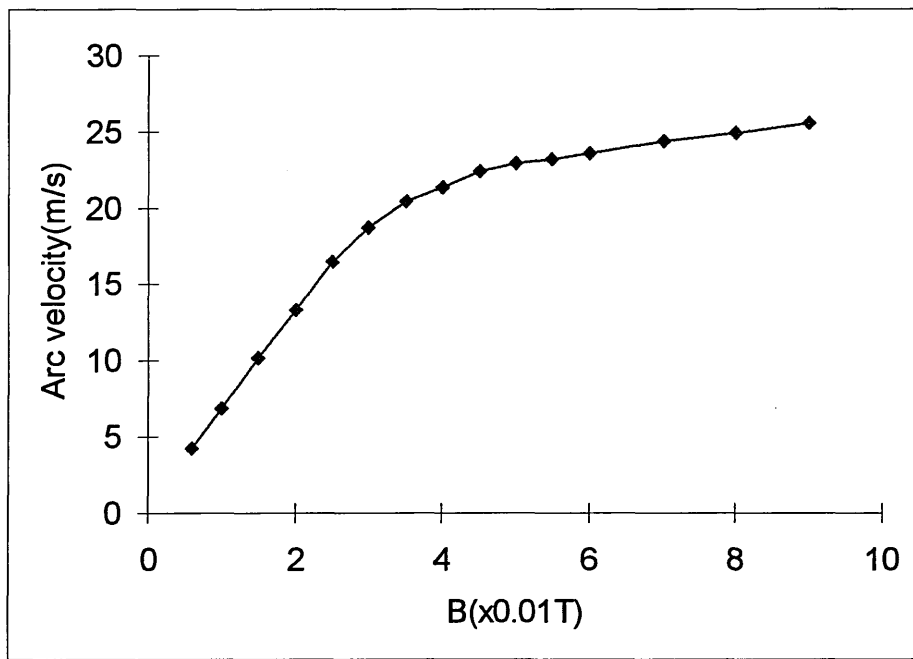
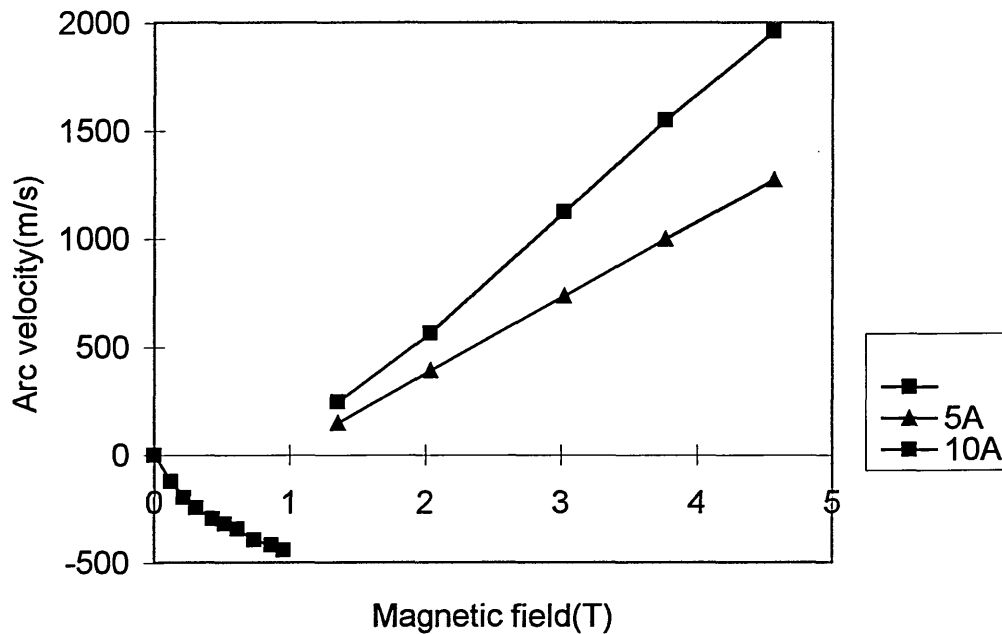


Fig 2.5, Plot of arc velocity vs. magnetic flux density, after [33]

Fig 2.6, Plot of Arc velocity vs. magnetic field, after[34]



Moving on from the work of Gallagher, Sherman(as mentioned earlier) suggested that the effect of surface contamination warranted further examination. It was observed that if the cathode had not been "arc cleaned", by allowing the arc to move randomly about the surface, then there was a marked increase in the velocity of the arc. They tested the effect of contamination of the cathode by measuring the velocity of the arc after the surface had been cleaned, and then again after exposure to air.

Fang[20,35] performed experiments to investigate the relationship between velocity and arcing number. From this plot, Fig 2.7, it can be seen that after a substantial number of arcs, approximately 50, the velocity of the arc stabilises. This levelling off of the arc velocity fits well with the idea of two different Types of cathode spot which has been noted by others such as Froome 1949/50, Hoyaux 1972 and Rahkovskii 1972.

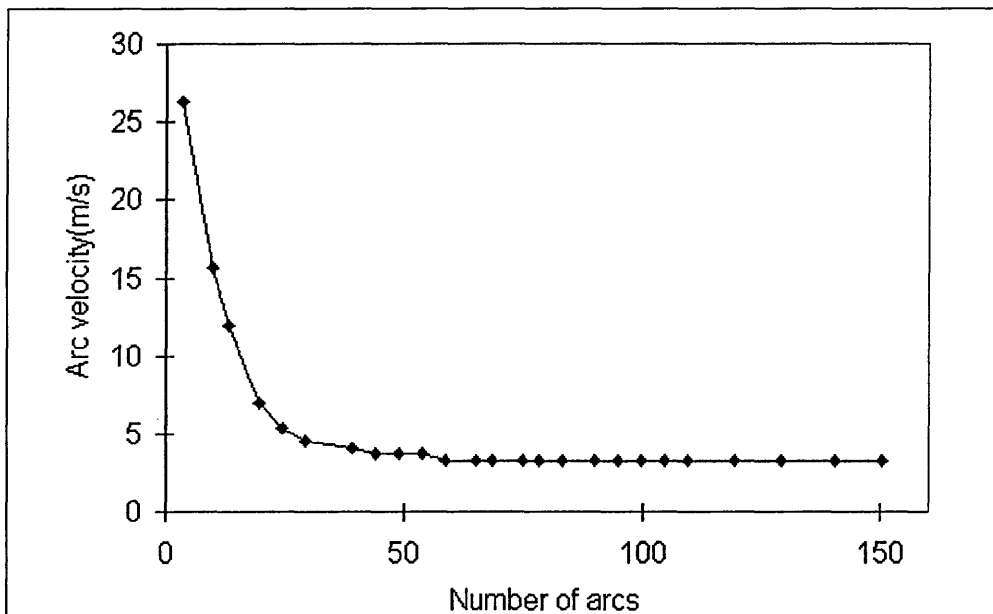


Fig 2.7, Plot of arc velocity as a function of number of arcs, after [20,35]

During the work performed above by Fang it was also noted that the velocity of the arc also showed itself to be linked to the temperature of the cathode and the electrode spacing, Fig 2.8 and 2.9.

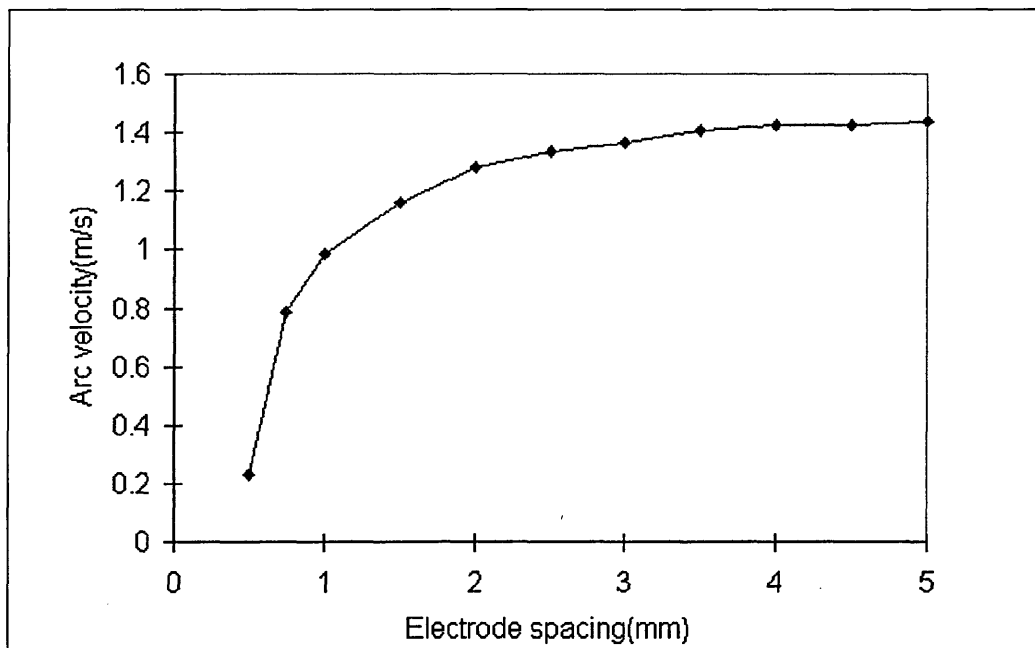


Fig 2.8, Plot of Arc velocity vs. electrode spacing, after[20,35]

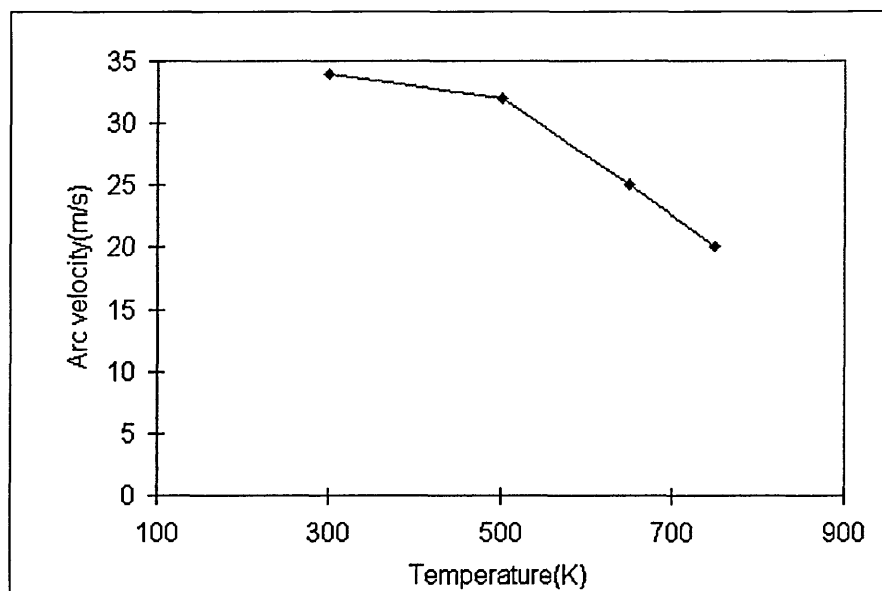


Fig 2.9, Plot of arc velocity vs. cathode temperature, after [20,35]

The final parameter linked to the arc velocity is surface roughness and general condition of the cathode. Jüttner et al[19] investigated the effect of the surface imperfections on the arc motion. They observed that the arcs tended to follow scratches or imperfections on the surface of the cathode; this was attributed to preferential accumulation of debris and contamination at these sites. Tying in with earlier work Fu[36] investigated the effects of surface roughness on the characteristics of arcs. It was discovered that a rougher surface has several effects:

- Longer arc lifetimes
- Lower arc voltages
- More diffuse motion of the spot.
- Higher retrograde velocity under the influence of a magnetic field
- Higher maximum erosion per Coulomb from the surface. This was related to the conical protrusion model of Daalder[37]

She also proposed an amendment to the definition of a Type 1 cathode spot, produced by Rahkovskii et al[3]. Fu believed that the effect of surface roughness should be incorporated into the definition.

2.2 MODELS OF ARC MOTION

2.2.1 MOTION OF THE CATHODE SPOT CONSIDERED AS A RANDOM WALK

The following is a description of the models of arc motion mentioned in 2.1.5, and is based on the work of Daalder[39]. Daalder assumed that the cathode spot moves from the origin of an x-y co-ordinate system. During each time step, τ , the spot can move a step of +s or -s in the x or y directions, with these movements being assumed to be of equal probability. We now consider a string of n such movements taking a total time t (i.e. $t=n\tau$). Assuming that this chain consists of a large number of events and that the displacements along the axes are independent, then the probability density function for the position of the cathode spot, $P(x,y)$, can be written

$$P(x,y) = \frac{1}{2\pi\alpha t} \exp\left(-\frac{x^2 + y^2}{2\alpha t}\right) \quad \text{EQ 2.3}$$

where α is the diffusion constant

This expression can be translated into cylindrical co-ordinates giving the probability, $P(R)$, of the spots being between R and δR from the origin

$$P(R) = \frac{R}{\alpha t} \exp\left(-\frac{R^2}{2\alpha t}\right)$$

A value of mean spot displacement, \bar{R} , follows from this distribution. Following from 2.1.5, since we are now considering motion in the x and y directions then the elementary step, s(1 dimension), now becomes s' (2 dimensions), where $s' = s\sqrt{2}$

$$\text{and} \quad \bar{R} = \left(\frac{\pi s'^2 t}{2\tau}\right)^{0.5}$$

Daalder then set about confirming that the motion of the spot can be described by a Rayleigh distribution. This was achieved by examining the x and y movements of the spot separately. It was found that the distributions were normal and centred about the zero displacement, with the probability, p, of a +s or -s step in either direction being 0.5

in both directions. Thus Daalder concluded that the motion of the cathode spot is a 2D random walk.

Independent work by Anders and Jüttner[13] also found evidence of the spot motion being a random walk phenomenon.

2.2.2 MOTION OF THE CATHODE SPOT UNDER THE INFLUENCE OF A MAGNETIC FIELD

Over the past several decades numerous authors[30,41,42,43] have studied the effect of externally applied magnetic fields upon the motion of the arc. The following covers the different types of models which try to explain this motion. The most important test of any of these models is their ability to explain the retrograde motion of the arc. There are several different categories into which these models may be placed. The first four categories attempt to explain the reason why the arc moves as it does, but the final type of model aims to accurately describe the motion in relation to given characteristics. The categories are:

- a. Asymmetric confinement of the plasma associated with the cathode spot
- b. Movement of the positive space charge above the cathode spot
- c. Movement of the plasma associated with the cathode spot
- d. Influence of the field upon the plasma column
- e. Stochastic model of the cathode spot

The last of these options is covered in more detail here, as the predictions from the model by Care[44] are tested against experimental results obtained by the author(see chapter 5).

(a) Asymmetric confinement of the spot plasma

Drouet[32,45] explained the occurrence of retrograde motion as the "uneven" or asymmetric confinement of the plasma associated with the cathode spot. This confinement arises from a combination of the applied transverse magnetic field and the "self field", which is generated by the electron current from the spot, and is illustrated by the magnetic field contour plot in Fig 2.10.

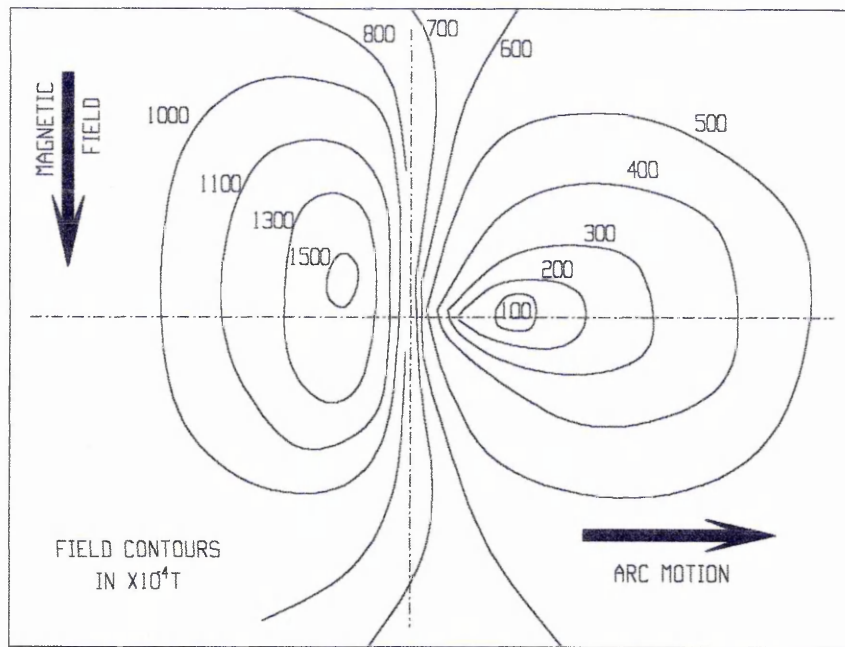


Fig 2.10, A magnetic field contour plot of the cathode spot region, after[17,32,45]

The magnitude of the self field is considerable in this model as Drouet considers the spot to be constructed from a number of smaller micro spots. These micro spots will therefore have a higher current density and hence self fields than a single spot. In fact the idea of micro spots boosts the values by approximately two orders of magnitude. The combination of the applied and self fields is constructive on the retrograde side of the cathode spot, leading to tighter confinement of the plasma, but destructive on the prograde side. This extra confinement(Fig 2.11) means that the plasma is denser on the retrograde side of the spot, leading to greater ion bombardment and heating at this point. The effect of this elevation in temperature is that it produces more favourable conditions for electron emission and hence the ignition of a new spot.

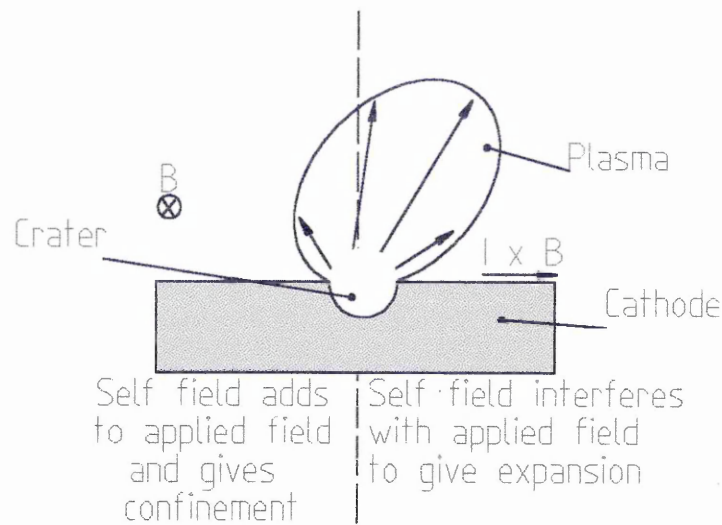


Fig 2.11, Effect of asymmetric confinement on the plasma, after [32,45]

Furthermore Drouet calculated that for external magnetic fields in excess of 1 Tesla the self field would be negligible, meaning the arc would again move in the amperian direction.

Two consequences arise from this theory:

- It indicates a subspot structure.
- The maximum distance which the arc spot can jump corresponds to the radius of the plasma cloud.

(b) Movement of the space charge above the spot

Harris[46]also considers the cathode spot to be constructed of several elements, plasma disks, hovering above the surface of the cathode. These disks remain in formation due to the opposition of the magnetic and electrostatic forces between them. The disks are considered to be comprised of a negative space charge close to the surface of the cathode, and a positive space charge lying further away, Fig 2.12.

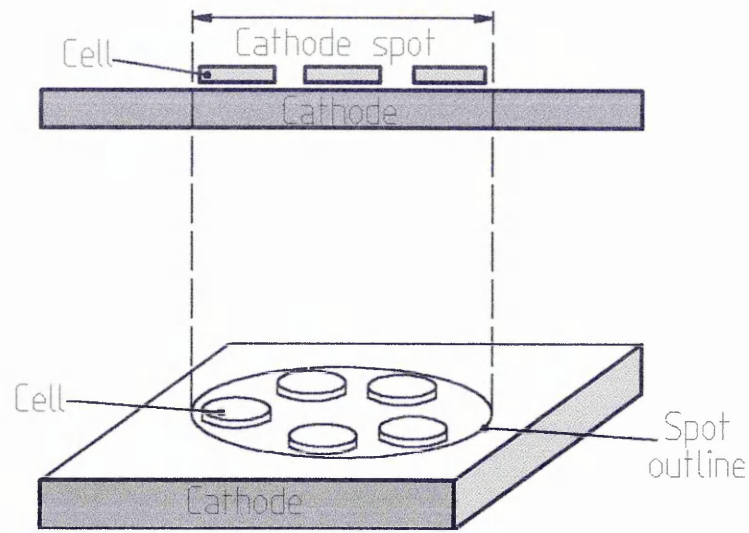


Fig 2.12, Sketch of the cathodes spot according to Harris, after [46]

If a magnetic field is now applied this will lead to the Lorentz force moving the electron cloud in relation to the positive space charge cloud, without moving the emission site. The shift in the negative space charge to the retrograde side of the spot means that the positive space charge is exposed producing an increase in electron emission. The effect of such an increase in emission is that there will be a displacement of the mean locus of emission in the retrograde direction covering the recently exposed positive space charge. Harris used the model to calculate various spot parameters, which agreed well with experimentally obtained values.

It is also noted that much earlier Longini[47] had proposed that retrograde motion of the arc was dependent upon a net space charge shift, though this model did not account for amperian motion above a certain temperature[48,49,50].

(c) Movement of the plasma associated with the cathode spot

In the model proposed by Nevskii[51] a reverse force acts upon the vaporised cathode material causing the spot to move. In the absence of a magnetic field the metallic ions are produced and swept away by the vapour stream. However when a magnetic field is applied the ions move under the influence of the Lorentz force along a circular trajectory until a collision occurs. If the collision occurs within the first half revolution then the ion will transfer its energy to the cathode spot plasma in the non-amperian direction. The

stream of ions being carried away from the cathode gives rise to a reverse force in the retrograde direction, Fig 2.13.

An expression for the velocity of the spot is then derived and is dependent upon the magnetic field and the pressure of the surrounding gas. These values of velocity are compared with work of Kesaev and show good agreement.

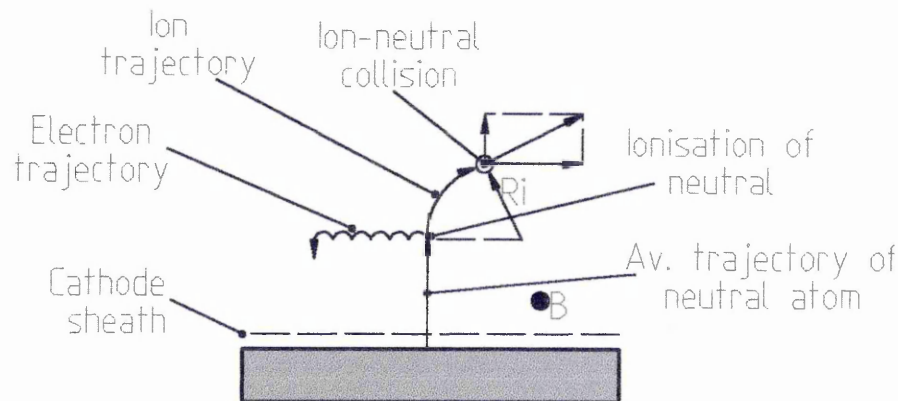


Fig 2.13, Production of reverse force, after[51]

(d) Influence of the magnetic field on the plasma column

At present there are three models which propose the effect of the field on the plasma column as the reason for retrograde motion. They all treat the column as flexible but fixed at the cathode spot end, Fig 2.14.

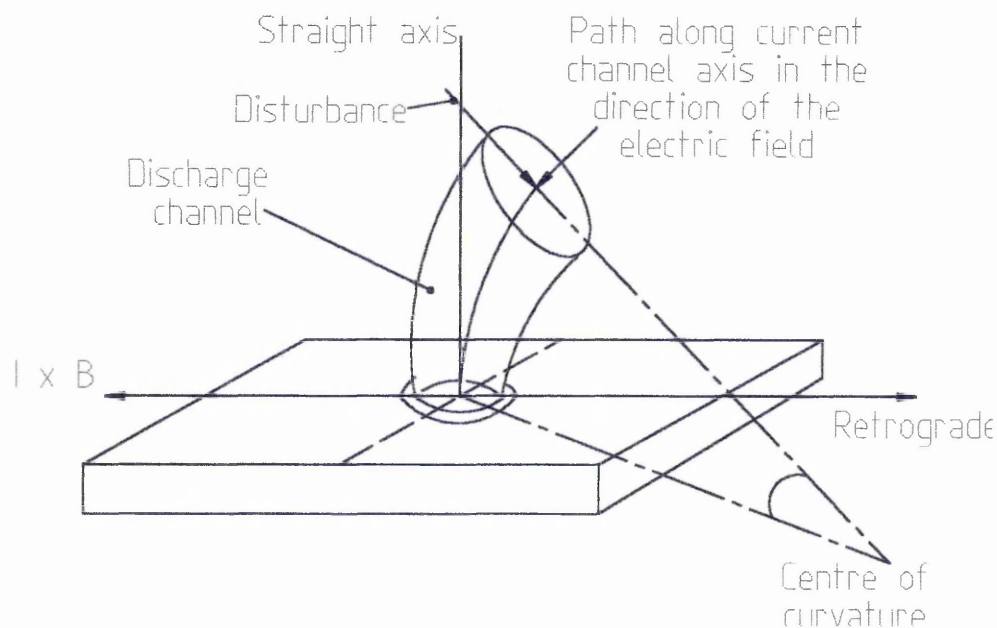


Fig 2.14, Diagram of the plasma column, after[34]

The first model to use this approach was constructed by Robson and von Engel[34]. They believed that the motion was due to unequal deflection of the arc column. It is pointed out that the column above the spot has a high electric field, with respect to the electric field of the cathode spot. Here the column is assumed to be deflected in the Lorentzian direction, and strongly curved near the cathode. Thus a force acts upon the cathode spot which is related to the sum of the applied field and the self field generated by the curved column, see Fig 2.15

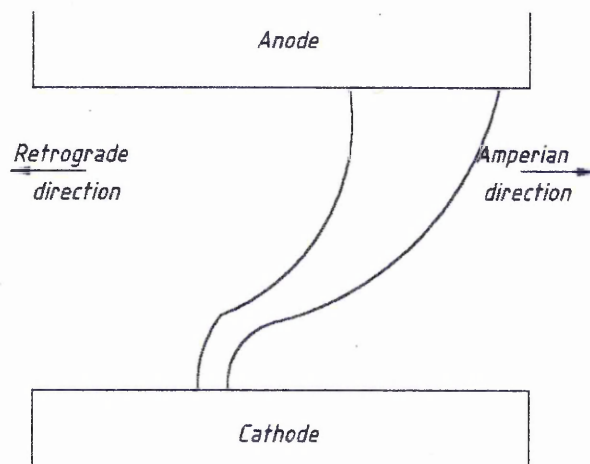


Fig 2.15 Arc in presence of transverse field, after [34]

i.e. If the self field is greater than the applied field then the spot will move in the retrograde direction.

At the time of the construction of this model there were some doubts as to its validity, the main problem being that the fields required would mean that the spot would have to be substantially smaller than was currently thought. More recent work regarding spot micro structure(2.1.4) would lead to greater current densities and hence higher self fields.

The second of these models is by Hong and Allen[52] and is based upon the earlier model of Robson and von Engel. They use electrodynamic theory to describe the arc column and believe that the force acting upon this column is a combination of forces acting in the retrograde and amperian directions. The plasma column will bend in the Lorentzian direction due to the applied magnetic field, leading to the production of a force on the column in the Lorentzian direction. This force will distort the uniform current density across the cathode spot, changing its current density profile. The change in the profile leads to the production of a force acting on the cathode spot in the

retrograde direction. Hence as the applied magnetic field increases then so does the retrograde force acting upon the spot. At some threshold point an equilibrium between the self field and applied field is reached, above which any increase in the applied field will lead to a force in the amperian direction.

The model also explains a number of features exhibited by the arc, such as:

- Temperature dependence of the velocity of the arc
- Pressure dependence of the velocity of the arc
- The effect of the cathode material upon the velocity of the arc
- The effect of surface condition on the velocity of the arc

The authors also note that retrograde motion of the arc is predicted for current densities in the order of 10^{12}Am^{-2} , this being in the range of current densities which have been experimentally observed.

Finally there is the model by Schrade[53]. In this model a force acts upon the current carrying channel(arc column), and is dependent upon the self and applied magnetic fields present in the system. This leads the author to the following conclusions.

For a straight column the forces are balanced. However if there is a disturbance to this system then the column will be bent, giving rise to the resultant force becoming non zero. If the force is acting in the opposite direction to the disturbance then the column will straighten and become stable again. Alternatively the force may be in the direction of the disturbance, this will cause the column to bend further. As the channel is bent closer towards the surface then heating of the cathode will occur, thus creating a preferential ignition site and a new spot, see Fig 2.16.

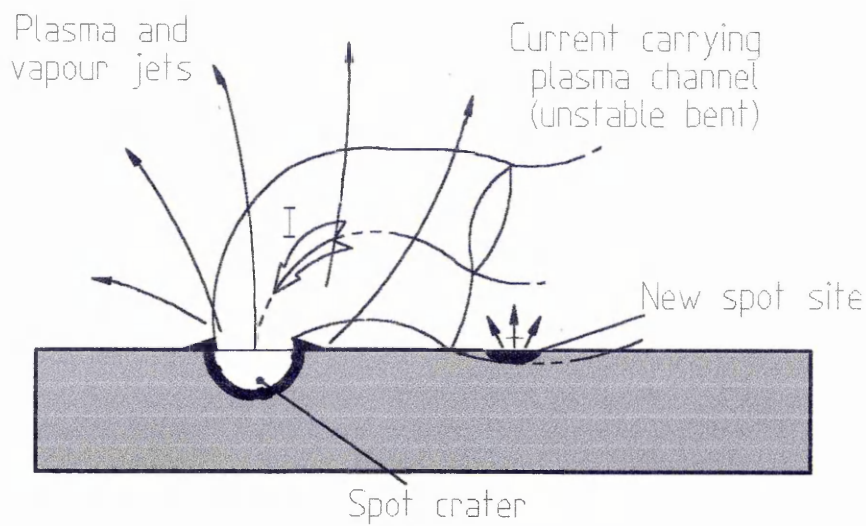


Fig 2.16, A sketch of the effect of the bending of the plasma column, after[53]

(e) Stochastic model of arc motion

This is the final model describing the motion of the arc in this chapter. The model by Care[44] is of particular interest to us, as in chapter 5 the experimental results are compared to values predicted by the theory. Care considers the arc to be moving on a two dimensional grid, Fig 2.17, on the surface of the cathode. The “forces” which influence the spot arise from the application of the transverse and normal components of a magnetic field. It has been observed that the arc moves with a velocity proportional to B_T and is confined to move along a path described by the $B_N=0$ position.



Fig 2.17, 2-D grid as envisaged by Care[44]

The position of the arc $\{i, j\}$ is moved along the axis in time steps, s , and can move in any direction or stay in the same position. The probability of the arc moving in a direction is denoted as $P^{(\eta)}$, where η is the direction of motion. The arc is steered along the x axis(2 and 4 directions) and the y axis(1 and 3 directions) is motion perpendicular to the path where the normal field is zero. Hence if the cathode spot is to progress then $P^{(2)} \neq P^{(4)}$ and there will be confinement of the spot if $(P^{(1)}-P^{(3)})$ is, say, linearly dependent upon i . The higher the value of i , the more the restoring element works to

bring the spot back to the path at which $B_N=0$ (and $x=0$). The forces described above are explained in more detail in chapter 4, section 4.1.1.

Using these forces and assumptions Care then derives a Fokker-Plank expression. This equation(EQ 2.4) describes the probability density, ϕ , of the arc's position with respect to time.

$$\frac{\partial \phi}{\partial t} = \left[D_y \frac{\partial^2 \phi}{\partial y^2} + D_x \frac{\partial^2 \phi}{\partial x^2} \right] + \left[c \frac{\partial \phi}{\partial y} \right] + \left[f(x) \frac{\partial \phi}{\partial x} + \frac{df}{dx} \phi \right] \quad \text{EQ 2.4}$$

Term (a) Term (b) Term (c)

$$\begin{aligned} D_y &= a(P^{(2)} + P^{(4)}) & D_x &= a(P^{(1)} + P^{(3)}) \\ c &= b(P^{(4)} - P^{(2)}) & f(x) &= b(P^{(3)} - P^{(1)}) \end{aligned} \quad \text{EQ 2.5}$$

Examining EQ 2.4 and 2.5 it is possible to interpret the expression physically as follows.

- If no magnetic field is applied $P^{(1)}=P^{(3)}$, $P^{(2)}=P^{(4)}$
i.e. $c=0$ and $f(x)=0$

Hence only term (a) will remain, meaning that the arc will diffuse across the surface of the cathode at a rate governed by D_x and D_y .

- If a transverse field(B_T) is now applied then c , and term (b)in EQ 2.4, will become non zero. This will have the effect of driving the arc along the x-axis, moving with a mean velocity c and the random diffusive motion superimposed on the driving motion.
- If a normal field(B_N) is now applied $f(x)$, and term (c) in EQ 2.4, will become non zero. This action is interpreted by Care as inducing a velocity to restore the arc to the path where $B_N=0$, i.e. the spot is confined by the normal field component.

REFERENCES

- [1] G A Lyubimov, V I Rahkovskii
Soviet Physics Technical Physics, 21(8) (1978) 693
- [2] A I Bushik, B Jüttner, H Pursch
Beitrage Aus Der Plasmaphysik, 19(1979)177
- [3] V I Rahkovskii
IEEE Transactions on Plasma Science, 4(2) (1976) 81
- [4] B Jüttner
IEEE Transactions on Plasma Science, 15(5) (1987) 474
- [5] A E Guille, B Jüttner
IEEE Transactions on Plasma Science, 8(3) (1980) 259
- [6] A Hull
Physical Review, 126(5) (1962) 1603
- [7] V V Kanzel, V I Rahkovskii
Proceedings of 6th International Symposium on Discharges and Electrical
Insulation in Vacuum, Swansea, (1974) 265
- [8] F R Schwirzke
IEEE Transactions on Plasma Science, 19(5) (1991) 690
- [9] L A Sena, L I Pranevychius, G.N Fursey
Proceedings of 10th International Conference on the Phenomenon on
Ionised Gases, Oxford, (1971) 105
- [10] B Jüttner
Beitrage Aus Der Plasmaphysik, 22 (1982) 453

- [11] G Ecker
Vacuum Arcs, Theory and Application, J M Lafferty(editor)
Wiley Interscience (1980)
- [12] J Kutzner, H C Miller
IEEE Transactions on Plasma Science, 17(5) (1989) 688
- [13] A A Plyutto, V N Rhyzkov
Soviet physics JETP, 20 (1965) 328
- [14] O Lloyd
Proceedings of 10th International Conference on the Phenomenon on
Ionised Gases, Oxford, (1971) 184
- [15] V L Sizonenko, M I Markov, L I Kiselevski, G G Shergin
Soviet Journal of Plasma Physics, 11 (1985) 1259
- [16] D M Sanders
Journal of Vacuum Science & Technology A, 7(3) (1989) 2339
- [17] P J Walke
PhD Thesis, Sheffield Hallam University, September 1994
- [18] Y H Fu, R P Smeets
IEEE Transactions on Plasma Science, 17(5) (1989) 727
- [19] B Jüttner, H Pursch, V A Shilov
Journal of Physics D: Applied Physics, 17 (1984) L31
- [20] D Y Fang
Journal of Physics D: Applied Physics, 15 (1982) 833
- [21] E Hantzsche, B Jüttner
IEEE Transactions on Plasma Science, 13(5) (1985) 230

- [22] J E Daalder
IEEE Transactions on Power Application Systems(PAS), 93(1974) 1747
- [23] B Jüttner
Beitrage Aus Der Plasmaphysik, 19 (1979) 25
- [24] G P Smith, R Dollinger, D P Malone, A S Gilmour
Journal of Applied Physics, 51(7) (1980) 3657
- [25] B Jüttner
Journal of Physics D: Applied Physics, 17 (1984) L11
- [26] B E Djakov, R Holmes
Proceedings of 1st International Conference on Gas Discharges, London,
(1970)468
- [27] B E Djakov, R Holmes
Journal of Physics D: Applied Physics, 4 (1971) 504
- [28] E Hantzsche, B Jüttner, H Pursch
Journal of Physics D: Applied Physics, 16 (1983) L173
- [29] J E Daalder
Journal of Physics D: Applied Physics, 16 (1983) L177
- [30] P D Swift, D R McKenzie, I S Falconer, P J Martin
Journal of Applied Physics, 66(2) (1989) 505
- [31] C J Gallagher
Journal of Applied Physics, 21 (1950) 768
- [32] M Drouet
IEEE Transactions on Plasma Science, 13(5) (1985) 235

- [33] J C Sherman, R Webster, J E Jenkins, R Holmes
Journal of Physics D: Applied Physics, 8 (1975) 696

- [34] A E Robson, A von Engel
Physical Review, 93 (1954) 1121

- [35] D Y Fang
Journal of Nuclear Materials, 111/112 (1982) 517

- [36] Y H Fu
Journal of Physics D: Applied Physics, 22 (1989) 94

- [37] J E Daalder
PhD Thesis, Eindhoven University of Technology, (1978) 66

- [38] E Hantzsche
Beitrage Aus Der Plasmaphysik, 17 (1977) 65

- [39] J E Daalder
Journal of Physics D: Applied Physics, 16 (1983) 17

- [40] S Anders, B Jüttner
IEEE Transactions on Plasma Science, 5 (1991) 705

- [41] E A Litinov, G A Mesyats, A G Parfenov
Soviet Technical Physics Letters, 16(9) (1990) 723

- [42] A E Robson
Journal of Physics D: Applied Physics, 11 (1978) 1917

- [43] V I Alferov, O N Vitkovskaya, H Cherbakov
Soviet Physics Technical Physics, 22(1) (1977) 57

- [44] C M Care
Journal of Physics D: Applied Physics, 25 (1992) 1841
- [45] M G Drouet
Japanese Journal of Applied Physics, 20(60 (1981) 1027
- [46] L P Harris
Proceedings of 10th International Symposium on Discharges & Electrical
Insulation in Vacuum, (1982) 106
- [47] R L Longini
Physical review, 71 (1947) 642
- [48] C G Smith
Physical review, 73 (1948) 543
- [49] J D Cobine, C J Gallagher
Electrical Engineer, 68 (1949) 469
- [50] D Y Fang
IEEE Transactions on Plasma Science, 11(3) (1983) 110
- [51] A P Nevskii
Soviet Physics Technical Physics, 14(6) (1969) 803
- [52] J S Hong, J E Allen
Europhysics Conference Abstracts, IGC, III (1992) 2033
- [53] H O Schrade
IEEE Transactions on Plasma Science, 17(5) (1989) 635

3.0 MACROPARTICLES

Since the beginning of research into the use of cathodic arc PVD the problem of small micro-droplets being included in the finished film has proved a problem. This chapter covers the work of a number of authors who have strived to reduce or remove the occurrence of these droplets, in order to make CAPVD a much more attractive and widely used coating technique.

3.1 What Are Macroparticles ?

As has been discussed earlier, when an electric arc interacts with the cathode surface a very small highly active emission site which produces a high velocity stream of cathode material, consisting of several components,

- Metal ions
- Neutral metal vapour
- Microdroplets, often known as macroparticles

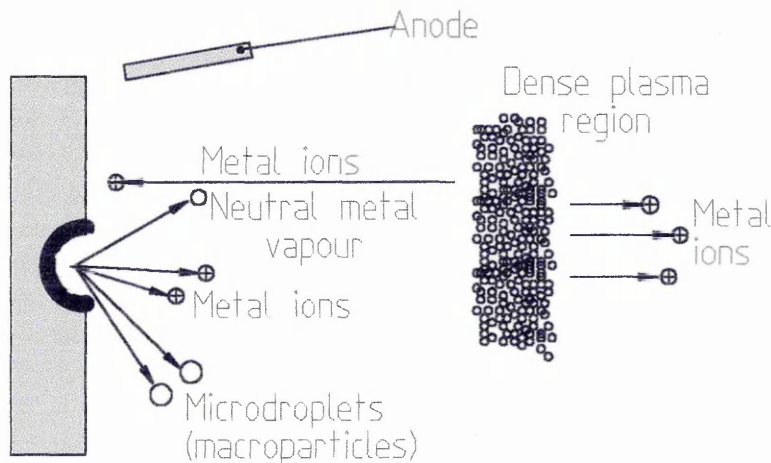


Fig 3.1, Illustration of the elements produced by an arc discharge

The macroparticles vary in diameter from sub micron to several microns. Inclusion of such particles in a metal coating could lead to premature component failure. The reason for such a failure is that during the growth of the film any macroparticles present will give rise to defects in the structure of the coating, as well as an increase in the surface roughness of the film. Since the key uses of PVD coatings are to improve hardness and corrosion resistance, anything which could be detrimental to coating life must be minimised.

3.2 Reduction/ Removal Of Macroparticles

The extent to which cathodic arc PVD(CAPVD) systems are used in industrial coating arrangements is seriously affected by the production of macroparticles. It is because of this that many authors[1, 2, 3, 4] have investigated methods by which they can be reduced or removed.

3.2.1 REDUCTION OF MACROPARTICLES

Over the course of several years a number of workers have catalogued the effect of various parameters upon the production rate of the macroparticles, and have examined methods to control their deposition. The following section is devoted to summarising this work.

- **Cathode material**

Work by Anders et al[1] showed that there was a strong dependence of macroparticle production rate on the type of material being used as the cathode. They found that materials with lower melting points produced a much higher number of macroparticles, Fig 3.2. This work supported earlier findings by Daalder[2] into cadmium and copper cathodes. Münz et al [5] also investigated macroparticle production of a variety of cathode materials with their results supporting the work of Anders and Daalder. They also noted that, when using chromium as the cathode material, a large number of smaller macroparticles were observed. This result was attributed to shrinkage of the droplets due to sublimation either as the macroparticle is in flight, or alternatively after it arrives at the substrate.

- **Arc current**

Both Tai et al[3] and Baouchi et al[4] observed that as the arc current was decreased then the number of macroparticles produced was also reduced, this is illustrated by a plot of points from work by Tai et al, Fig 3.3. Boxman[6] believed that the reduction in the arc current led to a decrease in the size of the molten pool at the cathode spot, and hence the number of macroparticles produced.

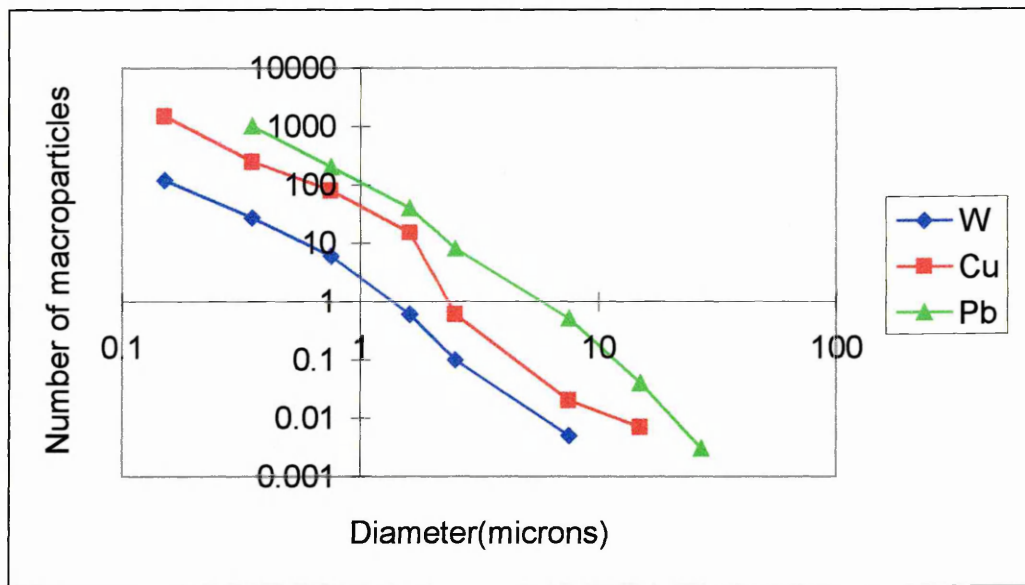
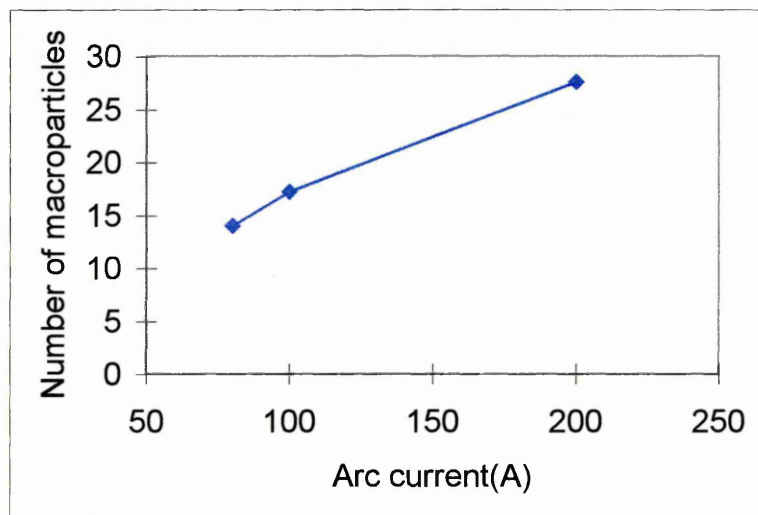


Fig 3.2, Particle size distribution, $f(d)$, for various cathode materials, after[1]

Fig 3.3, Number of macroparticles versus arc current, after[3]



- **Cathode temperature**

Shalev et al[7] noted that there was a correlation between the current pulse repetition rate and the macroparticle emission rate. Their experiments showed that, for a copper cathode, a change in pulse repetition rate from 0.3min^{-1} to 3min^{-1} gave a 40% increase in the erosion rate. The increase in erosion was also accompanied by an increase in the macroparticle production rate, which was thought to be linked to the higher average temperature of the cathode caused by the increase in the pulse repetition rate.

- **Cathode to substrate geometry**

Daalder[8] noted that the majority of the droplet mass is ejected between 20° and 30° from the plane of the cathode. Although it would seem imply that the majority of macroparticles are ejected in this angular range it is not necessarily the case. In Daalders paper the volume of each particle is calculated and then the mass, thus since particles under consideration range from 2µm to 50µm the mass of the largest macroparticle will be more than a ten thousand times more massive than that of the smallest one. Aksenov[9] noted that an appreciable number of small macroparticles travel in the direction normal to the cathode. Therefore if the surface roughness of the piece is critical the angle between the cathode and substrates should be taken into consideration. Work by Baouchi et al[4] also seems to conflict with the results of Daalder, as they find the peak emission angle to be at 60°. It would therefore seem that there is great confusion regarding the angular distribution of macroparticles, since there are a number of methods to describe the macroparticle flux, ranging from mass and volume to actual number of macroparticles. Work presented in chapter 6, uses the number and size of macroparticles counted to assess the contamination due to droplets.

Tai et al[3] noted that the distance between the cathode and the substrate is also critical when considering macroparticles, as is illustrated by Fig 3.4.

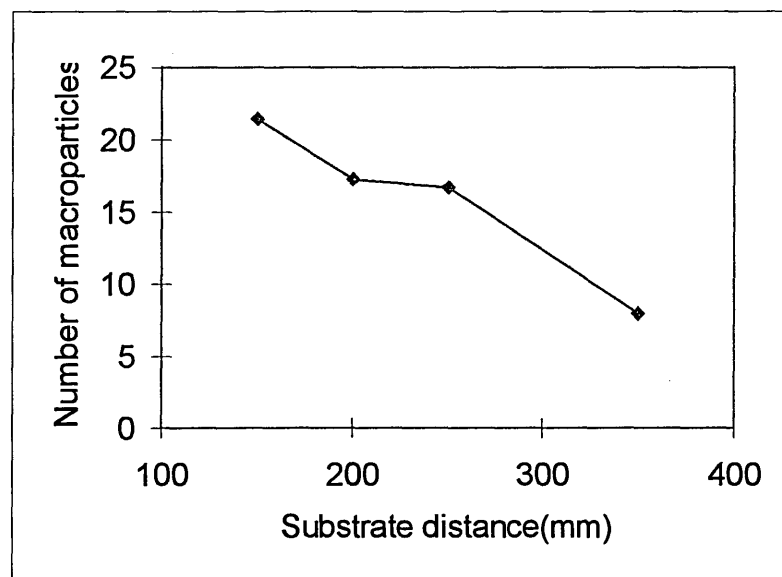


Fig 3.4, Substrate distance versus number of macroparticles

Since the droplets are ejected with a finite amount of energy, any increase in substrate to cathode distance could lead to a decrease in the number of macroparticle included in the coating. Anders et al [11] investigated the possibility that gravity was affecting the distribution of macroparticles. The results were obtained by placing samples at various positions about the coating axis and they show that gravity will only affect macroparticles above 10 μ m in diameter.

- **Species, partial pressure, of backing gas used**

Several authors[3, 4, 6, 10] have noted that the type of reactive gas, as well as its partial pressure, can lead to a change in the macroparticle production rate. This is illustrated by Fig 3.5, which shows the effect of the change in partial pressure on the number of particles detected.

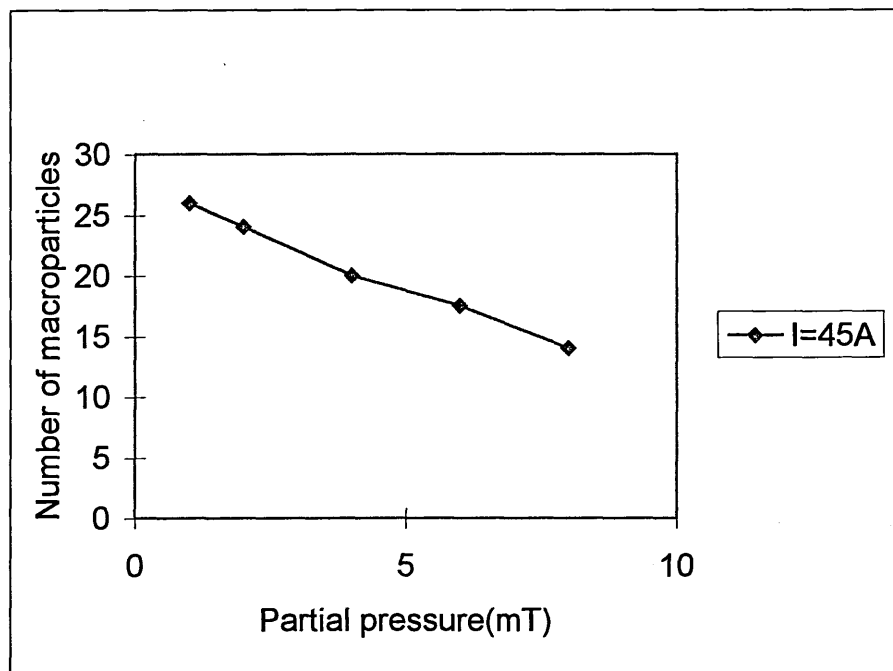


Fig 3.5, Partial pressure versus Number of macroparticles counted, after [4]

From the above the effect of the increasing partial pressure on macroparticle production can be seen. The decrease was thought to be due to the formation of a compound film on the surface of the cathode, thus the backing gas used and its partial pressure is important. Such a film will have a higher melting point than that of the bulk cathode material (for example the melting point of TiN is some 350°C higher than that of Ti), thus giving a reduction in the number of macroparticles being emitted. This effect is similar to that experienced when using different cathode materials or different arc currents.

- **Use of a magnetic field**

Numerous authors[3, 4, 10, 12] have studied the effect of magnetic field upon the motion of the arc, and consequently the production of macroparticles. The velocity at which the arc moves across the surface of the cathode and the confinement of the arc to a given path determine the droplet production rate. The effect of these parameters is discussed in more detail in chapter 6.

- **Control of the "sticking" of the macroparticles to the substrate**

Work by Tai et al[3] showed that the application of a negative bias to the substrate would reduce the number of macroparticles adhering to it. They found that if the bias voltage was changed from -20V to -300V a drop from 2.6×10^4 to 7.1×10^3 could be achieved, see Fig 3.6 for graphical illustration of results. This was supported by Vyskocil and Musil[13] who produced photographs of the surface of substrates obtained using a range of bias voltages.

Vyskocil and Musil also performed experiments to assess the impact of substrate heating on the adhesion of macroparticles. Their results are illustrated by two micrographs taken at 50°C and 500°C which showed a decrease in the number of macroparticles "sticking" to the substrate during deposition.

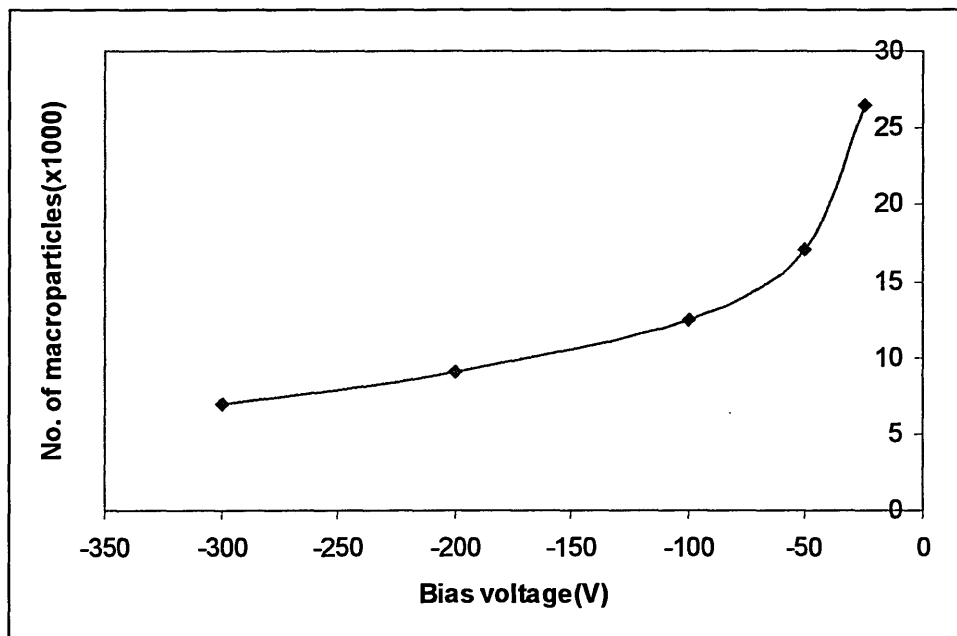


Fig 3.6, Bias voltage versus number of macroparticles collected, after[3]

- **Rotation of the cathode**

Kang et al[14] used an unusual method by which to reduce the number of macroparticles making their way to the substrates. In their experiments they used a rotating cathode arrangement, Fig 3.7, which allowed the velocity of rotation to be varied. They observed that changing the velocity from 0rpm to 4200rpm led to a reduction in macroparticles from 503×10^2 to 5×10^2 per mm^2 . The effect of varying velocity on the number of macroparticles, of different sizes, can be seen in Fig 3.8. Kang et al explained the effect as being due to centrifugal forces. As the droplets are ejected from the cathode they travel towards the wall of the chamber at a velocity dependent upon the rotational velocity of the cathode. Hence only the macroparticles are affected as the thermal velocity of the metallic ions is much greater than that of the induced tangential velocity.

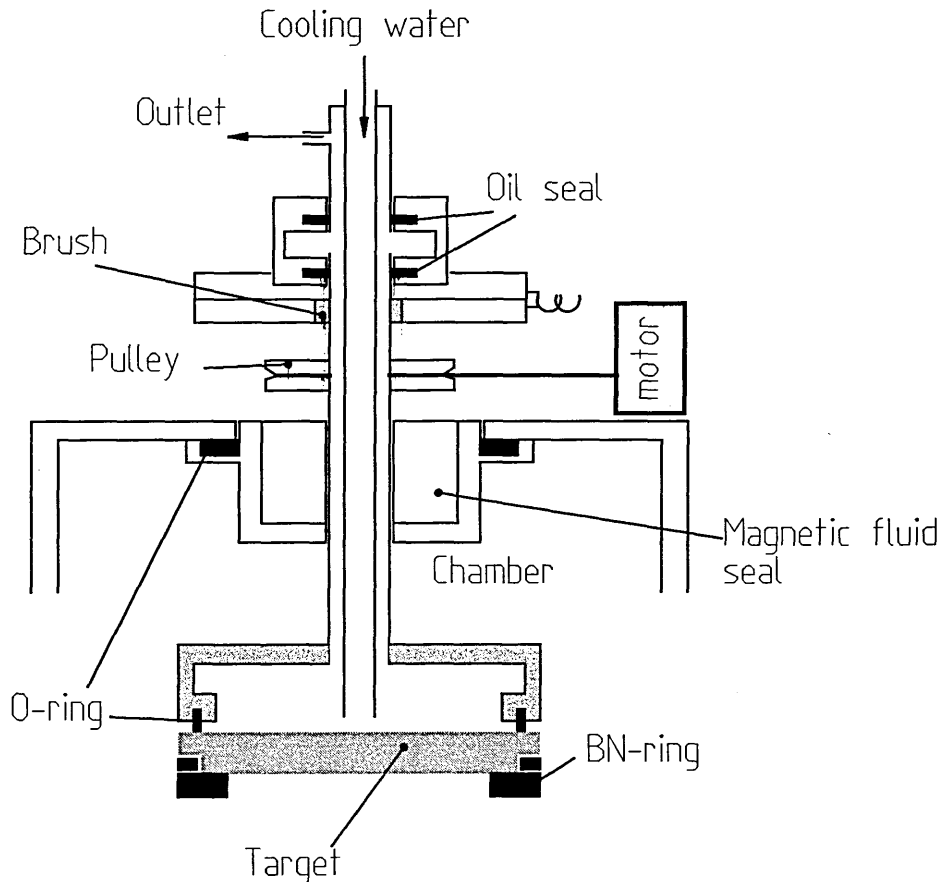


Fig 3.7, Sketch of the rotating cathode arrangement, after[14]

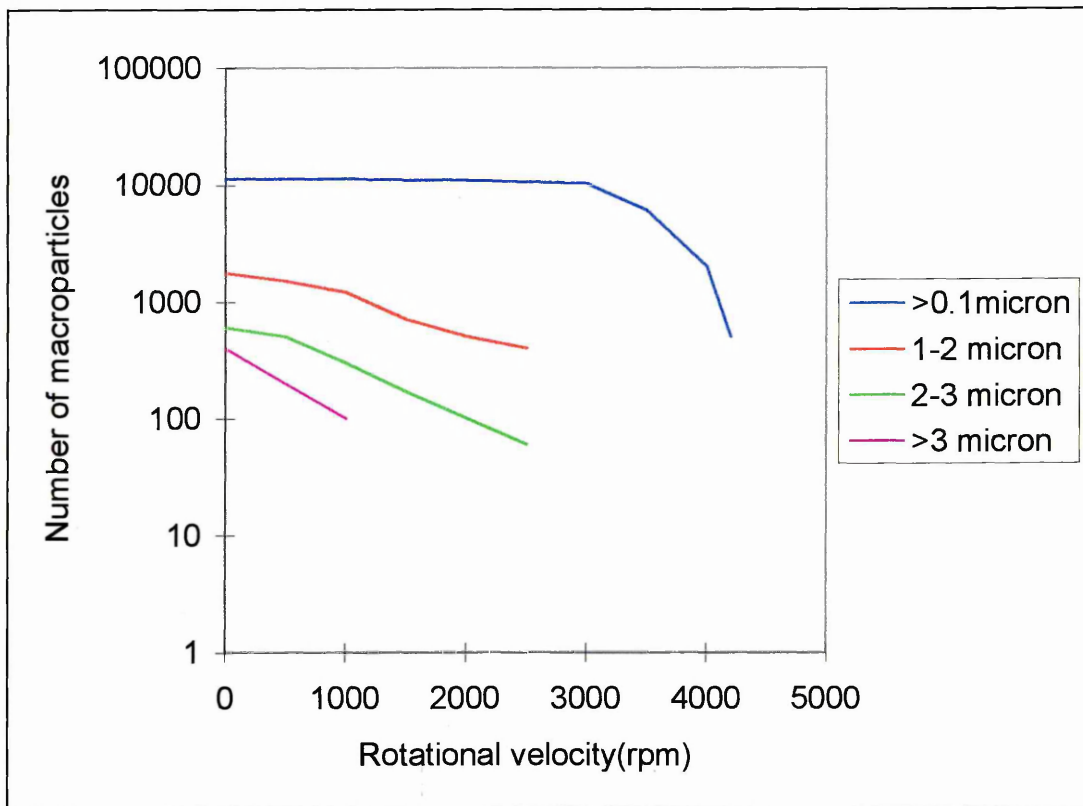


Fig 3.8, Plot of number of macroparticles versus rotational velocity, after[14]

- **Shutter system**

The simplest and cheapest way to reduce the number of macroparticles present in the coating is to introduce a shutter, or shield, directly into the plasma stream[15]. If the shield is negatively biased it will attract the positively charged ions from the plasma, but this technique also leads to a drastic reduction in the deposition rate.

- **Plasma Ducts**

This is by far the most popular method of reducing the number of macroparticles, and involves the use of a series of electromagnets to guide the plasma along a path. A number of authors[16, 17, 18, 19, 20, 21, 22, 23, 24] have studied the filtered arc, as it is more commonly known, for example Aksenov et al[16] in 1979 produced a quarter torus duct on which many other designs are based, see fig 3.9.

1000

1000

1000

1000

1000

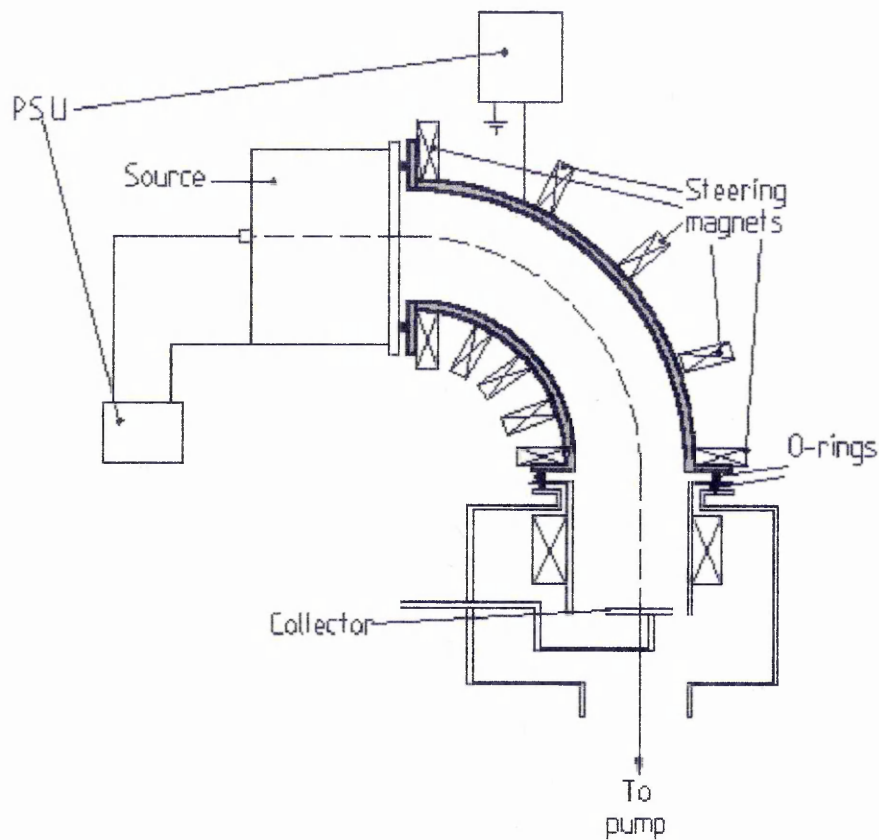


Fig 3.9, Sketch of a quarter torus plasma duct, after[16]

Initially[25] it was thought that such a duct would require large magnetic fields and hence large currents to provide the conditions for plasma transport. Later work by the same group[16] showed that what was actually required was a magnetic field large enough to guide the electrons along the duct, and the ions would then follow. What actually occurs is that the electrons will spiral along the lines of force of the magnetic field, whilst the ions, neutrals and macroparticles collide with the chamber wall. This bombardment by the ions leads to a build up of charge on the duct wall, which at some point will become large enough to repel the ions and guide them through the duct. The macroparticles, which are of a much greater mass than the ions, also attempt to follow the electrons along the duct but fail to do so. This is due to the fields in the duct being unable to exert a sufficient guiding.

Several methods have been studied to improve the efficiency of the duct, with limited success. The methods tried are:

- Optimising the duct potential[16], illustrated in Fig 3.9
- Changing the shape of the duct[17, 24, 26, 27]
- Focusing the plasma before entering the duct[28]

From the work covered in this chapter it is obvious that the problem of macroparticle contamination is critical to the extension of usage of cathodic arc PVD in commercial coating systems. Although there are many methods to reduce the number of droplets present, once the choice of thin film required has been made the number of methods is narrowed. The remaining methods included both reduction and removal mechanisms. Initially the use of a magnetic filter would seem to be the solution to the problems of macroparticle incorporation. Upon further inspection it can be seen that this method is very inefficient, as it reduces the coating rate significantly, thus in a commercial environment the complete range of options must be considered. Part of this thesis concentrates on the influence of externally applied magnetic fields on the angular distribution of macroparticles. As mentioned earlier a number of authors have studied the effect of magnetic fields, but none have been able to relate the changes in normal and transverse fields to macroparticle distribution. This work has been performed using the novel three coil electromagnetic steering array, see chapter 4, which allows a greater degree of freedom in the control of the velocity and confinement of the arc.

REFERENCES

- [1] S Anders, A Anders, K M Yu, X Y Yao, I G Brown
Proceedings of ISDEIV 1992, Darmstadt. Germany.
Published by I.E.E.E 1992
- [2] J E Daalder
Journal Of Physics D: Applied Physics 9 (1976) 2379
- [3] C N Tai, E S Koh
Surface and Coatings Technology 43/44 (1990) 324
- [4] A W Baouchi, A J Perry
Surface and Coatings Technology 49 (1991) 253
- [5] W D Munz, I J Smith, D B Lewis, S Creasey
Vacuum 48(5) (1997) 473
- [6] R L Boxman, S Goldsmith
Surface and Coatings Technology 51 (1992) 39
- [7] S Shalev, R L Boxman, S Goldsmith
Journal of Applied Physics 58(7) (1985) 2503
- [8] J E Daalder
Journal of Physics D: Applied Physics 9 (1976) 2379
- [8] K Akari, H Tamagaki, T Kumakiri, E S Koh, C N Tai
Surface and Coatings Technology 43/44 (1990) 312
- [9] I I Aksenov
Soviet Physics: Technical Physics 29(8) (1984) 893

- [10] K Akari, H Tamagaki, T Kumakiri, E S Koh, C N Tai
Surface and Coatings Technology 43/44 (1990) 312
- [11] S Anders, A Anders, K M Yu, X Y Yao, I G Brown
IEEE Transactions on Plasma Science 21(5) (1993) 440
- [12] P D Swift
Journal of Physics D: Applied Physics 29 (1996) 2025
- [13] J Vyskocil, J Musil
Journal of Vacuum Science and Technology A: 10(4) (1992) 1740
- [14] G H Kang, H Uchida, E S Koh
Surface and Coatings Technology 68 (1994) 141
- [15] H Brandoff
US Patent No. 4,511,593 (1985)
- [16] I I Aksenov, V A Belous, V G Padalka, V M Khoroshikh
Soviet Journal on Plasma Physics 4(4) (1978) 425
- [17] J S Storer, J E Galvin, I G Brown
Journal of Applied Physics 66(11) (1988) 5245
- [18] P J Martin, R P Netterfield, T J Kinder
Thin Solid Films 193/194 (1990) 77
- [19] A Anders, S Anders, I G Brown
Journal of Applied Physics 75(10) (1994) 4900
- [20] V N Zhitomirsky, R L Boxman, S Goldsmith
Surface and Coatings Technology 68/69 (1994) 146

- [21] T Witke, P Siemroth
IEEE Transactions on Plasma Science 27(4)(1999) 1039

- [22] D R McKenzie, Y Yin, E G Gerstner, M M M Bilek
IEEE transactions on Plasma Science 25(4)(1997) 652

- [23] Y Yin, D R McKenzie
Journal of Vacuum Science and Technology A: 14(6)(1996) 3059

- [24] P J Martin, A Bendavid, H Takikawa
Journal of Vacuum Science and Technology A: 17(4)(1999) 2351

- [25] I I Aksenov, V A Belous, V G Padalka, V M Khroshikh
Instrumentation and Experimental Technology 5 (1978) 236

- [26] S Anders
Proceedings ISDEIV 1996 ,Berkeley, California - Vol 2, pg 904
Published by I.E.E.E

- [27] I I Aksenov, V M Khoroshikh, N S Lomino, V D Ovacharenko
IEEE transactions on Plasma Science 27(4)(1999) 1026

- [28] S Anders, A Anders, I G Brown
Journal of Applied Physics 75(10) (1994) 4895

4.0 EXPERIMENTAL SET UP

This chapter describes the experimental arrangement used in the work for this thesis, and the changes required in order to investigate the parameters of interest. The chapter can be divided into three parts:

- *Development of electromagnetic control of the arc*

This section describes the progress of magnetic/electromagnetic steering systems used for controlling the motion of the arc.

- *Development of new hardware for the vacuum rig*

This section deals with the design of new hardware for the vacuum apparatus to enable experiments to be performed. The reasons for altering the system are discussed along with the solutions which were used.

- *Experimental apparatus used*

Here an overview of the vacuum system is presented, along with details of pumping systems, power supplies and gas control.

4.1 Development of Electromagnetic Control of the Arc

This section covers the development of electromagnetic control of the vacuum arc. This development began by using permanent magnets situated behind the cathode[1], and progressed further as electromagnets were used[2,3]. The use of electromagnets heralded a new era for arc control as now magnetic fields of various magnitudes and geometries could be generated.

4.1.1 CONTROL OF THE ARC

Following on from the work of Ramalingham[1](see chapter 1), a range of authors developed electromagnetic arc steering systems. Swift et al[2] developed a control system consisting of a single electromagnetic coil situated at the rear of the cathode, Fig 4.1. Using such an arrangement it is possible to vary the magnitude of the normal and transverse elements of the magnetic field, but not the position at which $B_N=0$, i.e. the orbital radius. In order to alter the orbital radius the coil would have to be moved away from the rear of the cathode, meaning that if the same field values were to be maintained then a large increase in coil current would be required. Hence such a system is said to have only one degree of freedom.

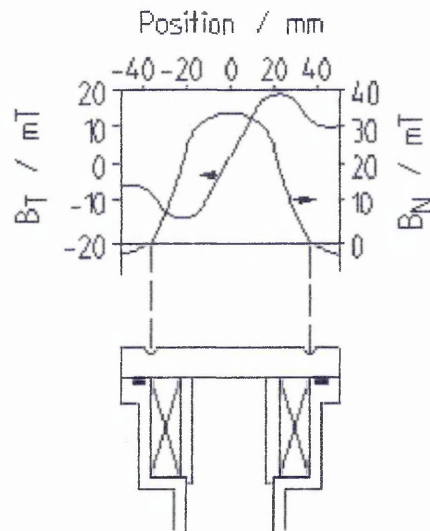


Figure 4.1, sketch of the electromagnets from Swift[2]

From their experiments Swift et al found that the arc tended to follow the path at which B_N was equal to zero. They hypothesised that the arc maintained this path due to a restoring

force, \underline{F} , which was generated by the action of the magnetic field, B , acting upon a positive space charge, $+q$, which is carrying a current density, j . The existence of this positive space charge is consistent with models produced by Plyutto[4] and Davis and Miller[5] (see chapter 2). From the experimental work performed Swift et al noted that, as in many such cases, the arc moved in the retrograde direction. An empirical description is then,

$$\underline{v} \sim -\underline{j} \wedge \underline{B} \quad (\text{EQ 4.1})$$

leading to an expression for the restoring force

$$\underline{F} \sim q[\underline{v} \wedge \underline{B}] \sim q[\underline{B} \wedge (m \underline{j} \wedge \underline{B})] \quad (\text{EQ 4.2})$$

which, using the vector identity $a \wedge (b \wedge c) = (a \cdot c)b - (b \cdot c)a$, gives

$$F \sim q[\underline{B}^2 \underline{j} - (\underline{B} \cdot \underline{j})\underline{B}] \quad (\text{EQ 4.3})$$

The first term in the above expression represents a force towards the cathode: the second term represents a restoring force; close to the path $B_N=0$ this takes the form of $B_N j B_T$. This acts along B_T if B_N is negative and opposed to B_T if B_N is positive.

Swift et al also noted that as the arc traversed around its orbit there was also some small deviation from the path at which the normal component of the magnetic field, B_N , was zero. They noted that such deviations grew smaller as the normal field strength increases.

Walke et al[3] considered this further and noted that at small deviations from the $B_N=0$ path then B_N can be approximated to the normal field gradient, B_N' , multiplied by the distance, x , of the arc from the path at which $B_N=0$, i.e.

$$B_N \sim x B_N'$$

Hence it may be expected that the magnitude of the force restoring the cathode spot to the $B_N=0$ position will increase more rapidly for larger normal field gradients.

These observations were used by Care as the basis for his model of arc motion[6].

4.1.2 THE TWO COIL STEERING ARRAY

As mentioned in the previous section the single coil steering array has limitations, it is only possible to alter the orbital radius of the arc by moving the coil away from the rear of the cathode. Following repositioning of the magnet a substantial increase in the coil current would be required to maintain the same level of magnetic field. A two coil magnetic steering system, used by Walke et al - Fig 4.2, gives better control as now the two magnetic fields generated by the electromagnets can be combined to change the overall geometry of the field.

When the fields of the two coils are superimposed it is possible, through the choice of the correct current ratio, to alter the orbital radius of the arc as well as one of either B_N' or B_T .

The reason for the development of the two coil steering array was twofold:

- To improve the efficiency of cathode usage by varying the orbital radius.
- To test the model of arc motion of Care[6].

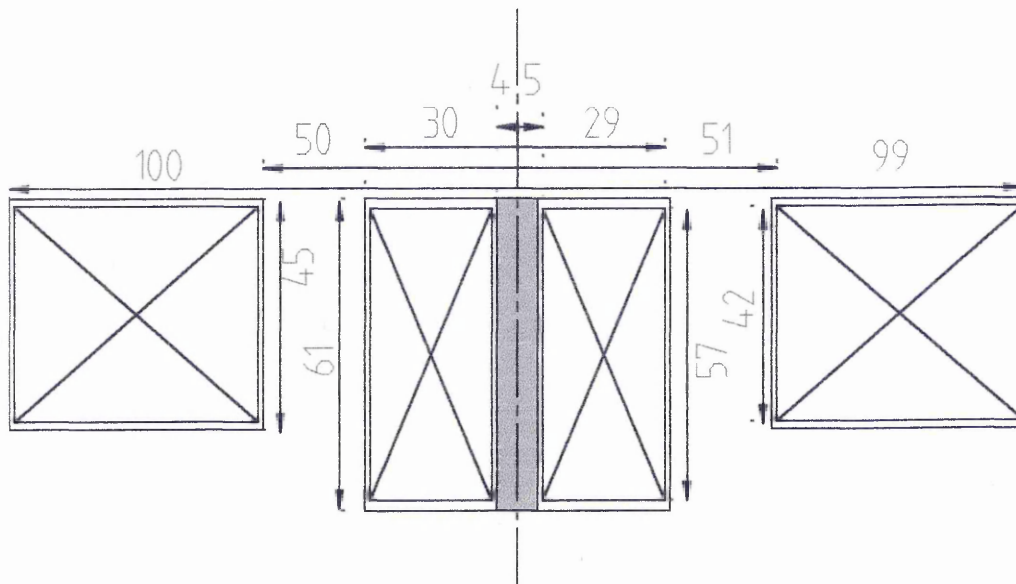


Fig 4.2, Diagram of the two coil magnetic steering array by Walke[3]

4.1.3 THE THREE COIL STEERING ARRAY

Using the steering system of Walke[3] it was impossible to fully test the model by Care[6], since he could not produce the degree of freedom required (EQ 4.6 and Appendix A). This being the case a new method of controlling the arc was required, this new system being a three coil steering array. The reason for the transition to three coils is explained in the following.

For a two coil arrangement it can be seen that

$$B_T(total) = B_T(coil1) + B_T(coil2) = K_T^{(1)} I^{(1)} + K_T^{(2)} I^{(2)} \quad (EQ 4.4)$$

$$B_N(total) = B_N(coil1) + B_N(coil2) = K_N^{(1)} I^{(1)} + K_N^{(2)} I^{(2)} \quad (EQ 4.5)$$

where

$K_N^{(x)}$ - Function of radius dependent on B_N of coil x

$K_T^{(x)}$ - Function of radius dependent on B_T of coil x

$I^{(x)}$ - Current flowing through coil x

From EQ 4.4 and 4.5 it can be shown(see Appendix A) that if a particular orbital radius is set then

$$B_N' \propto I^{(1)} \text{ and } B_T \propto I^{(1)}$$

hence

$$B_N' \propto B_T, \quad (EQ 4.6)$$

meaning that B_N' and B_T cannot be independently controlled.

However for a three coil system there are now three variables, $I^{(1)}$, $I^{(2)}$, $I^{(3)}$. Again it is possible to obtain equations for the normal and transverse elements of the magnetic field

$$B_T(total) = B_T^{(1)} + B_T^{(2)} + B_T^{(3)} = \sum_{x=1}^{x=3} K_T^{(x)} I^{(x)} \quad (EQ 4.7)$$

$$B_N(\text{total}) = B_N^{(1)} + B_N^{(2)} + B_N^{(3)} = \sum_{x=1}^{x=3} K_N^{(x)} I^{(x)} \quad (\text{EQ 4.8})$$

From these two equations it is possible (see Appendix A) to obtain two simultaneous equations for B_N and B_T .

$$B_T = \alpha_T^{(21)} I^{(2)} + \alpha_T^{(31)} I^{(3)} \quad (\text{EQ 4.9})$$

$$B_N = \alpha_N^{(21)} I^{(2)} + \alpha_N^{(31)} I^{(3)} \quad (\text{EQ 4.10})$$

where the α are functions of radius dependent upon the values of K_N and K_T for the three coils.

As can be seen from the above equations B_T and B_N are now no longer linked, meaning that with a three coil steering array it is possible to control B_N and B_T independently for a given radius,

i.e. there are three degrees of freedom. The extent of independent control of the three parameters depends on how different are the geometries of the three electromagnets.

4.2 Development of New Hardware for the Vacuum Rig

4.2.1 THE THREE COIL STEERING ARRAY

The following section is devoted to describing the design, construction and testing of the novel three coil electromagnetic steering array.

Modelling of the magnetic coils

To enable the design of a series of electromagnets to be designed a method to assess their performance was required. Walke et al[3] investigated various methods to predict the field profiles of an electromagnet and found that a Biot-Savart approach, describing the field produced by current carrying loops, proved satisfactory. This method was then converted to a computer program enabling the modelling of the three coils to be performed simultaneously.

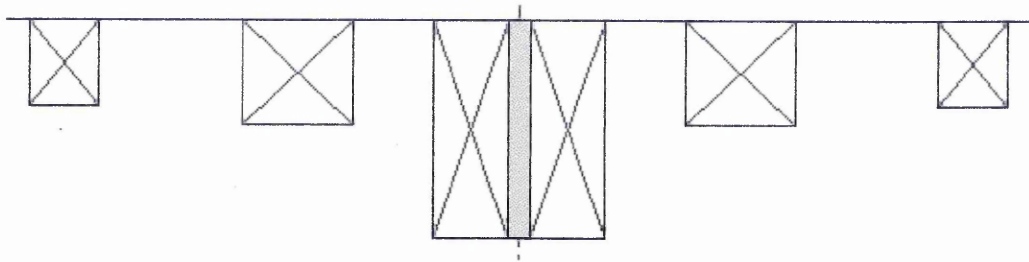
Options for coil configurations

As has been mentioned earlier, to produce the degree of freedom required we need a three coil steering system in which the coils have different field geometries. After careful consideration three such configurations were examined using the Biot-Savart program described above, see fig 4.4.

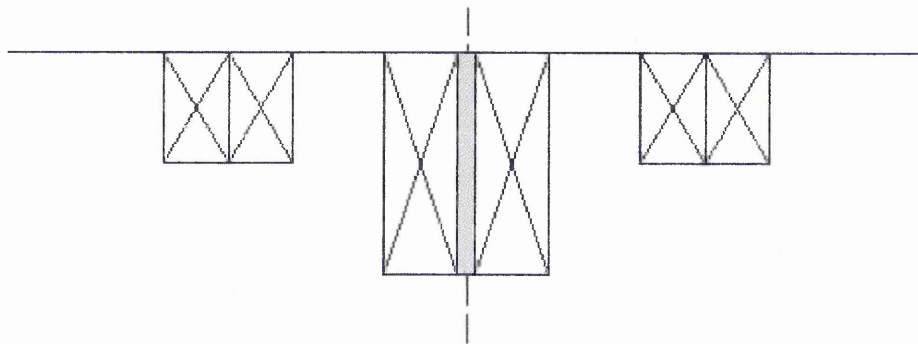
Using the program it was possible to generate both the normal and transverse field profiles from which the coil constants, as described in 4.1.3, could be derived. Once these constants had been obtained it was then possible, through substitution into equations 4.4 and 4.5, to check suitability of the coil configuration. There were three criteria which the new coil arrangement had to comply with,

1. The currents must be achievable i.e. must be able to be supplied using the 12A, 25A and 18A power supplies.
2. The fields obtained must produce a range of velocities and confinement which are detectable.
3. The new coils must be able to fit in the existing cathode assembly, or vacuum chamber.

- *Scenario A - New coil placed outside the cathode assembly*



- *Scenario B - existing outer coil is split*



- *Scenario C - New coil is placed between the two existing coils*

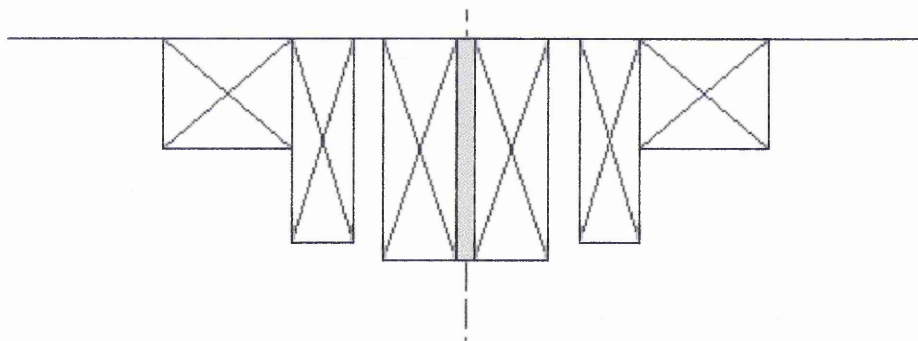


Fig 4.4, Sketches of the three possible coil configurations under consideration

Examination of the range of coil constants produced by the coils in the different scenarios resulted in the following:

- Scenario A - Due to the large radius of the proposed outer coil very large currents would be required if the coil was to enable the transverse field(B_T) and the normal field gradient(B_N') to be altered significantly. Hence this configuration was deemed unsuitable.
- Scenario B - Using this configuration it would be possible to vary the orbital radius and transverse field, but there would be insufficient scope for variation of B_N' . Thus this configuration was also deemed unsuitable.
- Scenario C - This scenario would enable us to alter all three parameters to such a degree that it was predicted that it would be possible to measure differences in both velocity and confinement of the arc. Thus it was thought that this arrangement of the electromagnets would prove most suitable.

Once the decision on coil configuration had been taken, a more in depth study of the currents required to produce certain magnetic fields was performed. This investigation involved the use of a spreadsheet. In this spreadsheet the coil constants, derived from the Biot-Savart program, were used in conjunction with the three coil equations(EQ4.9, 4.10) to produce values for the total magnetic field profiles. The study of these field profiles then allowed the identification of the orbital radius which would permit most control to be exerted on the motion of the arc.

Design of the coils

Now that the coil design had been decided, see Fig 4.4, the new steering array had to be constructed. The design to be used was based on the inner coil of the existing 2 coil steering array, complete with soft iron core[3], with the outer two coils requiring fabrication. As can be seen from Fig 4.5 it was necessary, due to spatial restrictions, to construct the new outer two coils as one single module.

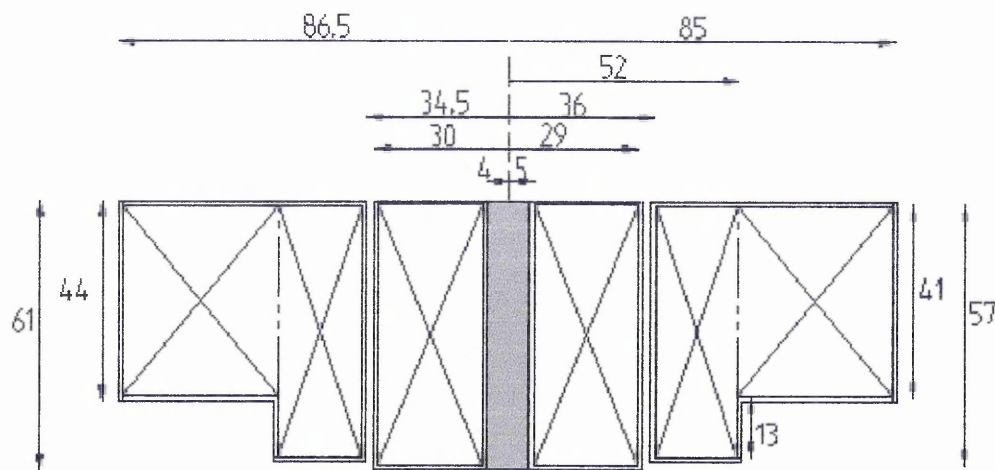


Fig 4.5, Diagram of the three coil steering array

From previous experience, with the two coil arrangement, it was known that passing such currents through the electromagnets could lead to overheating of the coils, hence a temperature monitoring and cooling system was required. The cooling system used by Walke et al, Fig 4.6, proved relatively ineffective thus several alternative methods to improve cooling were considered:

- The same method as Walke et al, but increasing the number of turns of cooling pipes. Using a smaller bore pipe would increase the surface contact area and therefore increase heat dissipation.
- If the brass jacket which encloses the windings were made water-tight then a thermally conducting fluid could be introduced, increasing heat dissipation from the coil windings to the brass jackets and thus the cooling pipes.
- Incorporation of small bore cooling pipes into the coil assemblies. This would take the form of U-shaped pieces of piping at intervals around the former to provide cooling at the heart of the coils, see Fig 4.7.

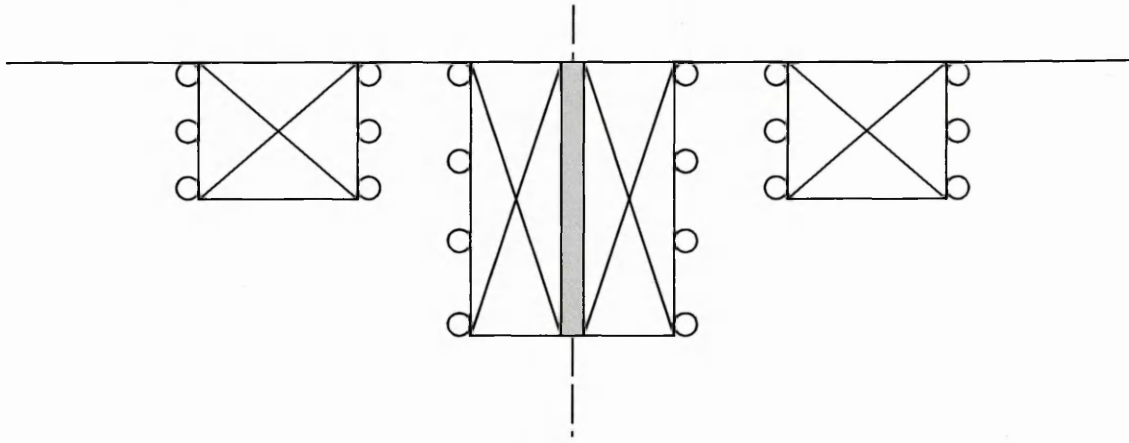
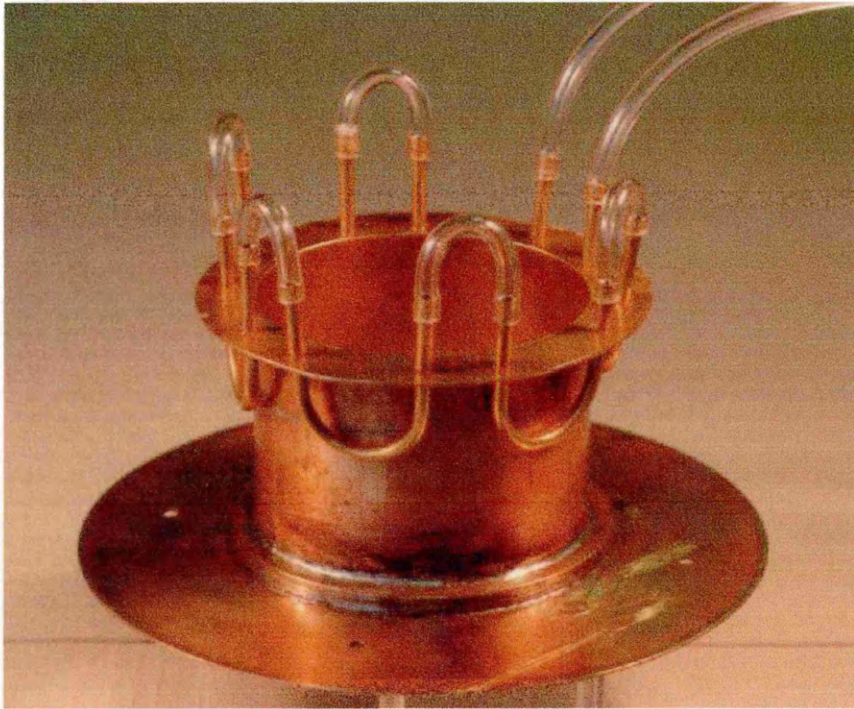


Fig 4.6, Sketch of cooling system used by Walke[3]

Fig 4.7, Photograph of proposed cooling system



After consideration of the three options it was decided that due to space and leakage considerations option c was identified as the best method. The effect of the incorporation of these cooling tubes was then modelled to make sure that the required fields were still achievable. Examination of the resultant modelled field profiles indicated that the cooling system design was an acceptable amendment.

Now that the design of the coils had been finalised, the brass formers/jackets were constructed. Once complete they were mounted on a lathe and the coils hand wound, using

1.7mm o.d. enamelled copper wire. At intervals of approximately 3-5 layers of windings the coil was bound using a heat resistant insulating tape in order to keep the windings tight, regular and undamaged. Once the construction had been completed the coils were tested for short circuits between the formers and the windings. When it was decided that the coils were functioning correctly then the cooling system was connected and the steering array fastened into the cathode assembly ready for testing of the magnets.

Testing of the magnets

In order to assess the impact of the new coils a Hall effect Gauss/Tesla meter was used to measure the field profiles of produce coil constants, as plotted below. It was known that due to the addition of the soft iron core then these results would not be exactly as predicted by the model, hence the coil constants needed to be determined experimentally. The values were then fed into the spreadsheet. Such a sheet was then used, in conjunction with the three coil equations, to allow values for B_N , B_T and B_N' to be calculated at a variety of distances from the centre of the coils given the coil currents, see figs 4.8 and 4.9. Using this work it was then possible to derive a number of coil current configurations which have an orbital radius of 2cm but also allow various combinations of B_N' and B_T to be obtained. Examples of such a settings are shown as Fig 4.10(a) and (b).

Coil constants for the new middle coil. Total number of turns= 276

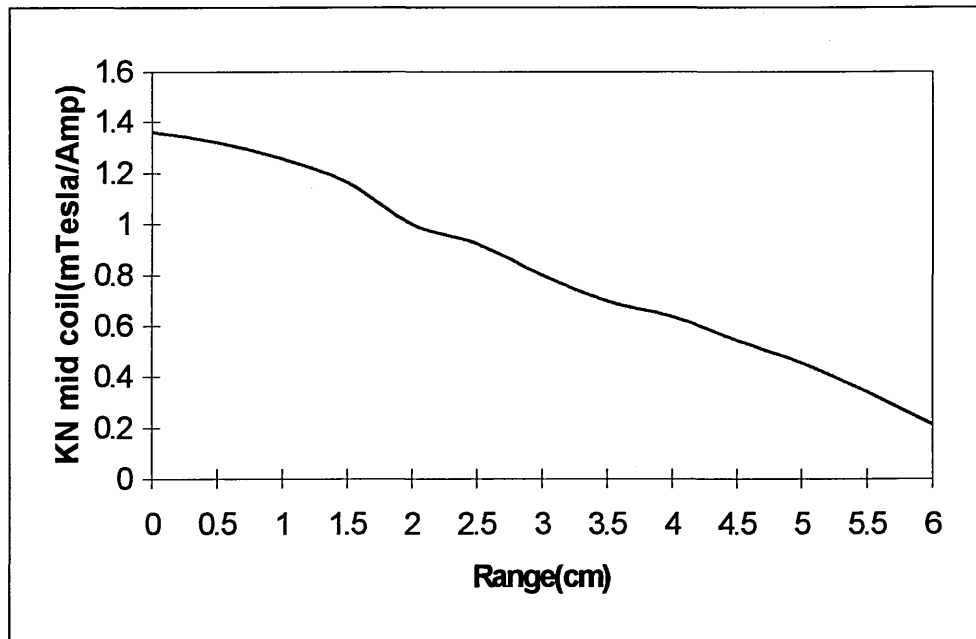
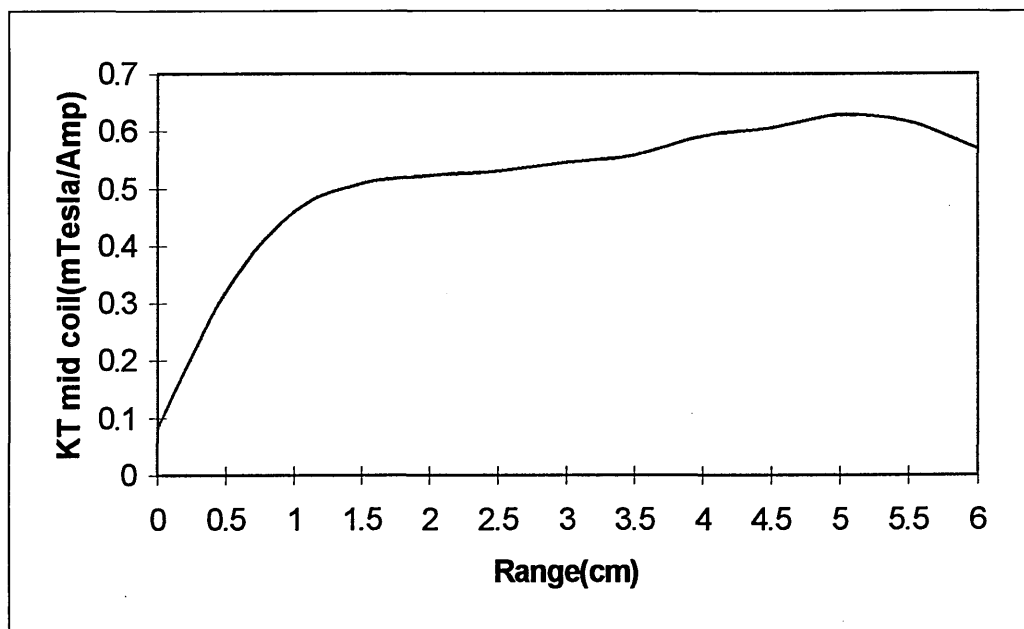


Fig 4.8 (a), Plot of coil constant for the normal component of the magnetic field vs Range for the new middle coil

(b), Plot of coil constant for the transverse component of the magnetic field vs Range for the new middle coil



Coil constants for the new outer coil. Total number of turns= 437

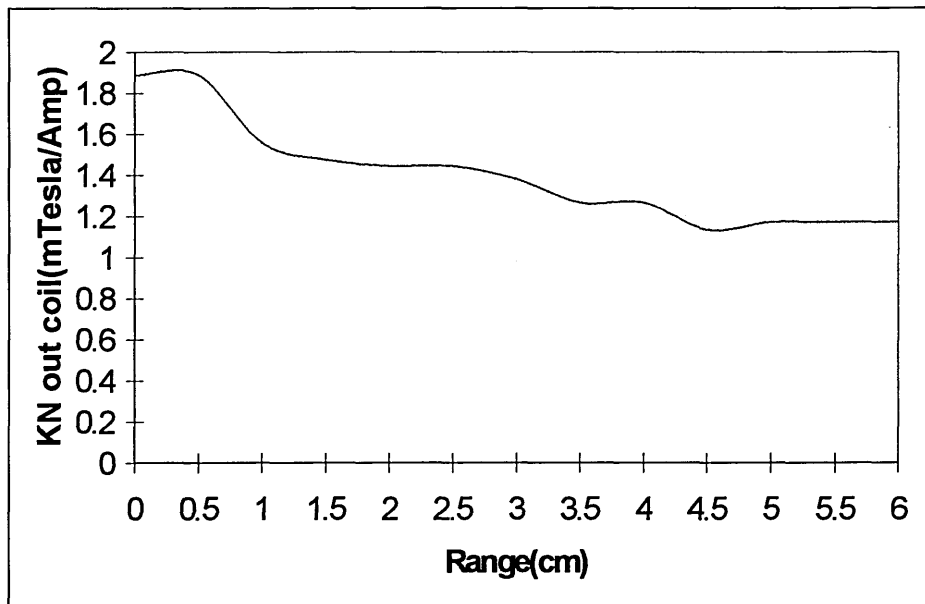
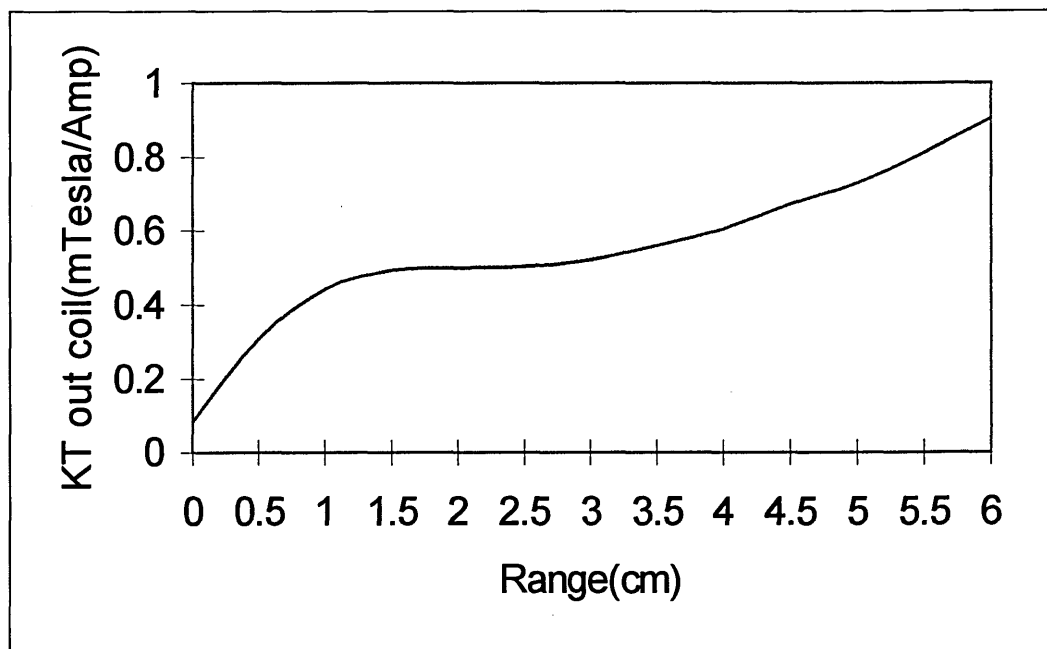


Fig 4.9 (a), Plot of coil constant for the normal component of the magnetic field vs Range for the new outer coil

(b), Plot of coil constant for the transverse component of the magnetic field vs Range for the new outer coil



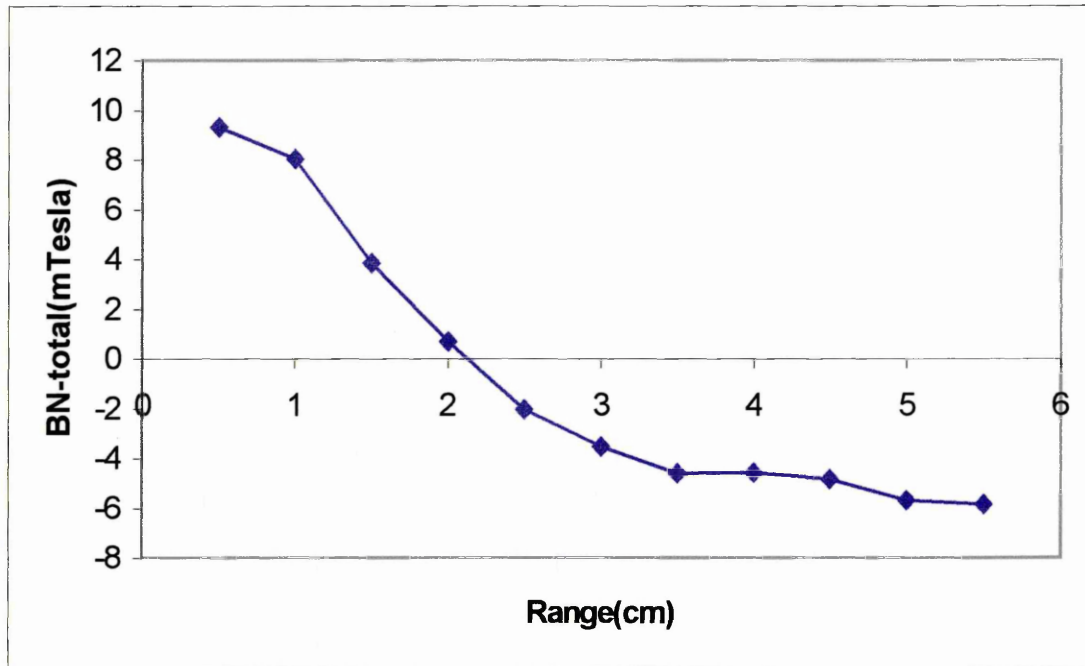


Fig 4.10(a), Plot of $B_N(\text{total})$ vs. Range to illustrate the ability of using coil currents to select orbital radius

4.2.2 WATER COOLED ANODE

In earlier work by Walke[3] a circular spoked brass anode was used which was cooled and powered via a water cooled electrical vacuum feedthrough, attached to one of the side chamber ports. In his work he used the arrangement to monitor the motion of the arc, not to assess the coating performance of the system. Upon beginning the work investigating coatings, Titanium(Ti) was deposited on substrates using a nitrogen reactive gas. The composition of the samples was then analysed using the Glow Discharge Optical Emission Spectrometer(GDOES). The results showed the presence of Zinc(see Fig 4.11 for a GDOES composition plot). After analysis of the materials in the system it was discovered that there was only one possible source of Zinc, the brass anode, hence it was deduced that the heating of the anode during coating was leading to the thermal liberation of Zinc. It had also been observed that during operation the anode became excessively hot leading to deformation. Since coating cycles lasted much longer it was thought that the anode

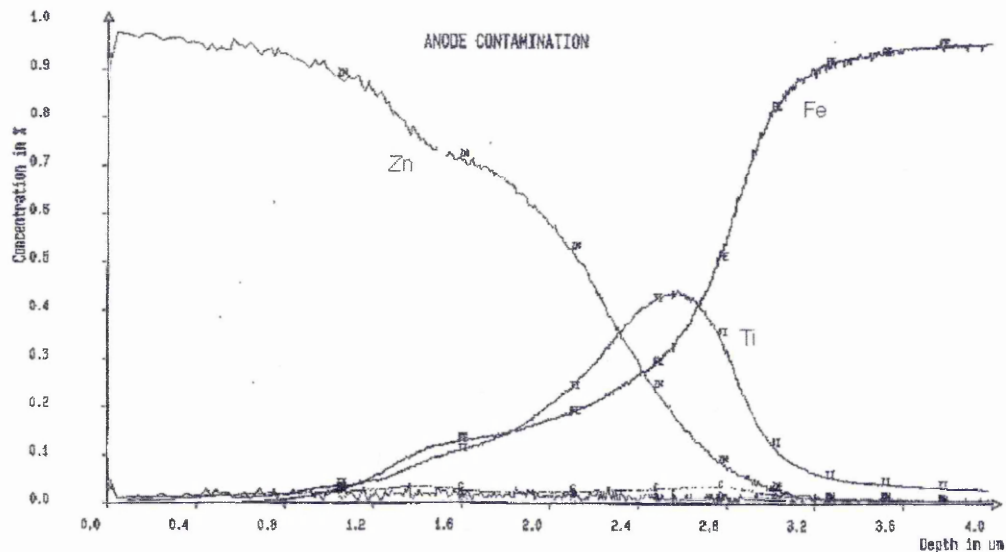


Fig 4.11, GDOES plot showing presence of Zinc in coating

would not survive. Thus a new anode was required which could withstand such temperatures and would not pollute the coatings being deposited. The options were:

- Use a material of higher thermal conductivity
- Construct a new anode with a better cooling system

A combination of the two was chosen. Copper tubing was used to construct a circular hoop(see Appendix C for schematic) which allowed constant water cooling while the arc was operating. Order of magnitude calculations were performed to ascertain whether the tubing could withstand the heat being dissipated.

Using the standard equation for heat conduction it was possible to estimate the temperature difference between the inner and outer wall, ΔT .

$$\Delta T = \frac{\Delta x \times q}{k \times A}$$

where

- ΔT - temperature difference between inner and outer wall of the copper tube
- Δx - thickness of the wall of the pipe
- k - thermal conductivity of the pipe
- q - power directed at the anode(taken to be the total electrical power dissipated)
- A - surface area of the pipe

Considering the performance of microbore tubing with an outer diameter of 6mm, and wall thickness of 0.5mm, produces the following results:

$$\begin{aligned} \text{Surface area of the pipe, } A &= \text{Length of pipe}(l) \times \text{Circumference of the pipe} \\ &= 2\pi R_{\text{anode}} \times 2\pi R_{\text{pipe}} \end{aligned}$$

where the radius of the anode is 50mm

$$\begin{aligned} \text{Power directed at anode, } q &= \text{Voltage} \times \text{Current} \\ &= 30\text{V} \times 80\text{A} = 2.4\text{kW} \end{aligned}$$

Substituting these values into the heat conduction equation gives a temperature difference, ΔT , of 0.43°C . The flow of water was measured at 0.24l/s, assuming that the water enters the anode at 20°C , then this will give values for the temperature of the water and temperature of the anode of 23.75°C and 24.21°C respectively.

Hence from the values of temperature obtained the anode would operate satisfactorily.

After the anode had been constructed the operation was checked using a thermocouple attached to the output water supply, it was found that the water temperature rose approximately 3°C.

4.2.3 SUBSTRATE SHIELD

Before any experiments are performed to test the effect of different parameters on the behaviour of the arc, the cathode must first be cleaned. This cleaning takes the form of a random arc discharge over the surface of the cathode, and continues until the light emitted from the arc is the characteristic colour of that substance*, a process which usually takes approximately 1-2 minutes.

* *light blue for titanium in argon atmosphere*

Since this cleaning has to be undertaken every time the chamber has been exposed to air a shielding mechanism must be employed to protect any samples to be coated from the flux generated by the random arc cleaning phase. Two different shield mechanisms were designed for different coating arrangements, full schematics of each of these designs can be seen in Appendix C.

a) *Pulley shield*

This design incorporates a pulley system to raise and lower the shield, see Fig 4.12. Here a handle is connected to the pulley chain via a rotary vacuum feedthrough. As the handle is turned the chain is tensioned and the shield rises exposing the sample.

b) *Rotary shield*

This shield uses a curved piece of metal to protect the seven samples used for macroparticle experiments (chapter 6). A sketch of this arrangement is shown as Fig 4.13. Here a rod inside the chamber is connected to both the shield and the handle outside the chamber, thus turning the handle exposes the seven samples to the flux from the cathode.

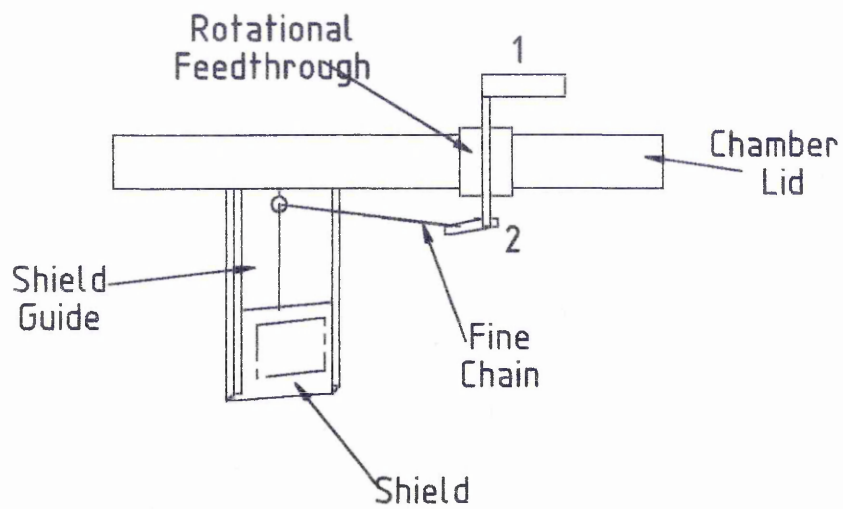


Fig 4.12, Sketch of single sample shield

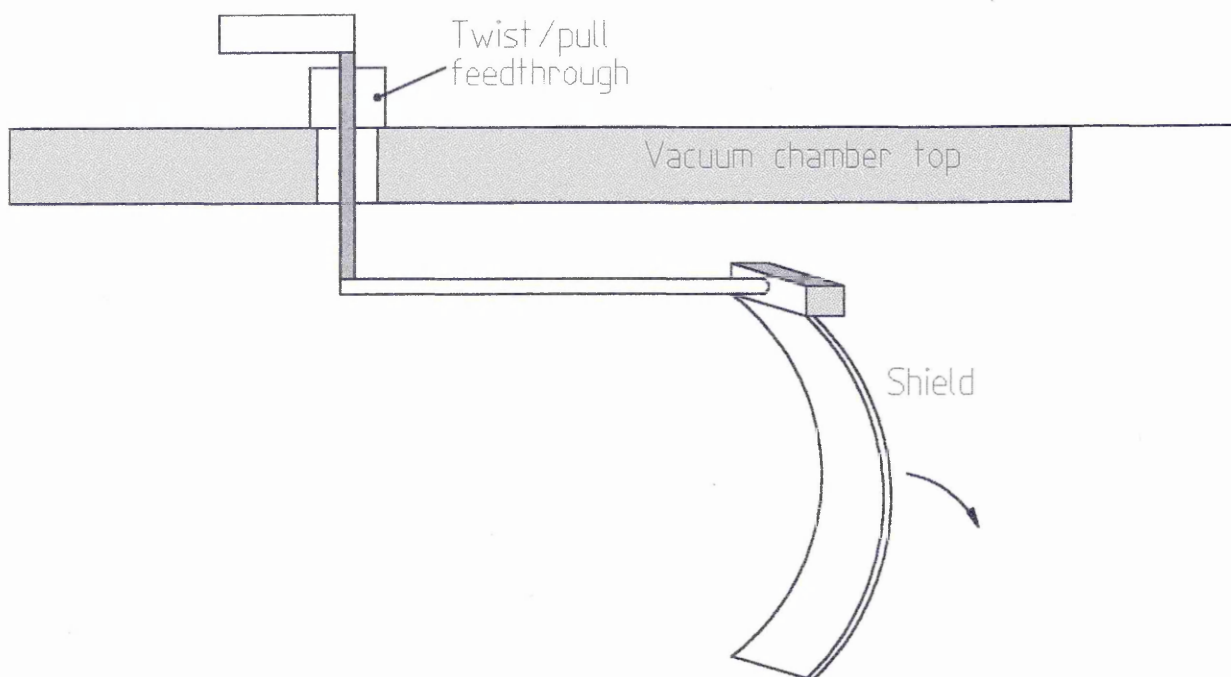


Fig 4.13, Sketch of rotary shield mechanism

4.2.4 SUBSTRATE HOLDER

As well as observing the arc motion it was also desirable to study the effect of the magnetic steering field on the production and distribution of macroparticles. To investigate this effect a substrate holder was designed and built. The holder consisted of two parts:

- A plate to attach to the port in the side of the chamber. This plate allowed cooling of the sample holder to be achieved, and could be used to coat a single sample or alternatively seven samples with the attachment described below. There was also the facility to insulate the samples from the chamber, by means of a PTFE washer, thus allowing the substrates to be negatively biased.
- A curved sample holder allowing up to seven samples to be coated at different angles with respect to the cathode. The curve of the holder was such that the substrates on each section were equidistant from the 2cm orbit on which the arc was moving.

A sketch of this arrangement, Fig 4.14, is shown below, it should be noted that the anode is not shown in this sketch.

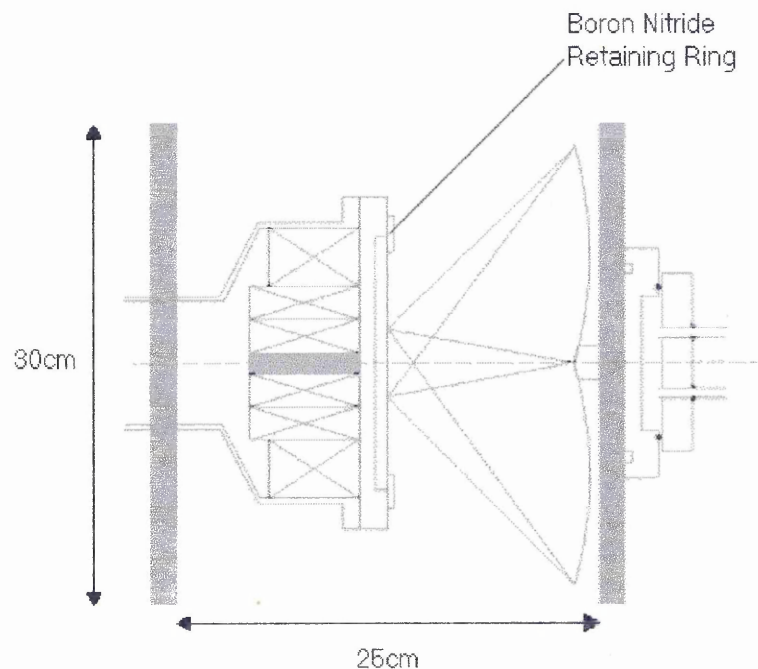


Fig 4.14, Sketch of sample holder in situ in the vacuum chamber

4.3 Apparatus Used

This section describes the design of the experimental vacuum system, the power supplies and the associated control systems used for the experiments covered in chapters 5 and 6. A sketch of the system with all its components is shown as Fig 4.15.

4.3.1 MAIN CHAMBER AND PUMPING SYSTEM

The chamber and control systems were designed by Dr P J Walke and Dr R New for the purpose of previous PhD work[3], and consist of a cylindrical aluminium vacuum chamber mounted on a modified Genevac evaporation unit. The manufacture of the rig was performed by Mr R Day and Mr G Robinson at the Materials Research Institute, Sheffield Hallam University. The pumping arrangement consisted of a diffusion pump, with a 20cm

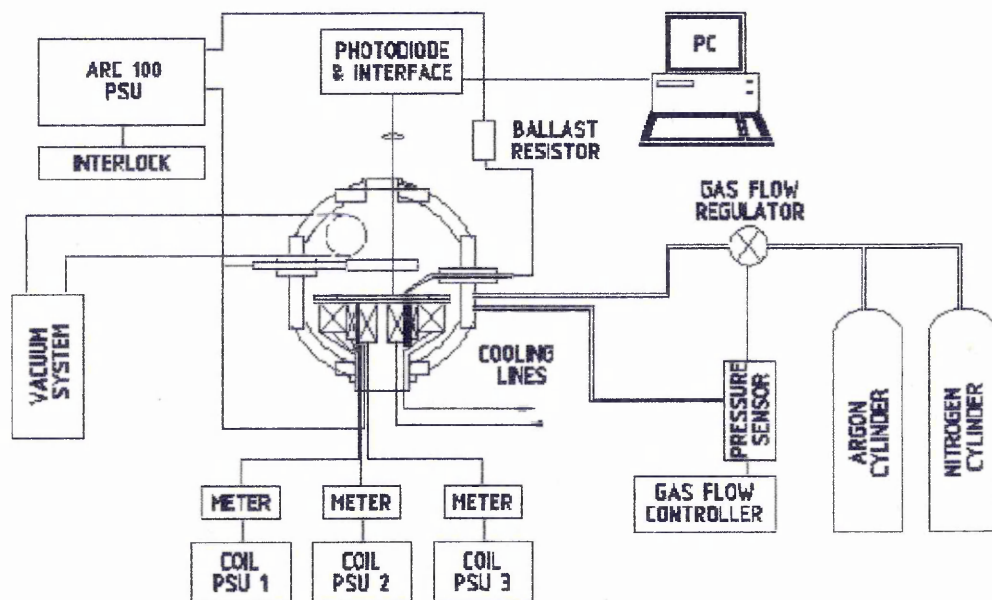


Fig 4.15, Overview of experimental system

throat, which was backed by a rotary pump. The combination of the two pumps produced a total pumping capacity of 1300ls^{-1} . Access to the chamber was either by the circular top plate of the chamber, by which the chamber was earthed, or by one of the four ports in the

side of the chamber. The ports are orthogonal to each other and consist of circular openings (10cm in diameter) covered by square metal plates with o-ring seals. The metal plates are then used to attach various components to the vacuum chamber. The port assignments are as follows:

1. This port is used to provide access to the cathode assembly, so that water and electrical supplies can be connected to the electromagnetic steering array and cathode assembly.
2. This port supports the water cooled anode.
3. This plate supports several systems:
 - Electrical feedthrough for the monal arc striker which is connected to a high current supply via a current limiting ballast resistor.
 - Gas feedthrough for the supply of a backing gas
 - Pressure transducer connected to the gas control apparatus
4. This port is dual purpose as it is directly facing the cathode:
 - Line of sight viewing port - used in conjunction with the photodiode array(see chapter 5) for the measurement of velocity and confinement of the arc.
 - Substrate holder port - where the substrate holder can be attached to perform experiments to investigate the distribution of macroparticles.

Once the entire vacuum system had been assembled a good seal was achieved producing a base pressure of below 1×10^{-5} torr.

4.3.2 THE POWER SUPPLIES

Five power supplies were used to power the system:

- "Arc 100" supply unit - This is used to provide the arc current and was manufactured by ELMA Technik GmbH. The supply gave a fixed current in the range of 0 to 100A at voltages of up to 100V. A safety interlock was also built into this supply whereby a 5V signal was required to enable the unit, hence a remote switch was used.

- Two constant current supplies with feedback stabilisation providing 20A and 10A and a variable, regulated voltage output, 18A supply - These were used in various combinations to power the electromagnetic steering coils.
- A twin stabilised 30V supply was used, linked in series, to produce a -40V bias voltage(with respect to ground)

4.3.3 THE GAS CONTROL SYSTEM

The pressure of the backing gas was controlled using an MKS250 gas controller in conjunction with a MKS baratron 122A pressure transducer, and a MKS 248 solenoid valve. The gas controller allowed the chamber pressure to be set with a high degree of accuracy(0.25% of reading) over a wide range of pressures. The transducer was an absolute pressure gauge(capacitance manometer type) giving an operational range of 3×10^{-4} torr to 1 torr($\pm 0.5\%$). This gauge also produces an absolute measure of pressure meaning that no additional corrections are required for different backing gases.

REFERENCES

- [1] S Ramalingham
US Patent No. 4,763,477(1987)

- [2] P D Swift, D R McKenzie, I S Falconer
Journal of Physics D: Applied Physics, 66(2) (1989) 505

- [3] P J Walke
PhD Thesis, Sheffield Hallam University, September 1994

- [4] A A Plyutto, V N Ryzhkov, A T Kapin
Soviet Physics JETP, 20 (1965) 328

- [5] W D Davis, H C Miller
Journal of Applied Physics, 40 (1969) 2212

- [6] C M Care
Journal of Physics D: Applied Physics, 25(12) (1992) 1841

5.0 EXPERIMENTAL STUDIES OF THE ARC MOTION

As has been mentioned in chapter 2 various authors have attempted to model the behaviour of the random arc, with one such approach being based on stochastic behaviour. A stochastic model by Care[1] further developed this approach, treating the motion of the steered arc spot as a random walk influenced by the two components (B_N' and B_T) of the applied magnetic field. In this model the confinement of the arc was affected by both components B_N' and B_T , whereas the motion along the path of $B_N=0$ was only influenced by B_T .

In this chapter the motion of the arc, as a function of magnetic field components, is studied experimentally. Such experiments allow the stochastic model by Care to be tested.

The chapter is divided into several sections:

- 5.1 Introduction to the stochastic model
- 5.2 Analysis of the arc motion. This section describes the electronics and software operation which were used to detect the motion of the arc.
- 5.3 Measurement of the arc confinement. Here the results of the experiments to monitor the radial motion of the arc are presented.
- 5.4 Measurement of the distribution of orbital transit times. Here results are presented which highlight the effect of the magnetic field components upon the orbital motion of the arc. Also included are explanations of the distribution of transit times and the fitting of experimental data to theoretical distributions.

5.1 Introduction to the Stochastic Model

The following is a brief section which aims to describe and summarise both the key elements of the model, and the solution to the stochastic model described in 2.2.2(e), with attention focussing upon the probability density for the position of the arc in the orbital and radial directions.

The equation for the time dependent probability density for the position of the arc in both directions is shown as EQ2.4 in chapter 2. In order that an analytical solution to the equation be reached two assumptions are made:

- The velocity of the arc is related linearly to B_T , which is probable over the limited range of settings under consideration
i.e. $c = K_c B_T$, where c is the velocity of the arc and K_c is a constant
- The confinement of the arc is achieved by a restoring force, $f(x)$, with the form
i.e. $f(x) = K_f B_N' B_T x$, where K_f is a constant and x is the distance of the arc from the path where $B_N=0$

It should be noted that for the purpose of this thesis that diffusion constants in both radial and orbital directions are considered equal ($D_x=D_y$). With these approximations an analytical solution to EQ2.4 can be obtained[1].

$$\phi(x, y, t) = \frac{1}{2\pi L^2} \sqrt{\frac{1}{2t/t_0}} \exp\left[-\frac{(y/L + c^*t/t_0)^2}{4t/t_0}\right] \times \exp\left[\frac{(x/L)^2}{2}\right] \sum_{m=0}^{\infty} \frac{(-1)^m}{2^{2m}(m!)} \exp[-2mt/t_0] H_{2m}\left(x/(\sqrt{2L})\right) \quad \text{EQ 5.1}$$

Here $H_n(x)$ is a hermite polynomial[2] of the order n , and the characteristic time(t_0), characteristic length(L) and dimensionless quantity c^* are defined as

$$t_0 = \frac{1}{K_f B_N' B_T} \quad L = \sqrt{D_x t_0} \quad c^* = \frac{c t_0}{L} \quad \text{EQ 5.2}$$

The behaviour of this solution can be demonstrated in the radial and orbital directions by superimposing a mean velocity, c , upon the distribution and examining it.

If we substitute for c^* and consider ϕ at long times only the m_0 term survives which is equal to 1, so that

$$\phi(x, y, t) = \frac{1}{2\pi L^2} \sqrt{\frac{1}{2t/t_0}} \exp\left(\frac{-(y + ct)^2}{4D_x t}\right) \exp\left(\frac{-x^2}{2(D_x / K_f B_N' B_T)}\right) \quad \text{EQ 5.3}$$

This simplified version of EQ 5.1 allows the behaviour arc motion in both directions to be determined:

- In the radial(x) direction the function spreads out with time leading to a gaussian whose width is governed by the diffusion constant, B_N' and B_T .
- In the orbital(y) direction the arc moves at a mean velocity(determined by the magnitude of B_T) and diffuses about its mean position, unconfined, at a rate governed by the diffusion coefficient.

5.2 Analysis of the Arc Motion

The aim of this work was to examine the orbital motion of the arc as a function of magnetic field. To perform these measurements it was considered that an improvement in the arc analysis method was required. Previously[3] separate experiments were performed to measure the following:

a) *Velocity of the arc* - A lens was used to image the arc track. A pulse was then produced when the image of the cathode spot crossed a slit placed in front of a large area photodiode. It was possible to measure the time elapsed between consecutive pulses which were processed by computer.

b) *Confinement of the arc* - This parameter was obtained by measuring photographs of the arc's motion. The pictures were taken using a camera, whose exposure time was such that an entire orbit of the arc was captured per frame.

In order to produce improvements various methods were considered, from charged coupled devices(CCD) to photodiodes. After consideration the final system was constructed incorporating a linear photodiode array in place of the large area detector discussed above in (a). Such a configuration allowed the simultaneous measurement of the velocity and confinement of the arc, thus allowing the automation of much of the data processing. A sketch of the arrangement, which consists of four parts, is shown as fig 5.1. Using the photodiode array approach allows the measurement of the velocity by detecting a pulse from any element(s), with positional information being determined from which of the elements were illuminated.

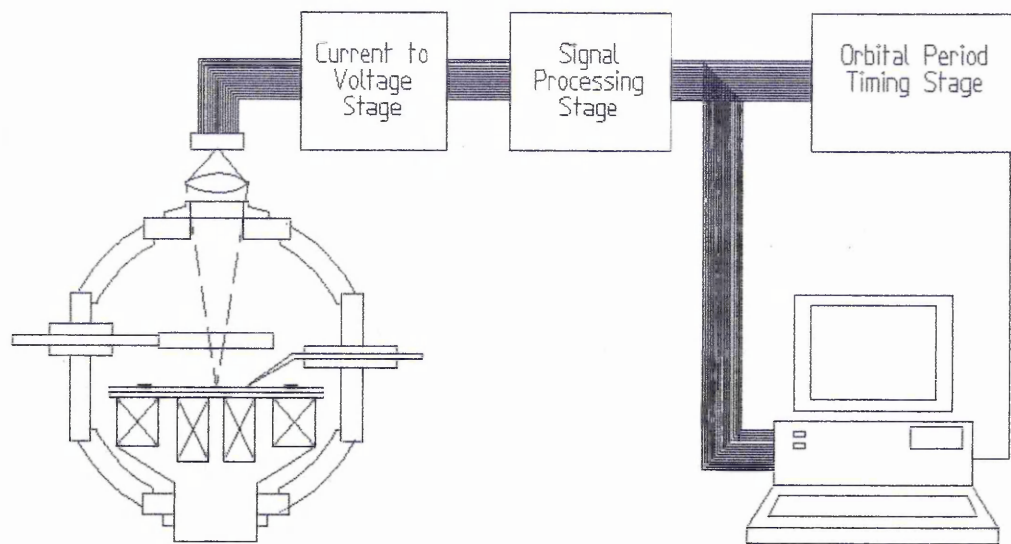


Fig 5.1, Block diagram of the photodiode array circuitry

Photodiode array

The light from a section of the arc's orbit is projected onto the detector array, producing a current. Detailed information regarding the detector array can be seen in Appendix C, in the form of the product data sheet. A sketch of the array can be seen as fig 5.2. From this diagram it should be noted that the design of the array allows for the interconnection, "daisy chaining", of several arrays to provide greater width.

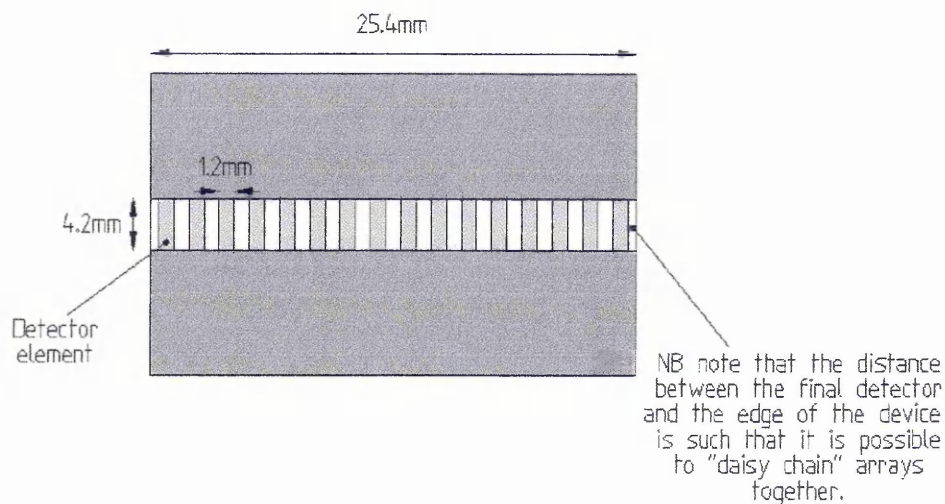


Fig 5.2, Sketch of the photodiode array

Current to voltage stage

The current produced by the photodiode is taken and converted to a voltage proportional to the light intensity falling upon the detector. The conversion stage uses a high gain low noise circuit[4], fig 5.3, similar to the circuit used by Walke et al[3]. The design has been modified due to the photodiode array being of common cathode configuration.

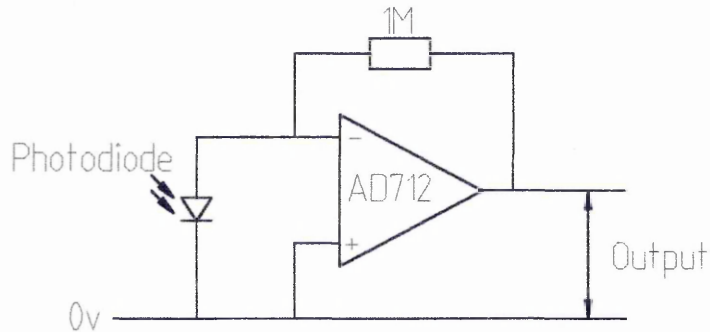


Fig 5.3, Sketch of the high gain low noise circuit for current to voltage stage.

Signal processing stage

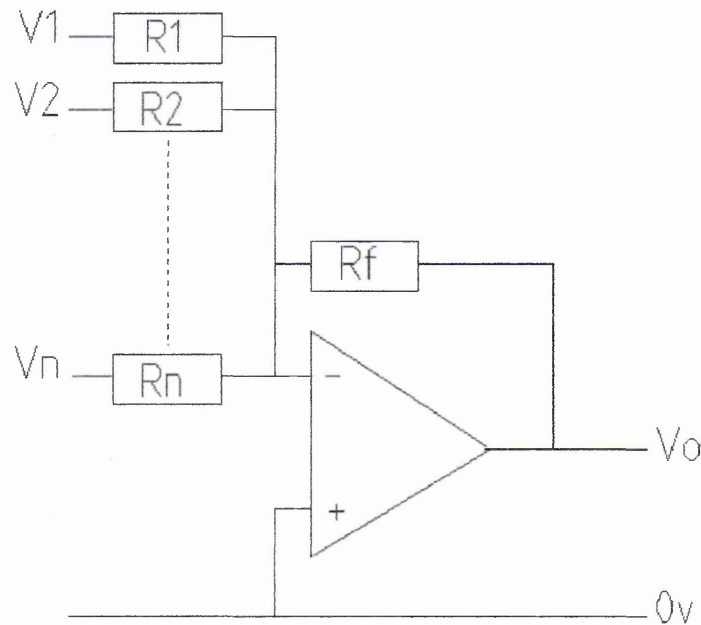
Now the amplified signal passes to a comparator, to give the pulse a sharp edge, where the photodiode voltage is compared to a preset threshold voltage. The discriminating voltage was determined experimentally so that it was possible to distinguish the ambient background light from the illumination of the array by the arc spot. The output from the comparator was a pulse of either 5V or 0V, this pulse is then elongated by passage through a monostable multivibrator. The extension of the pulse is obtained by locking the trigger input (from the comparator), via a resistor capacitor network. The reason for this stage is to prolong the pulse so that any random backward motion of the arc does not generate spurious additional pulses. During experimental testing of the circuitry it was found that it was desirable to have shorter duration pulses for optimum measurement of velocity than for confinement measurements.

N.B. It should be noted that each photodiode element had its own amplification and signal processing stage.

After the signal had been processed the resulting pulses from the sixteen detectors were then directed to two places. Firstly they were passed to the PC for collection, via a National Instruments PC-DIO-96 digital interface card, and secondly to the orbital period timing circuitry. The digital interface card allowed information on the state of the 16 photodiodes to be stored, for confinement analysis later.

Orbital Period Timing circuitry

This stage takes the sixteen individual signals from the detector array and combines them, using a summing amplifier, to produce an output pulse whenever one or more of the elements are illuminated (see Figure 5.4). The output from here is then fed to the data acquisition card, National Instruments ATMIO-16, which is being used for timing the arc period. By using this card it was possible to measure the period of the arc orbit as well as acting as a trigger for the confinement measurement routine.



$$V_{OUT} = -R_f \left(\frac{V_1}{R_1} + \frac{V_2}{R_2} + \dots + \frac{V_n}{R_n} \right)$$

Fig 5.4, Diagram of the summing amplifier assembly used

A complete diagram of the monitoring circuit is shown below as Fig 5.5.

Testing and evaluation of the detection circuitry

Once the electronic circuit had been designed and constructed, then the system required commissioning. The main aim of this stage of work was to check that the circuit had been constructed correctly and that the outputs from the electronics provided sensible experimental data. Before such examination of results could be undertaken the most appropriate value for the reference voltage level (V_{ref}) for the comparator had to be determined.

To define the level of this threshold all the elements of the array, bar one, were masked. This single exposed element was located about the position where the arc would pass ($B_N=0$ position of $r=22\text{mm}$), and the output of the relevant amplifier

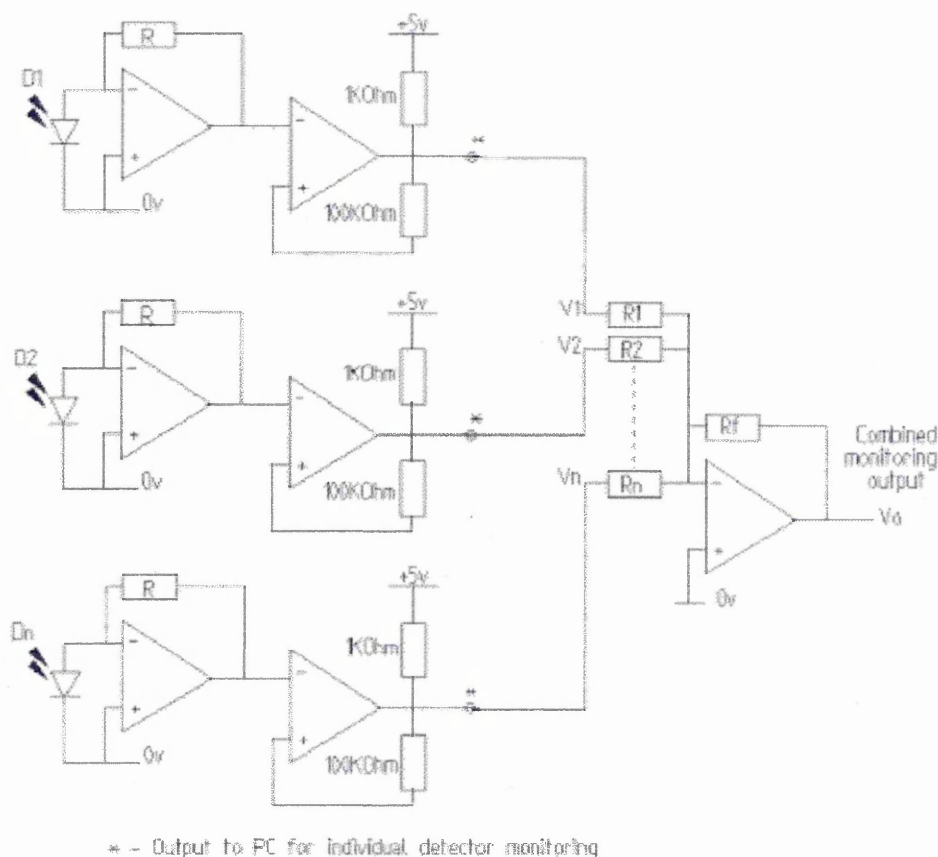


Fig 5.5, Diagram of the entire monitoring circuit

attached to an oscilloscope. An arc was then struck and the output voltage monitored for a short while, thus allowing a value for V_{ref} to be arrived at. Once this had been set then it was possible to “fine tune” the magnitude of V_{ref} to minimise erroneous switching of the counter. Such fine tuning was performed by utilising the arc timing program (for greater operational detail see next section).

The next step involved checking that the results being obtained were indeed being caused by the arc illuminating an element. This assessment was performed by again masking all but one of the detectors, this exposed detector was placed on the 22mm datum, the arc timing program was started and an arc struck. Once the preset number of orbits had been completed the individual element data was analysed and it was found that only the uncovered detector registered pulses showing that the circuit was functioning within design parameters. In addition to the above it was also possible to

check the arc timing circuit by modulating a light source and illuminating the element and then analysing the velocity data.

The next stage was now to test the detection system in a real life situation, by operating the arc under conditions and steering field values used by other authors[3, 7, 8]. Once the arc had been struck and the desired number of orbits sampled the data was saved to computer. Upon analysis of this file it was found that the confinement data agreed with the work of previous authors[3, 7, 8], though it was noted that a number of erroneous readings were included in the results file. Such erroneous reading had also been encountered by Walke[3] and were overcome by incorporating a filtering mechanism in the arc timing software. To eliminate/minimise the occurrence of the errors a similar filtering technique was used, in this application though two different filtering processes were required:

- (i) Removal of erroneous orbital period data – This process involved examining the data and calculating a preliminary value for the standard deviation from the mean velocity, once this had been arrived at the data was filtered and all values outside the ± 3 standard deviations were rejected and a new value for mean velocity of the arc calculated.
- (ii) Removal of erroneous elemental data – in order to make sure that no corruption of data was encountered the array of elemental data was scanned and any results in which 2 or more segments had been illuminated were rejected. Random examination of the raw experimental data showed that the arc did not illuminate adjacent segments simultaneously and hence this did not effect the final σ result. The occurrence of such random glitches could be due to the extremely electrically noisy environment in which the system was operating.

Alignment and resolution of the system

In order to truly establish a value for σ for an experiment careful consideration of the optical layout of the detection system had to be considered. To provide a true picture of the motion of the arc deviation from the $B_N=0$ the photodiode array had to be centred upon the track described by the $B_N=0$ position($r=22\text{mm}$) (see Figure 5.7). The extent of these deviations had also to be considered, in order to make a decision as to the extent of the deviations work by Walke et al was used as a guideline. In this previous work he experienced values of σ in the order of 2.5mm, thus it was decided to make sure that a sufficient range of radial movement by monitoring $\pm 5\text{mm}$ about the track. Thus it was

possible to position the lens correctly in relation to the cathode and photodiodes and also to derive an algebraic expression to calculate the distance between the $B_N=0$ position and that of the arc as it passed the detection system. Such a formula would be dependent upon the focal length of the lens, the distance between the cathode and the lens(object distance), and the distance between the array and the lens.

Program operation

The program used for data acquisition was written using the National Instruments Lab Windows software package. This software controls various computer interface cards to enable the sampling and storage of data. For the research presented here two such cards were used:

- **PCDIO-96 - Digital Interface Card**

This interface card has 96 digital inputs. In our experiments only sixteen of these inputs were used, but if greater accuracy is required it would be possible to link several arrays together.

- **ATMIO-16 Data Acquisition Card**

This is a general purpose data acquisition card, containing counters and both analogue and digital inputs and outputs. For the purpose of these experiments only the counters were used. This card was connected to the output of the orbital period monitoring stage to enable the timing of the arc period, and also the triggering of the confinement measuring routine.

The program used in this work has been developed from code written by Walke[3] to measure the velocity of the arc. A flowchart of the program, Fig 5.6(a), shows a simplified explanation of its operation, with the full program listing in Appendix B.

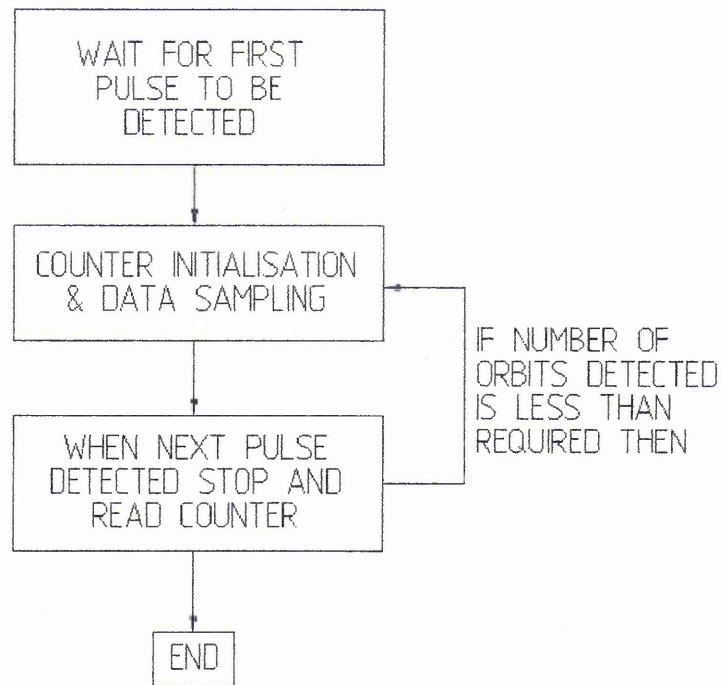
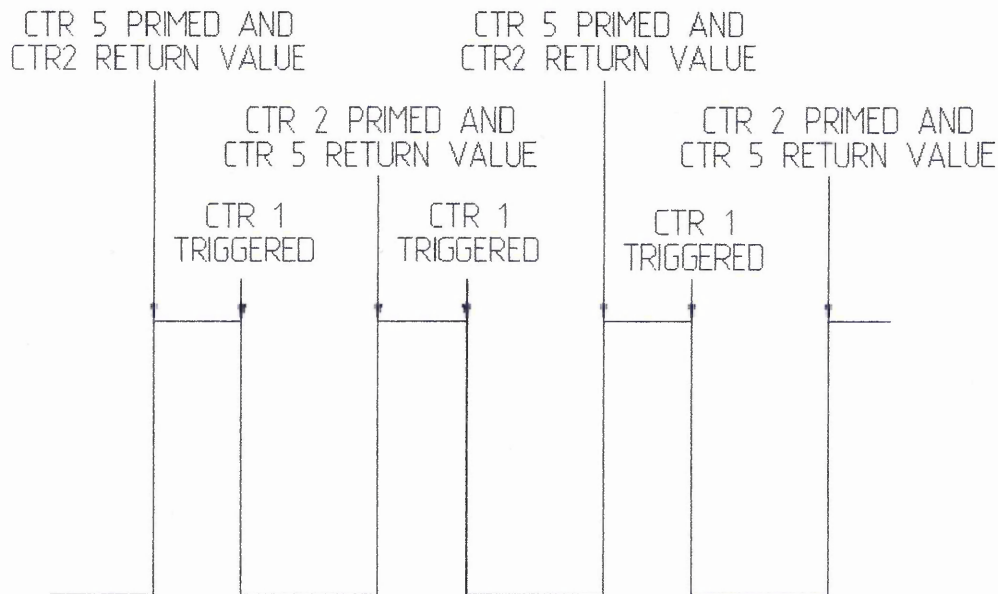


Fig 5.6(a), Flowchart of the arc detection program

Fig 5.6(b), Sketch of the program operation in relation to the input pulses



As can be seen from fig 5.6(b) three counters are used in order that all pulses passing the detector array are measured, these are labelled as counters 1, 2 and 5. Here counters 2 and 5 are used to time the periods between pulses(using the positive edge to trigger) and counter 1 is used to co-ordinate the whole timing process(using the negative edge to trigger). This diagram shows the workings of the program in relation to the

occurrence of events at the detectors. The program itself has three stages:

1. *Detection of the first pulse*

The computer continuously monitors the output of the detectors, using the output of the orbital period timing circuitry.

2. *Counter initialisation and data sampling*

Once the pulse has been detected, by the triggering of counter 1, counter 2 is read and counter 5 is primed. Then the value obtained from counter 2 is stored as the period of the arc, it should be noted that the first time around this loop counter 2 will produce no useful data as this serves to prime counter 2. In addition to this the 16 detectors are sampled to check their status, and the information is stored in an array.

3. *Waiting for another pulse to occur*

Once another pulse is detected, via counter 1, counter 5 is read and counter 2 is primed. Thus the value on counter 5 is saved as the period of the arc. The program will then return to step 2 until the desired number of orbits have been achieved.

It should be noted that the number of orbits being measured by the program also depends upon the deposition rate of the titanium on the glass observation window. This deposition turns the glass from transparent into a mirror at different rates dependent on the velocity and confinement of the arc. A smaller number of orbits were studied in each experimental run in this work than those monitored by Walke[3]. This was due to the expansion of the image of the arc track to cover all 16 detectors, for confinement measurements, thus decreasing the intensity of the illumination from the arc. A more detailed explanation of the arc velocity section of the program can be seen in the thesis of Walke[3].

5.3 Measurement of Arc Confinement

5.3.1 INTRODUCTION

As was described in 5.1 the probability density function of the arc in the radial direction, at long times, becomes gaussian with a half width L .

$$\text{i.e. } \varphi(x,t) = \frac{1}{\sqrt{2\pi}L} \exp\left[-\frac{1}{2}\left(\frac{x}{L}\right)^2\right] \quad \text{EQ 5.4}$$

Hence the probability of finding the arc spot a certain distance from the track should have a normal distribution with a width proportional to $1/\sqrt{B_N' B_T}$, as

$$L \propto 1/\sqrt{B_N' B_T} \quad \text{EQ 5.5}$$

This section describes the experimental measurement of the deviation of the arc from the path $B_N=0$ as a function of B_N' and B_T and compares the results to EQ 5.4

5.3.2 EXPERIMENTAL DETAILS

Using the apparatus as shown below(see chapter 4 for greater detail) measurements were made of the distribution of arc radii for a variety of combinations of normal field gradient(B_N') and transverse field(B_T).

Using the combinations of the various coil settings it was possible to vary the values of B_N' and B_T whilst maintaining an orbital radius of 22mm. Utilising the linear photodiode array and associated circuitry, as described in 5.2, the orbital radii of 500 arc orbits could be recorded. A computer program was then applied to these data files to calculate a value for the standard deviation of the arc track.

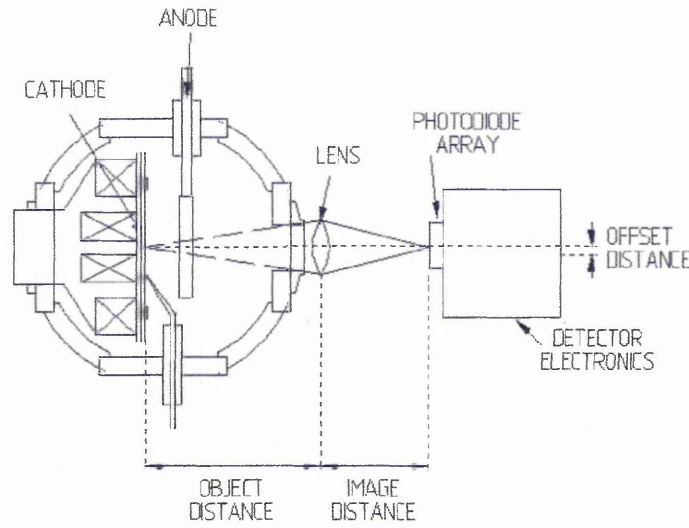


Fig 5.7, Sketch of the arrangement of the photodiode and associated optics used

Using the measurement of distance between the optical components and the dimensions of the photodiode array it was possible to convert the experimental records of which detector had been illuminated into deviations of the arc track in mm. Thus using this method of arc monitoring it was possible to improve the efficiency of experimental data capture over the method previously used by Walke[3].

5.3.3 RESULTS

Table 5.2(a) shows the results of the measurement of the standard deviation of the radius of the arc track (σ) for a variety of magnetic field settings, along with the standard error (s.err) and coil settings required. In addition to this data set, a reduced set was compiled by averaging settings of similar field settings. This data set can be seen as table 5.2(b). The equation for the probability of finding an arc spot a certain distance from the track centre, EQ 5.5, predicts that a graph of σ vs. $(B_N' B_T)^{-0.5}$ should be a straight line passing through the origin. In order to accurately derive the powers of B_N' and B_T two different methods were used.

Method 1

In the first option values for σ , presented here as table 5.2(a), were combined with the results from previous work[3] to produce a single larger data set. An equation solving routine in MS Excel was then used to obtain values for the powers to which B_N' and B_T are raised in equation 5.5. To ascertain the “best fit” values the variables were adjusted until the sum of squares of $(\text{measured } \sigma - (\text{constant} * B_N'^x * B_T^y))$ was at a minimum.

After such a routine the program found the values to be $x=-0.35$ and $y=-0.75$, differing from the stochastic model by Care. The next stage of this

Table 5.2(a), Summary of experimental results and settings

Standard Deviation, σ , of arc(mm)	Standard error in σ	Number of readings in data set	$(B_N' B_T)^{-0.5}$ ($mT^{-1} m^{0.5}$)	B_N' ($mT m^{-1}$)	B_T (mT)	B_N'/B_T (m^{-1})
2.2	0.11	384	0.01938	428.07	6.22	68.8
2.29	0.12	363	0.01932	429.36	6.24	68.8
2.12	0.11	360	0.01923	431.18	6.27	68.7
1.93	0.10	365	0.01691	493.98	7.08	69.8
1.85	0.09	396	0.16996	491.83	7.04	69.9
1.89	0.10	346	0.01694	493.34	7.06	69.9
1.4	0.07	446	0.01344	639.67	8.66	73.9
1.52	0.07	495	0.01334	642.71	8.74	73.5
1.28	0.06	466	0.01345	638.31	8.66	73.7
1.3	0.06	498	0.01338	640.28	8.73	73.3
1.3	0.07	349	0.01162	674.80	10.98	61.5
1.33	0.07	329	0.01180	689.43	11.24	61.3
1.18	0.06	350	0.01046	748.83	12.20	61.4
0.94	0.04	496	0.01047	748.17	12.20	61.3
1.12	0.05	447	0.01037	755.37	12.32	61.3
1.63	0.08	379	0.01035	755.77	12.35	61.2
0.85	0.05	342	0.00907	864.96	14.06	61.5
0.87	0.05	312	0.00900	870.74	14.19	61.4
0.87	0.05	321	0.00894	876.50	14.28	61.4
1.08	0.06	288	0.00892	878.72	14.32	61.4
0.89	0.04	492	0.00892	878.61	14.31	61.4

examination was to assess the error limits for such a fit. The value for error was estimated by adjusting the values of x and y and viewing their impact on the results by plotting σ vs. $B_N' B_T^y$. It was found that as x and y were adjusted away from their optimal values then the two original data sets would separate out. Fig 5.8 illustrates an example of a poor fit.

Table 5.2(b), Reduced experimental data set

B_N' (mTm ⁻¹)	B_T (mT)	Standard Deviation, σ , of arc(mm)	Error in σ (mm)
429.54	6.25	2.20	0.1
493.05	7.06	1.89	0.05
640.24	8.70	1.38	0.1
682.14	11.11	1.32	0.02
750.79	12.24	1.15	0.34
872.70	14.21	0.87	0.1

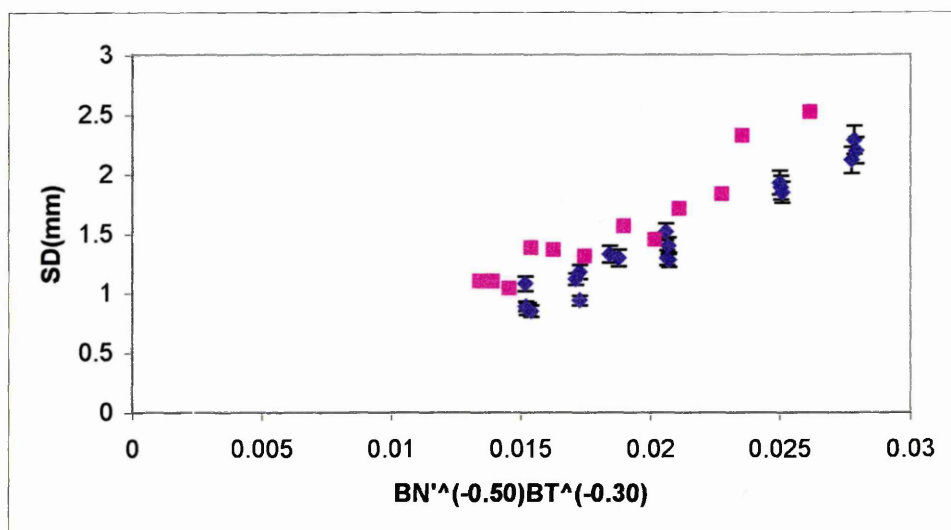
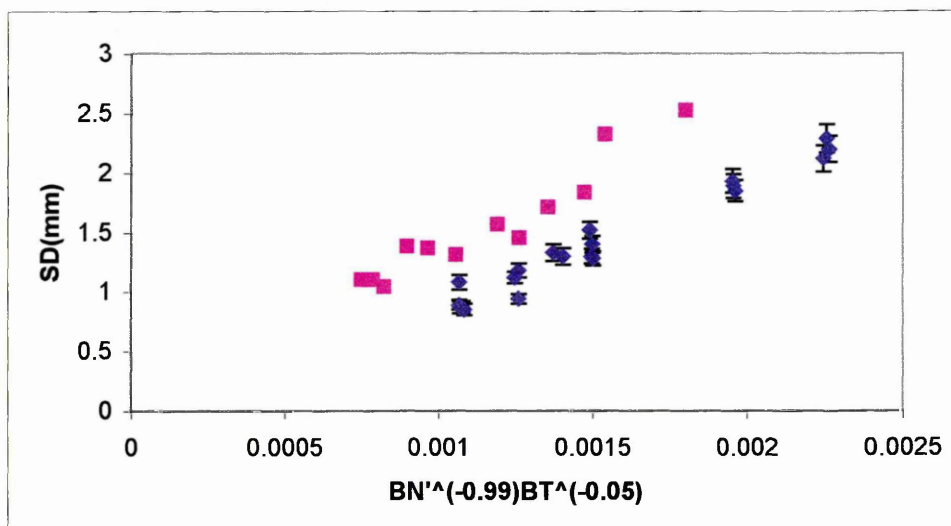


Fig 5.8 (a) Illustration of the separation of the data set by varying x and y

(b) Illustration of values of x and y which produce a greater separation of data sets.



The point at which this separation began to occur was thus judged by eye for a range of values. Once all the permutations had been considered a final value for the error in the fit was arrived at and is below. A plot of this relationship can be seen as Fig 5.9.

$$\sigma \propto B_N'^{-(0.35 \pm 0.35)} B_T^{-(0.75 \pm 0.25)}$$

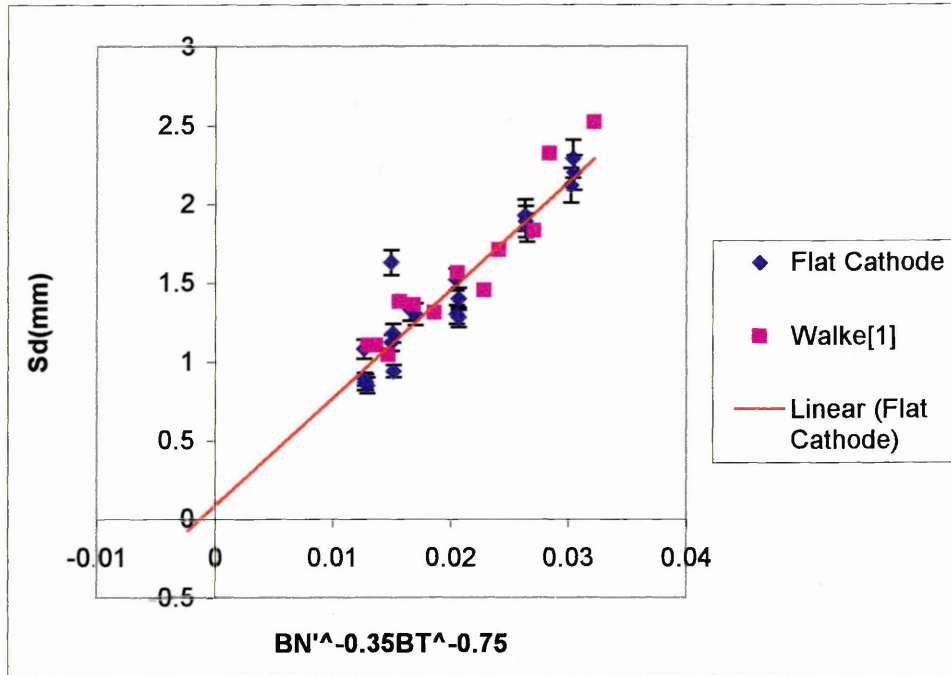


Fig 5.9, Plot of σ vs. $B_N'^{-(0.35)} B_T^{-(0.75)}$, using the data set based on table 5.2(a)

Method 2

The second method used involved a much more analytical approach based upon a standard statistical technique [11]. This uses the reduced data set to reduce the complexity of the fitting routine, the data can be seen as Table 5.2(b). We expect from Care[1] that

$$\sigma \propto B_N'^{(x)} B_T^{(y)}$$

$$\text{ie } \sigma = k B_N'^{-(x)} B_T^{(y)}, \text{ where } k \text{ is a constant} \quad \text{EQ 5.6}$$

In order to arrive at values for the powers of B_N' and B_T , logs. are taken of EQ 5.6 which produces the expression below

$$\text{Log } \sigma = \text{Log } k + x \text{ Log } B_N' + y \text{ Log } B_T \quad \text{EQ 5.7}$$

Using the results from table 5.2(a) it is now possible (given values of k , x and y) to calculate a value for σ , let us call it $\sigma(\text{eq})$. In order to check the accuracy of the fit

between calculated and experimental values for σ the least squared method was used[11]. The value for χ^2 was derived , as shown below, which allowed this judgement to be made.

$$\chi^2 = \sum \left(\frac{(\sigma - \sigma(eq))^2}{(SE of \sigma)^2} \right), \text{ where SE } \sigma \text{ is the standard error of } \sigma$$

Hence by varying the values of k, x and y a range of χ^2 values can be obtained, where χ^2 will be a minimum for the best fit.

Constraints on the values of x and y

If we assume that for the experimental arrangement outlined in this thesis

$$B_N' \propto B_T$$

$$\text{i.e. } B_N' = \gamma B_T$$

The value of γ is now investigated by examining the relationship between B_N' and B_T using values obtained from table 5.2(a). Using the three coil magnet arrangement outlined in this thesis it is possible to vary the field profiles considerably. An indication of this ability can be obtained by comparing the percentage variation of the ratio of B_N'/B_T between work presented here and that of previous authors[3,7,8]. Work by Walke et al[7] allowed the ratio to be varied by $\pm 3\%$ from the mean value whilst the arrangement used here allowed the ratio to be varied by $\pm 9.5\%$ from the mean value. Although the ability to change the field profiles has been considerably improved γ can still be considered as approximately constant, hence EQ 5.6 would become

$$\sigma = k(\gamma B_T)^x (B_T)^y$$

$$\text{i.e. } \sigma = (k\gamma)^x (B_T)^{x+y}$$

if we again take logs. of the equation, it now becomes

$$\text{Log } \sigma = \text{Log}(k\gamma)^x + (x+y)\text{Log}(B_T) \quad \text{EQ 5.8}$$

$$y = c + mx$$

Substituting the experimental results into EQ 5.8 then it is possible to produce a plot of Log σ vs. Log B_T , see Fig 5.10. Examining EQ 5.8 it can be seen that it is of the form $y = c + mx$, hence the gradient of the line will be equal to $(x+y)$.

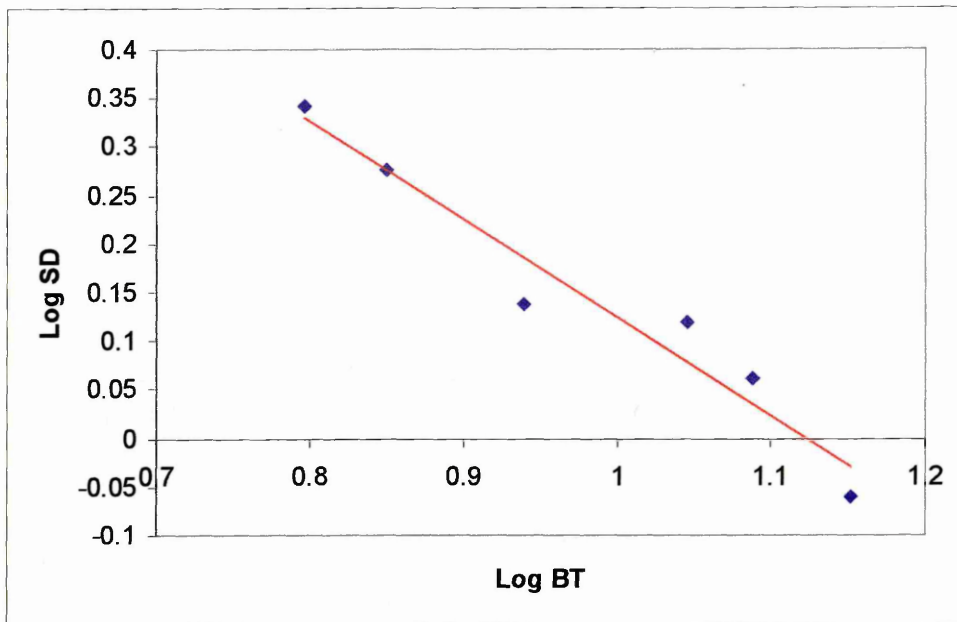


Fig 5.10, plot of Log σ vs. Log B_T , using reduced data set

To obtain a value for the gradient of the best fit line for the data shown in Fig 5.10, a fitting routine from MS Excel was used. This routine is called LINEST and provides a value for the gradient, m , and error in the gradient of the fitted line. When this program was applied to the experimental data then the results were 1.08 ± 0.08 , hence this means that $(x + y) = -1$ to within experimental error, as expected from Care prediction that $x = y = -0.5$.

Solving for the powers of B_N and B_T

Using the "Solver" routine supplied by MS Excel it is now possible to adjust the values of k , x and y in EQ 5.7 in order to minimise the value of χ^2 . The solver routine also allows the imposition of certain constraints. The results of the previous section imply that the constraint $(x + y = -1)$ is reasonable. The routine was then activated using a variety of starting/seed figures for k , x and y to find the values of the constants which closely matched the experimental results. Each run of the solver routine produced final fitted values for k , x and y which were noted along with the seed figures. After numerous start points were tried it was found that a large majority of the results settled around certain values for the constants. In order to illustrate the spread of the output values of k , x and y the following figures were compiled to show the breadth of these variations,

$k = 120 \pm 8$, $x = -0.47 \pm 0.04$ and $y = -0.54 \pm 0.04$

i.e.
$$\sigma \propto B_N^{-(0.47)} B_T^{-(0.54)}$$

Assessment of errors associated with the values for x and y

In order to assess the validity of the results found above, an indication as to the error values associated with these figures needed to be arrived at. Again a statistical method outlined in the book on error analysis by P R Bevington[11] was used, a précis of this method follows.

This technique uses three points which straddle the χ^2 minimum and assumes that the curve which passes through them will be treated as a parabola, an illustration of this can be seen below as Fig 5.11. In this plot the value of χ^2 is plotted against the range of values from a_0 to a_n .

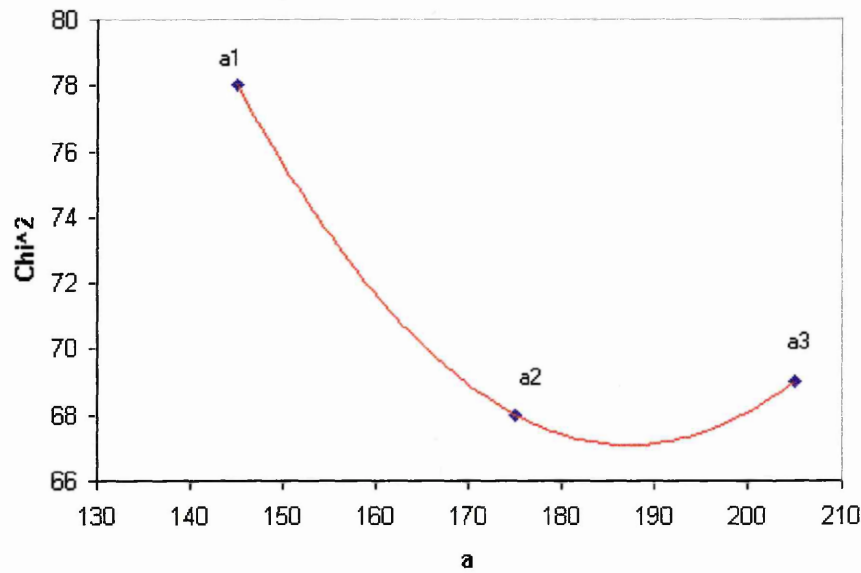


Fig 5.11, Plot of χ^2 vs. a

Thus we consider the three points as having the values

$$\chi^2_{(1)} = \chi^2_{(a1)}, \chi^2_{(2)} = \chi^2_{(a2)}, \chi^2_{(3)} = \chi^2_{(a3)} \quad \text{where } a1 = a2 - \Delta a \text{ and } a3 = a2 + \Delta a.$$

Hence the minima of the curve can be expressed as in EQ 5.9 below,

$$a(\min) = a3 - \Delta a \left(\frac{\chi^2_{(3)} - \chi^2_{(2)}}{\chi^2_{(1)} - 2\chi^2_{(2)} + \chi^2_{(3)}} + \frac{1}{2} \right) \quad \text{EQ 5.9}$$

The error in a can then be calculated by using the second derivative of χ^2 at the

minimum of the curve, $\frac{\partial^2 \chi^2}{\partial a^2}$. The error obeys:-

$$Error = \sqrt{2 \left(\frac{\partial^2 \chi^2}{\partial a^2} \right)^{-1}}$$

EQ 5.10

In order to utilise this method it is necessary to plot both x and y against χ^2 , see Fig 5.12(a) and (b).

By following the route outlined above it is then possible to calculate values for both x and y at the minimum of the χ^2 plots, as well as an estimation of their possible errors. These values then allow us to produce a complete expression for σ , EQ 5.11.

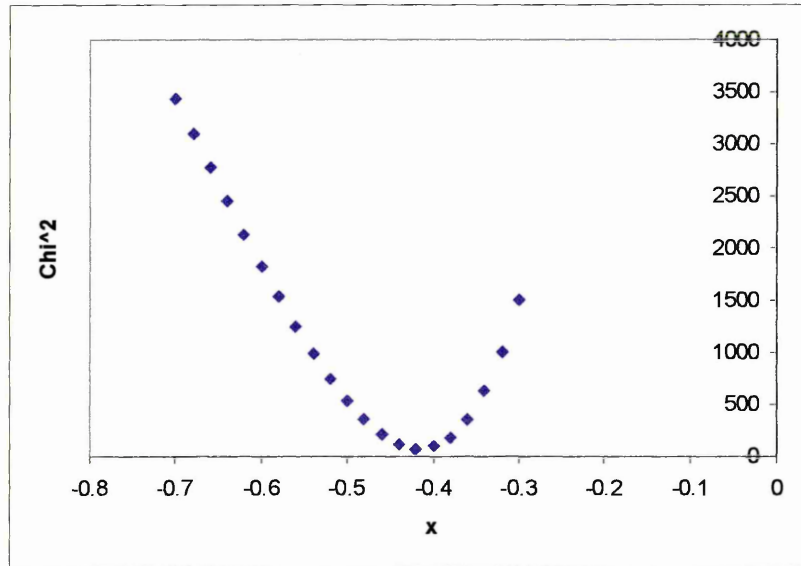
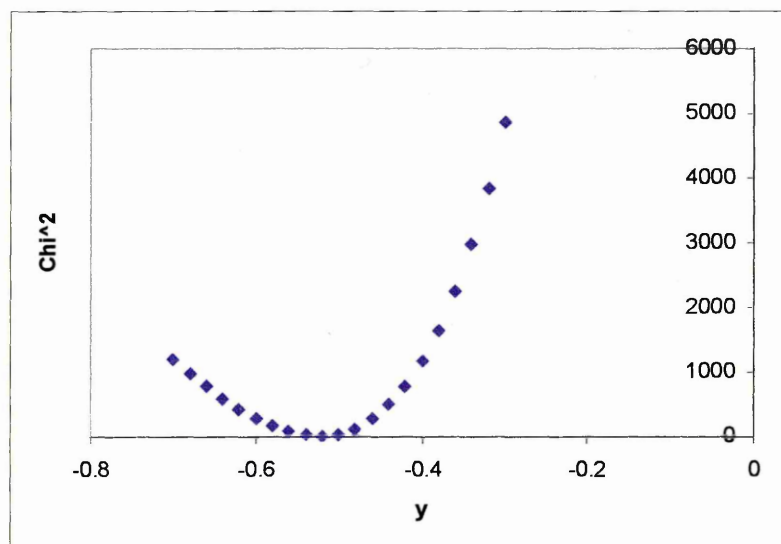


Fig 5.12(a), Plot of χ^2 vs. x

Fig 5.12(b), Plot of χ^2 vs. y



When such an error calculation was performed then errors for $x = \pm 0.001$, and $y = \pm 0.001$ are achieved. As can be seen these errors are extremely small indeed, numerous checks were performed on these error figures but the outcome was always the same. Thus in order to produce error estimates which appeared more credible another method of analysis was used. This method involved omitting one field setting at a time and then using the Solver routine in MS Excel to produce values for x and y . The spread of these various outcomes would then be used to give an error value for x and y . The results of this analysis is shown below in table 5.1

χ^2 value based on	x	y
All settings	-0.44	-0.56
All bar 1 st setting	-0.47	-0.53
All bar 2 nd setting	-0.45	-0.55
All bar 3 rd setting	-0.43	-0.57
All bar 4 th setting	-0.42	-0.58
All bar 5 th setting	-0.44	-0.56
All bar 6 th setting	-0.51	-0.49
Average Values	$-0.465 \pm 0.045/\sqrt{6}$	$-0.535 \pm 0.045/\sqrt{6}$

Table 5.1, Error values of x and y

Thus using this average as our error figure gives us the expression below,

$$\sigma \propto B_N^{-(0.47 \pm 0.02)} B_T^{-(0.54 \pm 0.02)} \quad \text{EQ 5.11}$$

If this result is now plotted, using LINEST it is possible to obtain a value for the intercept point, q , \pm error. Such a plot can be seen below, Fig 5.13, where $q = 0.14 \pm 0.13$. The stochastic model[1] predicts a relationship of $\sigma \propto (B_N B_T)^{-0.5}$, with $q=0$. The results presented here are very close to agreeing with this theory to within experimental error.

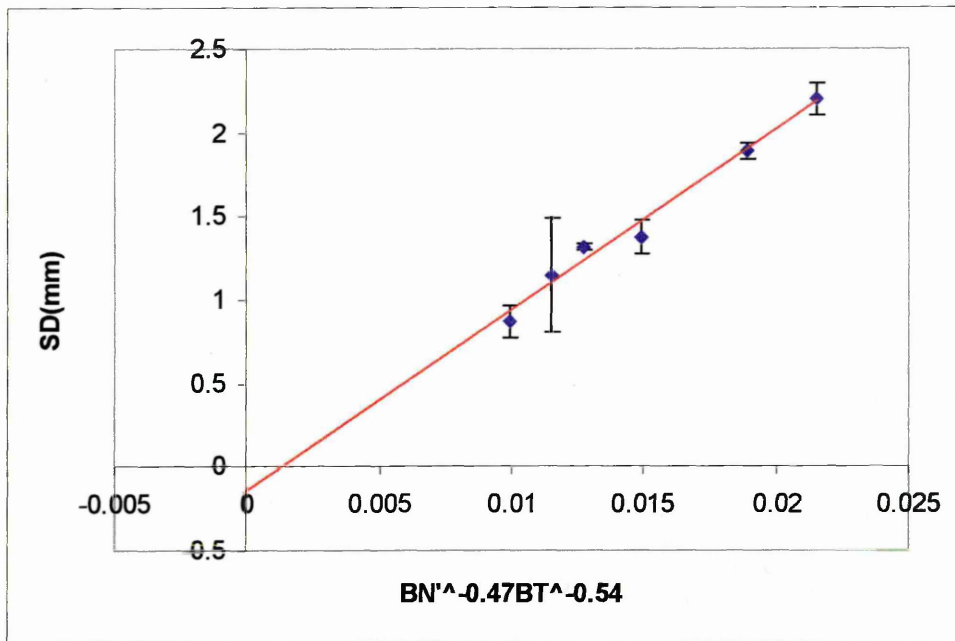


Fig 5.13, plot of σ vs. $B_N^{-(0.47)} B_T^{-(0.54)}$, using reduced data set

Comparison between data sets

Three sets of results are shown in Fig5.14, these are:

- (a) Results obtained by Walke et al[3] using a two coil electromagnetic steering array with values corrected for a flat cathode.
- (b) Preliminary results obtained using the three coil steering array using a severely eroded cathode, presented at ICMTFT 1996[12].
- (c) Results obtained using the three coil array and a flat cathode(the results were corrected for cathode wear).

The three sets of data are plotted on the same axes to allow the comparison of results presented here to work by others. To aid such a comparison a linear fit has been applied to (a) and (c).

In addition to this the inclusion of (b) allows the influence of the erosion of a track in the surface of the cathode to be clearly seen. 5.3.3.1 presents a discussion the effect of the trench on the movement of the arc, indicating the possible physical processes at work and suggesting possible lines of future work.

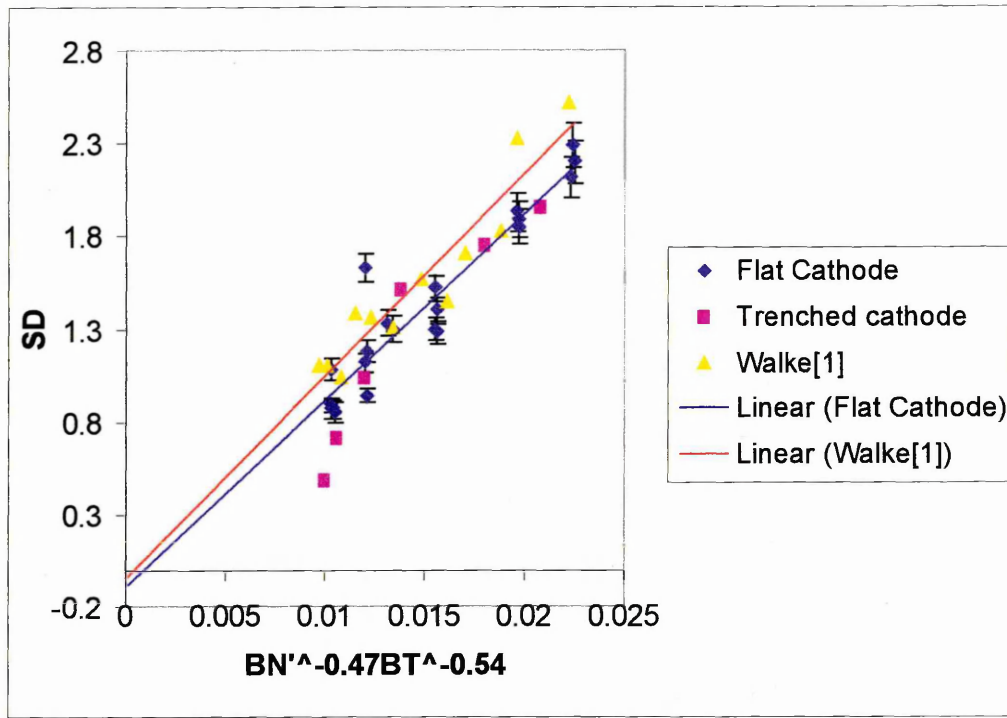


Fig 5.14, Plot of σ vs. $B_N'^{-(0.47)} B_T^{-(0.54)}$, using the full data set as in table 5.2(a)

Using the novel three coil electromagnetic steering array, as explained in chapter 4, allows greater freedom in the setting of B_T and B_N' values than the two coil steering array used for earlier work[3]. Though it is true that such a three coil steering array allows the proportionality between B_T and B_N' to be broken the system used here is not an ideal one because of the practical limitations discussed in section 4.2.1, such an array would hopefully be the basis of further research(see chapter 7). Although the system used is not an ideal one it has been shown that a greater degree of variation in the ratio of field components can be achieved, $\pm 9.5\%$ compared to $\pm 3\%$ for the 2 coil steering system. This steering array has allowed more in depth evaluation of the values of x and y . In addition to this the results presented here are also in a different regime of B_N'/B_T , with the values presented here being approximately half the B_N'/B_T values of Walke[3]. Such a difference in this ratio was achieved due to having 3 separate coils, as opposed to two.

5.3.3.1 The effect of erosion of the cathode on the magnitude of the applied magnetic field

As has been indicated above, a trench worn into the surface of the cathode can lead to significant changes in the behaviour of the cathode spot. In earlier work[3], Walke measured and modelled the magnetic field components to allow the estimation of magnetic fields in the region of a trench which had been eroded. This earlier work produced measurable increases in B_N' and B_T with trench depth, as indicated by Fig 5.15(a) and (b). In these experiments each run consisted of 2000 orbits, which after 25 runs produced an overall erosion of $650\mu\text{m}$. The information gained from these experiments was then used as a basis for the correction of magnetic fields components shown in this thesis.

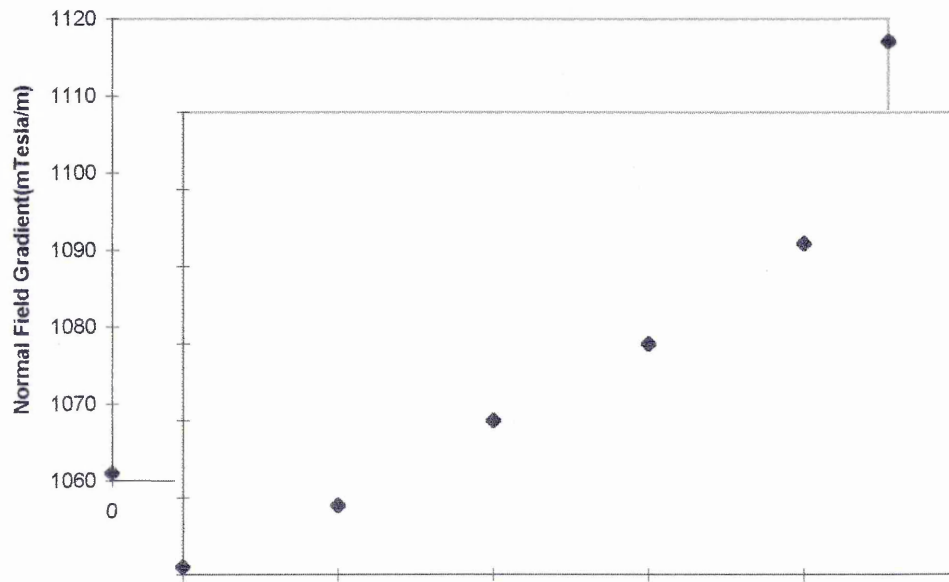


Fig 5.15(a), B_N' vs. Run Number after[3]

In further experiments Walke[3] found that with a track eroded to 2.5mm depth the B_N' at zero B_N had increased by 25%, whilst the B_T value had increased by 22%. These changes in magnitude of the magnetic field components led to an overall increase in confinement in the order of 19%.

An alternative explanation of the effect[5] of the trench can be achieved by examining the effect of the topology of the trench on the field values. Such an explanation is outlined in Fig 5.16.

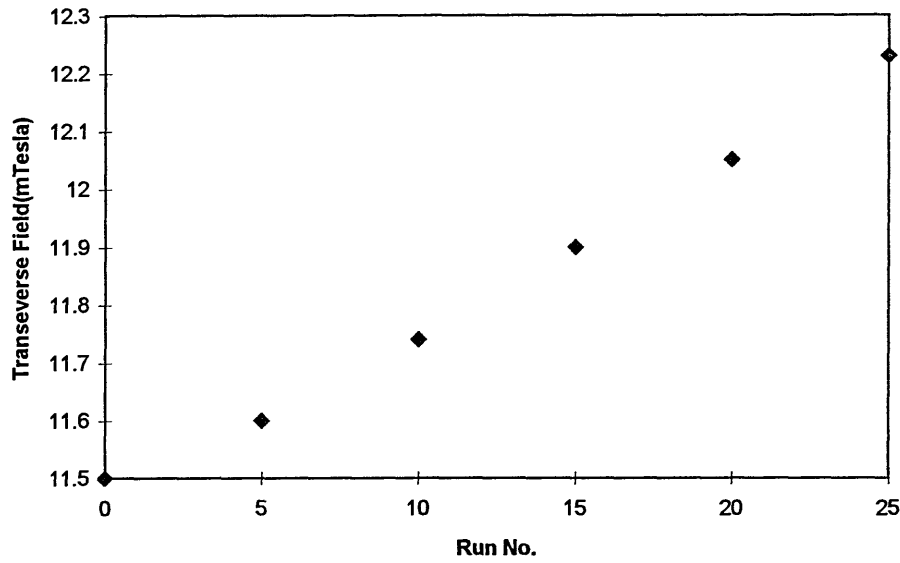


Fig 5.15(b), B_T vs. Run Number after [3]

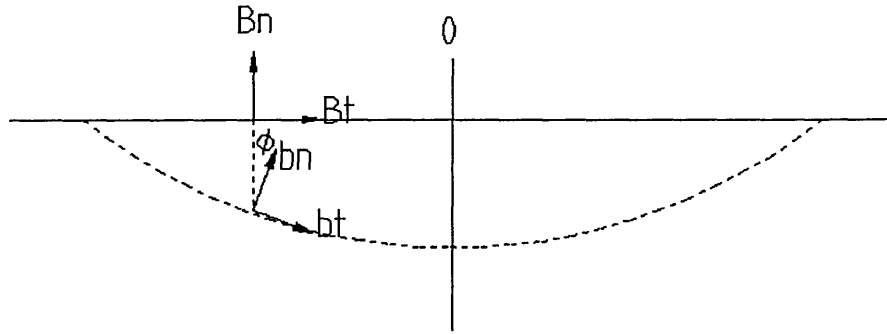


Fig 5.16, Diagram of the cathode, a trench and associated magnetic field components

The above diagram represents the effect of the erosion of a trench on the magnetic field. From this we can see that when $\varphi=0^\circ$ then $B_N = b_N$ and $B_T = b_T$, and when $\varphi=90^\circ$ then $B_N = b_T$ and $B_T = b_N$. It is possible to relate b_N and B_T to B_N for any value of φ , thus

$$b_N = B_N \cos \varphi + B_T \sin \varphi \equiv B_T \left(\frac{B_N}{B_T} \cos \varphi + \sin \varphi \right) \quad \text{EQ 5.12}$$

$$b_T = B_N \sin \varphi + B_T \cos \varphi \quad \text{EQ 5.13}$$

by differentiating EQ 5.12 it is possible to obtain an expression for the normal field gradient experienced by the spot in the trench(b_N'), which after algebraic manipulation, recognising that $\varphi = \frac{dy}{dx}$, gives the following expression

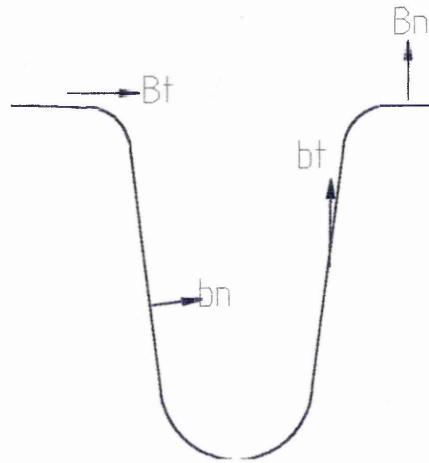
$$b_N' = B_N' \cos \varphi + B_T' \sin \varphi + \frac{d^2 y}{dx^2} (B_T \cos \varphi - B_N \sin \varphi) \quad \text{EQ 5.14}$$

(where x and y are distances from the origin in the horizontal and vertical plane respectively)

Thus at small φ

$$b_N' = B_N' + \frac{d^2 y}{dx^2} B_T$$

But for a deep narrow trench φ is not small and $\frac{d^2 y}{dx^2}$ will be large, as illustrated in the sketch below.



The resultant profile of B_N takes the form shown in 5.16

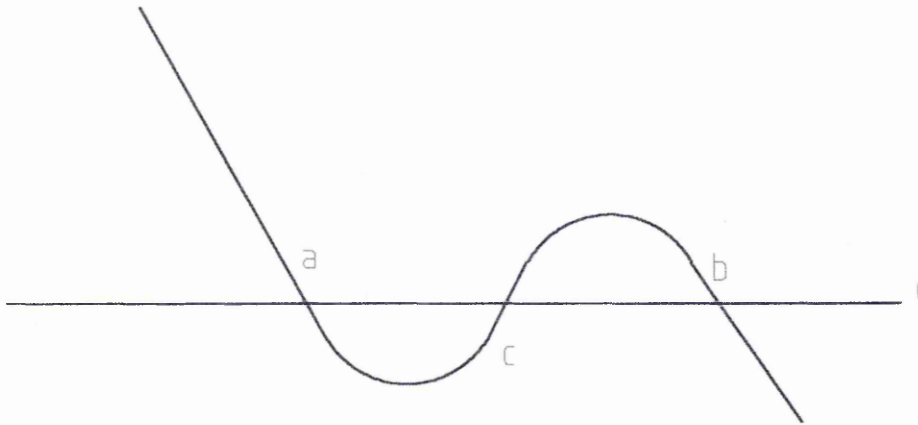


Fig 5.17, Plot of B_N vs. x.

Thus the spot would be repelled by point c with a and b being equilibrium, meaning that an experimental observer would notice an increase in the depth of the well but not a widening of the trench. Examining the preliminary work presented at ICMTFT

1996[12], and plotted as Fig 5.14, it can be seen that there is a deviation from the expected line of results. It is thought that the complicating effects of the trench on the arc motion could be the reason for this, chapter 7 includes suggestions for further work which should be able to clarify the effect of the trench.

5.4 Measurement Of The Distribution Of Orbital Transit Times

5.4.1 INTRODUCTION

The stochastic model predicts that the motion of the arc in the orbital direction will be a movement at a uniform velocity, c , upon which a random diffusive motion is superimposed[1]. By assuming one dimensional motion and that at $t=0$ the arc is at $y=0$ then

$$\phi(y,t) = \frac{1}{\sqrt{(4\pi\alpha_x t)}} \exp\left(\frac{-(y - vt)^2}{4\alpha_x t}\right) \quad \text{EQ 5.15}$$

The above equation uses, α_x instead of D_x for the diffusion constant, v for velocity instead of c . Such alterations to the nomenclature used by Care[1] were made to be consistent with later notation and to avoid confusion arising the diffusion constant and the fitting parameter. The experimental work described in this section was obtained by monitoring the arc as it passes a fixed point, the photodiode array, thus enabling a distribution of spot transit times to be produced. From this analysis it is possible to extract values for the arc speed and diffusion constant[3,7].

5.4.2 EXPERIMENTAL DETAILS

Using the equipment as described in 5.3.2, along with the program outlined in 5.1, a number of experiments were performed which produced distributions of transit times of the arc for a variety of field settings. As has been mentioned earlier in this chapter this experimental data was obtained using the new detection system, which allowed simultaneous monitoring of both radial position of the arc and orbital transit times.

For the duration of the experiments conditions were kept as stable as possible. All measurements were made at a fixed backing pressure of 40 mtorr of Argon and using an arc current of 80A.

Using the methods outlined in 5.3.2 experimental runs were performed on the cathode, each of the runs consisted of measuring 500 orbits of the arc. Previous arc analysis

work[3] allowed the monitoring of 2000 orbits but due to changes in the design of the anode, and the detection mechanism, it was impossible to monitor such a large number of orbits. To maximise the number of number of revolutions measured a shielding system was designed, built and employed as shown in fig 4.4. Such a shielding system enabled the viewing port to be obstructed during the random arc cleaning of the surface of the cathode. Such cleaning of the cathode was necessary each time the arc was run after the chamber had been brought back to atmosphere because the cathode surface absorbs impurities present in the air thus producing a contaminated surface and hence type 1 cathode spots.

5.4.3 DISTRIBUTIONS OF SPOT TRANSIT TIMES

As mentioned previously each experimental run produced 500 values for the spot transit time. These values were obtained using the program `arctme.bas`, a modified version of a program written by Walke[3]. The output of `arctme.bas` program consisted of values, in microseconds, which represented the time interval between consecutive passes of the arc. Such data was stored as a succession of numbers which were comma separated. Another program, `datanal.bas`, then took this raw experimental data and analysed them. The program works as follows(a full listing can be found in appendix B):

- Data are imported and stored in an array
- The data undergoes a 2 stage filter process. First the data is analysed and any data above $\pm(3 \times \text{Standard deviation})$ from the mean are removed. Secondly the data must then pass through a band pass filter, such a filter serves to remove experimental values which indicated that either the arc had not completed an entire orbit or alternatively that the circuitry had failed to register a second pulse. This second stage filter is made largely redundant by the new more complex data filter. Such filtering of the data leads to approximately 5-10% of the data being rejected. Such erroneous readings could be due to the extremely electrically noisy environment which the detector circuitry is working in.
- The data are sorted into 17 bins to enable the frequency distribution to be produced, for eventual comparison with the theoretical distribution as outlined by Care[1]. The histogram information is then saved to a file to permit the “fitting” of various parameters by another program, `ksfitter.bas`.

- Using the above frequency distribution values a normal distribution with the same mean and standard deviation as the measured data is generated. Again this distribution was then saved to file for comparison with the theoretical distribution.

5.4.4 FITTING OF THE DATA TO THE THEORETICAL DISTRIBUTION

As has been described above the datanal.bas program produces several values and distributions which will be used by ksfitter.bas to produce fitting coefficients. Such a fitting is achieved by altering the values of velocity of the arc, v , and diffusion constant, α , until the best match between the theoretical distribution and the actual distribution is achieved. For the purpose of this calculation it is assumed that the distance which the arc travels during one orbit remains constant.

The program KSFITTER is based upon a Kologmorov-Smirnov fitting routine and is written in QuickBasic(for full listing see appendix B). The program uses a grid search method to successively approximate the values for v and α . Initial guesses are made by the user, based on previous experience, and a step size is calculated(1/10th of the value initially). The program then steps through the values of v and α changing their values until a local minimum is located. This point, along with the two bracketing it, are then used to determine the minimum of a parabola passing through these three points. Once the minimum has been roughly located the step size is then decreased, based upon the number of steps required to reach the minimum, and the exact position of the minimum is located. This process is repeated until the change in the goodness of fit parameter with each combination of v and α values is below $\approx 1\%$.

The goodness of fit for this program was changed from the χ^2 test for the comparison of measured frequency distributions to the Kologmorov-Smirnov(K-S) test. The K-S test is for the comparison of measured and continuous distributions[3,6]. The difference between the two tests is shown below.

The formula for the χ^2 test is

$$\chi^2 = \sum \frac{(O - E)^2}{E} \quad \text{where } E \text{ is expected value and } O \text{ is the observed value}$$

The K-S test calculates the maximum deviation, D , between the normalised cumulative distribution of the continuous function and the measured distribution,

$$D = \max_{i=1}^{i=n} |F_i - S_i|$$

where F_i is the theoretical cumulative distribution and

S_i is the measured distribution.

The advantage of K-S fit is that it produces an even fit across the graph as opposed to the χ^2 fit which tends to emphasise the wing area of the distribution (i.e. when E is small)

Once the minimised value for D has been produced this can then be compared with a tabulated, or calculated, value for the confidence interval,

$$1\% \text{ confidence} \quad D_{\text{crit } 1\%} = 1.63/\sqrt{n} \quad \text{where } n = \text{number of samples}$$

In order that the hypothesis that the experimental data is not from the theoretical distribution can be rejected, then the D value returned by the K-S test must be below the critical value calculated from the above.

A D value for the fit between the experimental and normal distribution, with the same mean and standard deviation as the experiment, is also calculated in order that a comparison of the goodness of fit can be attained.

5.4.5 RESULTS

The fitting process described previously was performed upon all of the data sets obtained from the experimental runs allowing the determination of the fitted values for v and α . The term $V(\text{raw})$ is used to denote experimentally obtained values for velocity of the arc, which were derived directly from the arc timing software.

The experiments were performed after the cathode had been thoroughly random arced to remove any oxide layer or surface contamination.

Table 5.3 summarises the experimental data collected. Included in the information are the B_N , B_T values, goodness of fit parameter (as explained earlier) and the v and α values obtained from the fitting routine.

From the table it can be seen that in all cases the magnitude of the goodness of fit parameter between model and experiment (D_{model}) was better than that between the

experiment and the normal distribution(D_{normal}). In addition to this D_{model} was always below the 1% confidence value of D_{critical} for a sample of 500 orbits. Thus the hypothesis that the experimental data is from a distribution other than that predicted by the stochastic model is rejected.

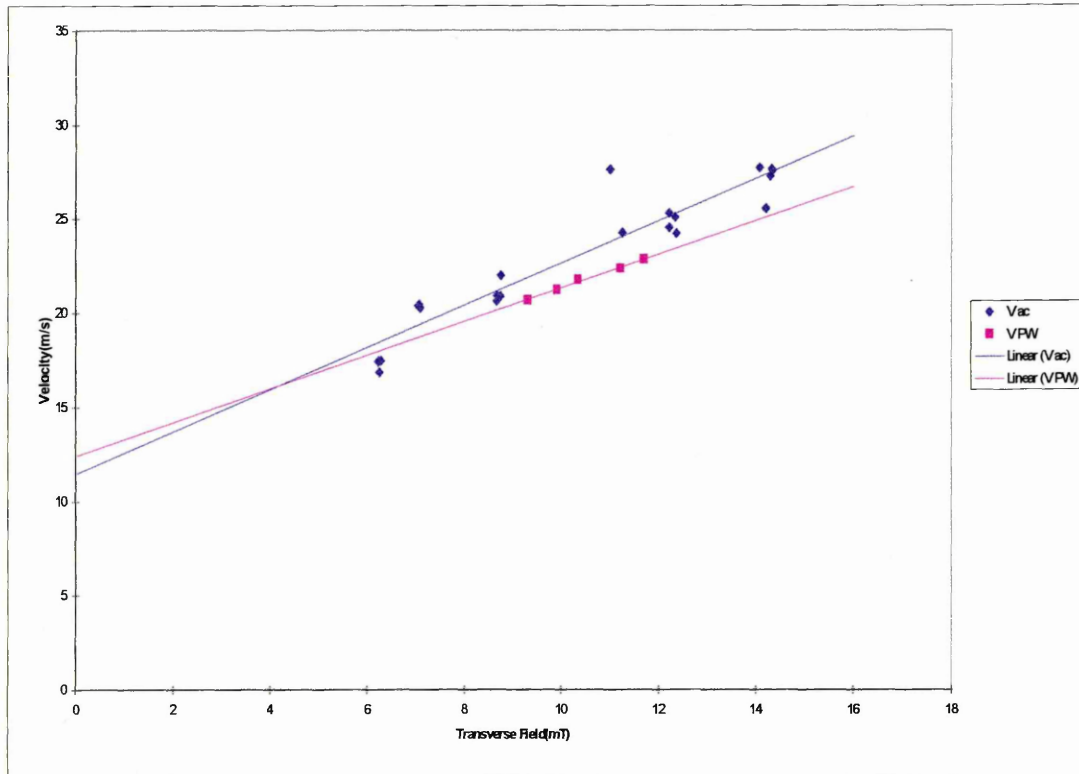
Table 5.3 Summary of experimental results pertaining to the movement of the arc

B_T mT	B_N' mTm ⁻¹	V(raw) ms ⁻¹	V(fit) ms ⁻¹	α (xe-2) m ² s ⁻¹	D_{model} (xe-2) ($D_{\text{crit}}=7.29\text{e-}2$)	D_{normal} ($D_{\text{crit}}=7.29\text{e-}2$)
14.32	878.82	27.56	27.80	1.09	2.17	0.51
14.31	878.61	27.67	27.80	0.85	2.54	0.55
14.28	876.50	27.27	27.13	1.05	3.02	0.44
14.19	870.74	25.56	27.46	1.15	3.01	0.29
14.06	864.95	27.72	27.94	1.28	2.13	0.49
12.35	755.77	24.24	24.89	1.95	6.46	0.40
12.32	755.37	25.11	25.39	1.06	4.33	0.49
12.20	748.17	25.30	25.57	1.09	3.52	0.49
12.20	748.82	24.54	24.80	1.43	4.06	0.46
10.98	674.79	27.61	27.54	1.98	3.66	0.35
8.74	642.71	22.00	22.07	2.99	2.45	0.32
8.73	640.28	20.88	21.03	3.20	1.09	0.34
8.66	638.31	20.94	21.03	3.20	1.09	0.30
8.66	639.67	20.64	20.65	2.57	1.65	0.81
7.08	493.98	20.28	20.58	2.76	1.65	0.31
7.06	493.34	20.45	20.71	2.93	1.43	0.29
7.04	491.83	20.36	20.68	2.61	2.27	0.31
6.27	431.18	17.46	18.01	4.15	2.55	0.28
6.24	429.36	16.86	17.43	4.86	3.43	0.26
6.22	428.07	17.42	17.91	4.34	2.42	0.26

5.4.5.2 The spot velocity

Table 5.3 gives the spot velocity for a variety of magnetic field settings. As has been mentioned earlier, experimental runs are recorded after a lengthy period of “random arcing” of the surface of the cathode. Figure 5.19 shows these results for spot velocity plotted against B_T .

Fig 5.18, Velocity of the arc vs. Transverse field, using data set from table 5.3



In the above figure two sets of values are depicted, experimental results obtained for this thesis (V AC), experimental results of a previous author (V PW) adjusted as shown below [3,7]. Best fit lines to these data sets are also shown and finally linear fit to these data sets. The adjustment of the values of Walke was necessary due to differences in operating conditions,

- (i) Higher backing gas pressure
- (ii) Higher arc current

In order that correction factors for the two parameters could be arrived at the literature was consulted [9,10]. Swift et al had performed a number of experiments which illustrated the variations in velocity for a range of pressures and also arc currents.

Examination of the plots of Swift et al, as illustrated in fig 5.19a and 5.19b, then allowed the variation in the spot velocity to be quantified. The correction factor for the spot velocity, due to the difference in arc current and pressure settings, was found to be 2.35m/s. The results of Walke in Fig 5.18 have thus been adjusted to account for this difference. Examining the plot it can be seen that there is a similarity in the results, though they do still differ. It is thought that such a difference could arise due to the method by which adjustments were obtained, i.e. reading figures from trends of graphs, which itself entails some uncertainty.. According to work by Swift et al[9] a plot of B_T vs. Spot velocity should produce a graph whose gradient is 1m/s/mTesla. If a linear fitting routine is applied to our data then the gradient of the line produced is $1.1 \pm 0.1\text{m/s/mTesla}$, showing good agreement with Swift.

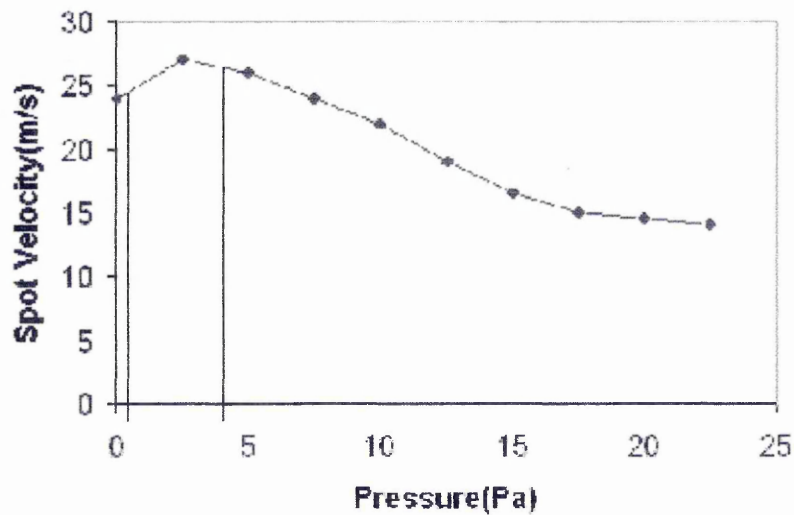


Fig 5.19a, Plot of Spot velocity vs. pressure after[9]

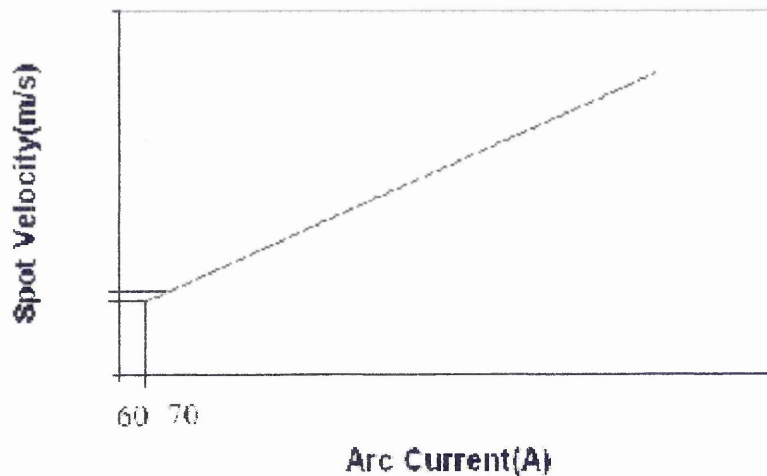


Fig 5.19b, Plot of spot velocity vs. arc current after[9]

5.4.5.3 Effect of Applied Magnetic Field on the Diffusion Constant

According to the stochastic model[1] the value of the diffusion constant in the direction of retrograde motion, α , should have no dependence upon B_T or B_N . This section briefly describes the experiments performed to test for any such dependence.

As described previously, 5.4.4, a fitting routine was utilised to produce values for both velocity and diffusion constant, with the results being presented as table 5.3. These values for α are shown plotted against B_T in figure 5.20.

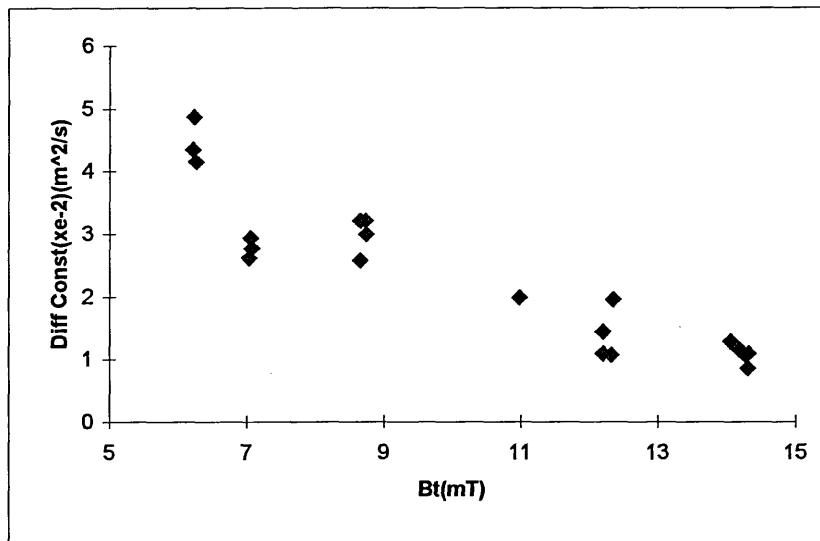


Fig 5.20, Diffusion constant(α) vs. Transverse field(B_T), using data set from table 5.3

The results presented above extend the experimental range of B_T settings for which the α values were determined, approximately $B_T = 6.5$ -14 mT for this work as compared to $B_T = 11.6$ -12.3 mT range of earlier studies[3,7]. Similar trends are observed in the behaviour of the diffusion constant, when compared to earlier work[7]. However there is approximately an order of magnitude discrepancy in the values obtained. To check this discrepancy an alternative method of obtaining a value for α was used. This method involved the graphical analysis of the orbital period distributions. As part of the data gathering process, the distribution of orbital transit times was calculated and saved. Here the time taken to complete a single orbit is logged in one of 17 frequency bins and the outcome saved. Examples of such distributions can be seen over as Fig 5.21(a) and (b).

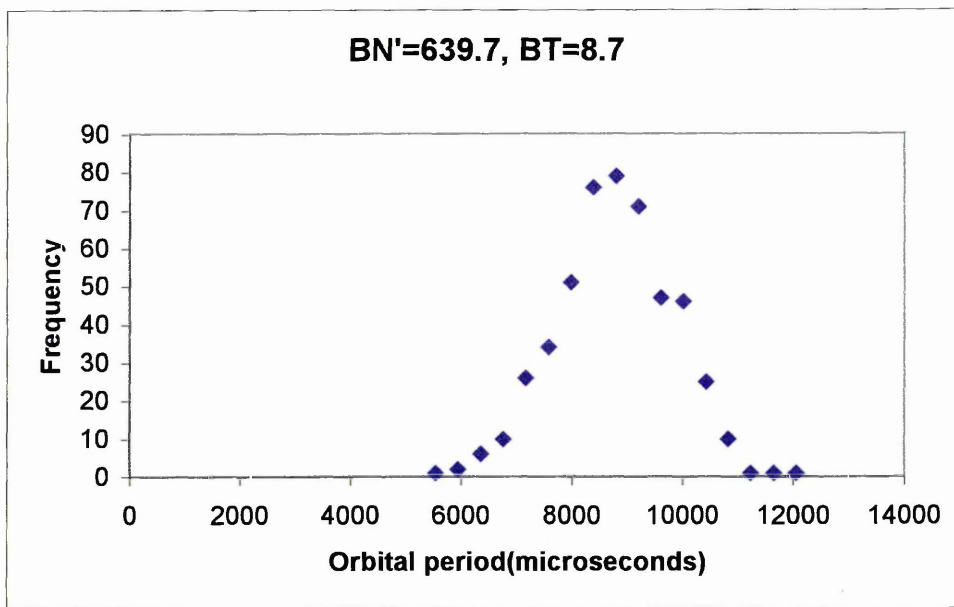
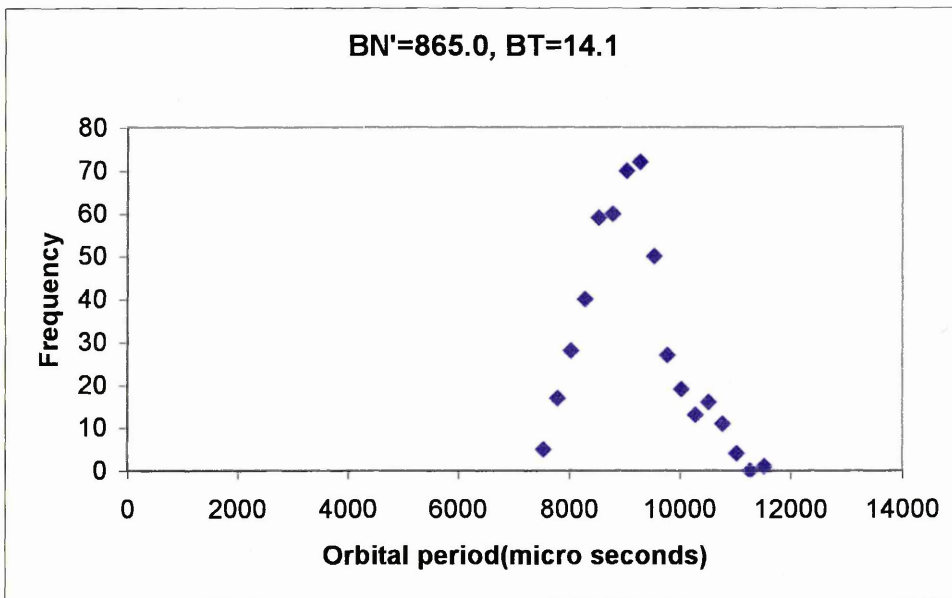


Fig 5.21 (a), Plot of orbital period vs. normalised frequency
 (b), Plot of orbital period vs. normalised frequency



To obtain a value for α from this distribution of transit times the following analysis can be carried out.

The standard form of a Gaussian distribution can be described as

$$= \frac{(x - \bar{x})^2}{2w^2}$$

It can be seen that the denominator of the gaussian equation is equal to the denominator of the exponential expression from the stochastic model EQ 5.15,

i.e. $2w^2 = 4\alpha t$

thus $w = \sqrt{2\alpha t}$ EQ 5.16

where w is the half width(in distance units), α is the diffusion constant and t is the mean orbital period.

In graphical terms the value of w can be expressed as

$$w = \text{Vel} * \Delta t = x\Delta t / t$$
 EQ 5.17

where x is the orbital circumference, Δt is the half width of the frequency distribution and t is the mean orbital period.

Hence combining EQ 5.16 and EQ 5.17 produces an expression for α ,

$$\alpha = \frac{x^2 \Delta t^2}{2t^3}$$
 EQ 5.18

Therefore it is possible, using EQ 5.18, to calculate a value for α from a given frequency distribution.

To assess this method it was then applied to validate results of previous authors[3,7]. Applying this methodology it was then possible to obtain values which were in good agreement with the results reported, see example below, thus proving the validity of the process.

Using values obtained from a graph presented by Walke[7]

$$x = 0.1194, \Delta t = 0.97\text{ms}, t = 12\text{ms}$$

Therefore $\alpha = 3.88 \times 10^{-3} \text{ m}^2\text{s}^{-1}$

The value of α reported in the paper was $2.77 \times 10^{-3} \text{ m}^2\text{s}^{-1}$. Considering that values were obtained “by eye” from a graph the two values agree well.

Using this technique the values of α can now be determined graphically, see below,

Fig 5.21(a)

$$x = 0.1382, \Delta t = 1145\mu\text{s}, t = 8800\mu\text{s}, \text{ leading to}$$

Therefore $\alpha = 1.84 \times 10^{-2} \text{ m}^2\text{s}^{-1}$, which compares with the precise program result of $2.57 \times 10^{-2} \text{ m}^2\text{s}^{-1}$

Fig 5.21(b)

$x = 0.1382$, $\Delta t = 714\mu\text{s}$, $t = 9260\mu\text{s}$, leading to

Therefore $\alpha = 6.23 \times 10^{-3} \text{ m}^2\text{s}^{-1}$, which compares with the precise program result of $1.28 \times 10^{-2} \text{ m}^2\text{s}^{-1}$

Examining the two examples above the results obtained using the fitting program agree with the graphically obtained results, to within the approximations of the latter method, hence this confirms that there is a difference between the results presented here and the work of others[3,7]. This discrepancy now needs to be investigated.

As has been mentioned earlier in chapter 4, there were some operational differences between the system used here and that used by Walke
i.e. $I=80\text{A}$ ($I_{\text{walke}}=70\text{A}$) and Pressure= 40mTorr Argon ($P_{\text{walke}}=4\text{mTorr}$).

It may be that the pressure difference may be at the root of the difference. Anders et al[13] described the effect of increasing pressure on the diffusion constant.

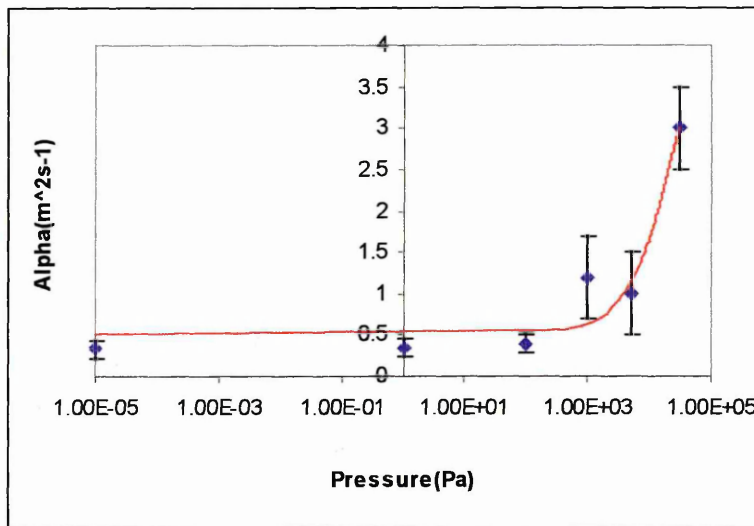


Fig 5.22, Plot of α vs. Pressure after [13]

From their plot, see Fig 5.22, it can be seen that at some threshold point any pressure increase has a dramatic effect on the diffusion constant. However there may be reasons why the work of Anders et al may not be directly comparable with the present work:-

1. The threshold point is not very well defined, having only a single point. Thus the threshold may indeed be closer to the range of pressure being used here.
2. The effect of arc current is not shown, or the operational current quoted

3. The plot is for the effect on a random arc, where as the results we present are for a steered arc.

Although there is indeed a distinct difference between the results presented here and those by other authors, it is thought a number of further areas of research may be able to clarify the position. Suggestions for further work are outlined in chapter 7. Due to the significant discrepancy some doubt is cast on the “combined data sets” approach to obtaining the powers of B_N' and B_T , hence method 1 5.3.3 should be regarded with caution.

REFERENCES

- [1] C M Care
Journal of Physics D: Applied Physics 25(1992)1841
- [2] M Abramowitz, I A Stegun
Handbook of Mathematical functions
Dover: New York (1965)
- [3] P J Walke
PhD Thesis, Sheffield Hallam University, September 1994
- [4] RS Components Data Sheet No. F14784
- [5] Private Communications R New 1997
- [6] J B Kennedy, A Neville
Basic Statistical Methods for Engineers/Scientists (3rd edition)
Harper and Row: New York (1986)
- [7] P J Walke, R New, C M Care
Surface and Coatings Technology 68/69(1994)352
- [8] P J Walke, R New, C M Care
Surface & Coatings Technology 59(1993)126
- [9] P D Swift, D R McKenzie, L S Falconer, P J Martin
Journal of Applied Physics 66(2)(1989)505
- [10] D Y Fang
Journal of Physics D: Applied Physics 15(1982)833

- [11] P R Bevington, D K Robinson
Data Reduction and Error Analysis for the Physical Sciences
2nd edition. Published by McGraw – Hill Pages, Chapter 8

- [12] A L Craven, R New, C M Care, P J Walke, J Cawley
Poster presented to ICMCTF '1996 San Diego

- [13] S Anders, B Jüttner
IEEE Transactions on Plasma Science 19(5)(1991) 705

6.0 EXPERIMENTAL STUDIES OF MACROPARTICLE DISTRIBUTION

Many authors have examined macroparticles(see chapter 3) and their effect upon the hard coatings produced by cathodic arc PVD. In this chapter new results are presented which illustrate the effect of velocity and confinement of the steered arc on the angular distribution of macroparticles.

The chapter is divided into four sections:

- Methods of investigation
- Sample preparation
- Analysis methods
- Experimental results

6.1 Method of Investigation

As has been mentioned previously, a novel three coil electromagnetic steering array has been designed and built(see chapter 4). This new array allows the variation of the transverse and normal elements of the magnetic field to be varied, so that the effect on various parameters can be observed. In this chapter we are interested in studying the effect of the magnetic field on the angular distribution of the macroparticles. To this end some form of sample holder was required. Before such a design was produced the operating criteria and requirements had to be determined, initially there were only two criteria the holder must fit:

- It must be able to provide a wide range of angles from the source
- It must be possible to apply a bias to the substrates to increase adhesion of the coating.

A system was designed which fitted these requirements(see 4.2.4) as it can be seen that there are two parts to the final design.

a. Substrate holding plate

This plate is of the same dimensions as the others used around the chamber, enabling interchangeability between the ports. The main feature here is the water reservoir situated behind the front face of the plate, meaning that if a single sample was being coated it would be possible to keep it cool. The second feature is the PTFE spacer, which along with the nylon bolts used to fix the plate to the chamber, isolates the plate (and therefore samples) from the chamber meaning a bias can be applied.

b. A sample holder

This is constructed from two sections from a circle of steel. The reason for its shape was to make the face of each sample equidistant from its nearest section of the arc orbit. The distance between cathode and substrate is critical since the macroparticles are ejected with a certain energy, hence as the distance from the emission site to sample increases then the number of macroparticles reaching the sample will decrease. In addition the equidistance of the samples means that the solid angle subtended by the substrate remains constant. In addition to this another problem was identified, this being the distance

between source and sample. Over such a short distance it was impossible to treat the orbit of the arc as a point source, hence some method was required which would enable the samples to be shielded from macroparticles from a large portion of the arcs orbit. Achievement of this would enable the solid angle subtended by the samples to remain approximately constant. The solution to this problem was studied and after careful consideration a double shield system was developed with holes drilled to allow for a narrow passage through the shield for the flux from a narrow region of the arcs orbit, such an arrangement should provide the desired outcome. An approximate representation of this system is shown as Fig 6.1, with the holes mentioned above being at the position where the line between the cathode and substrate crosses the shields in front of the sample holder. Such shielding will therefore allow the section of the arc to be treated as a point source. Using this design it was possible to produce a working model which would allow the study of a range of emission angles, with the range under study being 0° , 9° , 25° , 44° , 63° , and 79° .

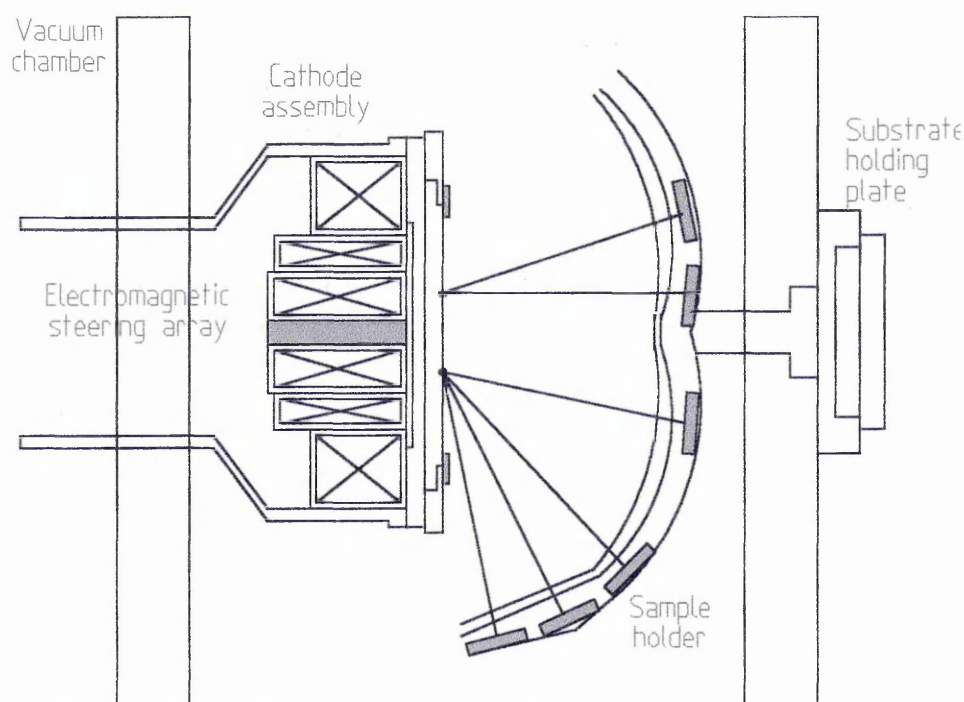


Fig 6.1, Diagram of the sample holder with the double shield mechanism

6.2 Sample preparation

In order to differentiate between the macroparticles and sample surface structure a highly polished finish was required. For these experiments circular stubs of stainless steel, 32 mm diameter by 7mm thick, were used and mounted onto the sample holder. These stubs were polished to a 1 μ m diamond finish. The polishing was performed at the facilities of the Materials Research Institute, and involved using successively finer grades of grit paper. For each grade of paper the stubs were eroded for between one and two minutes, until the scratches from the previous paper had disappeared. The orientation of the stub was altered by 90° each time a new grade of paper was used. After each grade disk, the stubs were washed in soap solution and then dowsed with acetone and then methanol to remove any debris or residues. When all grades of sanding disks had been used, and the samples cleaned, diamond paste was used to polish them further. Here the stubs were polished, using the finishing wheels, for up to five minutes. As before the samples were thoroughly cleaned between stages. Once a satisfactory level of polishing had been achieved the stubs were stored in a dessicator to keep them dry and dust free. Even so before the substrates were attached to the holder, prior to deposition, a cleaning cycle was used. This cycle was to completely clean and degrease the samples to increase adhesion of the TiN coating, this cleaning regime was arrived at after consulting colleagues, and consisted of the following stages:

- 5 minutes ultrasonic agitation in acetone bath
 - to remove grease
- 5 minutes ultrasonic agitation in methanol bath
 - to remove grease and acetone residue
- 3 minutes ultrasonic agitation in first Millipore, highly pure de ionised, water bath
- 2 minutes ultrasonic agitation in second Millipore water bath
- Drying using a nitrogen line

N.B. During and after the cleaning stage handling of the samples was kept to a minimum, and only performed using lint free cotton gloves, to avoid grease contamination.

Once the samples had been cleaned they were mounted on the substrate holder and the substrates were dusted again with a nitrogen line immediately prior to being sealed in the chamber for coating.

6.3 Analysis Method

Due to the size of the macroparticles under consideration it was impossible to analyse them using the naked eye, or an optical microscope. Hence to view these particles a scanning electron microscope(SEM) was used.

6.3.1 MODES OF OPERATION OF THE SEM

There are three modes in which an SEM can be operated, secondary electron, backscatter and a mixture of the two. Each of these modes has its advantages and disadvantages for the different imaging needs. The most common type used is secondary electron mode. Here a detector is placed at an acute angle to the surface of the sample, where it detects the secondary electrons emitted from the surface due to probing by the beam. The detector consists of a positively charged metal grid which accelerates the secondary electrons towards a photomultiplier tube, this mode of operation produces a topographical image of the surface, due to the nature of secondary electrons. The other mode used is backscatter mode, here as the electron beam hits the surface of the specimen energetic primary electrons are backscattered. To monitor these the backscatter detectors are normally positioned above the sample, around the final condenser lens in the microscope column. This method is therefore elementally sensitive, since each substance has a different back scattering efficiency. Where a greater contrast is required the two above modes can be combined, to produce a clearer picture of the surface. An example of such an occurrence is where a macroparticle is deposited on a surface of different composition, using a mixed mode it is possible to "highlight" the droplets making the identification process much simpler.

The equipment used for the results presented here was a Philips XL40 series analytical scanning electron microscope(ASEM), comprised of a Link eXL energy dispersive x-ray(EDX) and back scatter facility. In the analysis presented here a combination of the two was used, 80% secondary electron mode and 20% backscatter, such an arrangement was chosen to create a greater degree of contrast between the surface and the macroparticles.

6.4 Analysis of Macroparticle Properties

Due to the size of the macroparticles the only way to analyse the droplets is by using an SEM. Using this equipment it was possible to analyse macroparticle density/size distribution and by comparing results from different samples angular information can be gleaned. The following is a brief description of how each of the two methods were performed:

6.4.1 ANGULAR DISTRIBUTION

Here the SEM was used to produce Polaroid prints of 20 fields of view, two examples are shown as Fig 6.2(a) and (b), each covering $1.4 \times 10^{-9} \text{ m}^2$ of the sample.

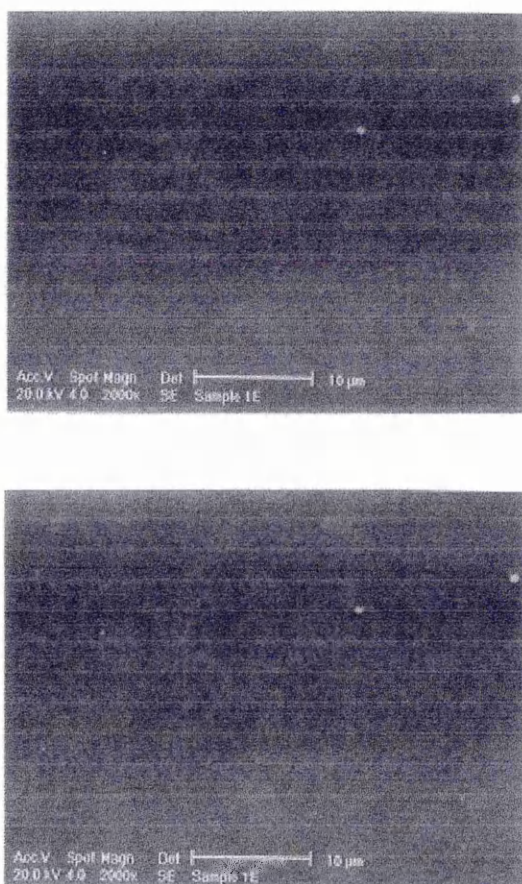


Fig 6.2(a) and (b) Sample images of typical photographs from SEM

The location at which the photographs were taken was chosen randomly in the area of the sample which had not been shielded from the macroparticle flux. A magnification of $\times 2000$ was used for the photographs, thus enabling a manual count of the macroparticles to be undertaken. An automated system of feature selection is available called Featurescan which can identify and measure particles. Unfortunately some problems

were encountered when using this system, a full explanation of this problem can be found in 6.4.2. Once the count had been performed for the required number of frames a value for count per unit area was calculated, ρ_m . It was estimated that using this method the smallest macroparticle counted was in the order of $0.2\mu\text{m}$. It should also be pointed out that the values for macroparticle density were determined by manually counting the number of macroparticles per frame, but blinding the run number and sample identification whilst the counting was being undertaken. Such blinding was achieved by the construction of a counting jig which covered the area of the frames which featured the identification markers. As an extra measure of quality assurance the values obtained from the counting were again checked blindly by randomly selecting frames taken and then recounting, this blind testing was performed on 10% of the frames and it was found that the results obtained were found to be within the variation of the counts.

6.4.2 SIZE DISTRIBUTION

As was mentioned above several problems were identified when using the automated counting software. These were due to the manner in which valid features are identified, this method is explained in the following.

The Featurescan software operates on a separate computer from that which controls the microscope, this computer “grabs” the image of the sample from the electron microscope computer and stores it to memory. Once the image has been acquired, objects are selected which match a range of user defined parameters. In this case the parameters were:

- Minimum number of pixels
- Maximum number of pixels
- Circularity
- Aspect ratio

Using the above elements it was possible to construct a feature filter, which could discriminate between macroparticles and debris giving a size distribution. Such a filter has parallels in other spheres i.e. low pass, high pass and band pass filters in the audio domain. This filter should, in theory, allow the computer to accurately discriminate between genuine macroparticles and debris or surface imperfections. Unfortunately during experimental work it was found that using the Featurescan method produced

particle counts which were exaggerated by up to 10%, hence as a counting tool it was not suitable. However if each frame is checked individually then it is possible to tailor the threshold levels, used to differentiate between particulates and macroparticles, so that no debris is included in the count thus giving a valid approximation of the size distribution. In order to provide a more in depth analysis for size analysis purposes this means that a smaller sample of the whole frame set, 10% of the total number of frames studied, are examined to provide the distribution.

6.5 Experimental Results

The results presented in this chapter were obtained with the system as outlined in chapter 4, and using Nitrogen as the reactive gas to a partial pressure of 40mTorr. An arc current of 80A was used with a coating time of 30 seconds per run. Each sample was polished and cleaned, as outlined in 6.2, and affixed to a sample holder in the appropriate position. A bias voltage of -40V, with respect to the chamber, was applied to the samples via the insulated holding plate. It was determined that such a bias would increase adhesion of the coating to the sample, thus reducing imperfections in the surface of the coating and debris present on the samples.

A range of magnetic fields were then applied during deposition to study the effect on macroparticle deposition. These fields were generated by the novel 3 coil magnetic steering array, described in chapter 4, with the field profiles chosen to produce an orbital radius of the arc of 22mm, to which the sample holder had been optimised. As has been mentioned previously a total of 20 frames per sample were taken and the macroparticles counted. In addition to this 2 of the 20 frames were analysed using the Featurescan software enabling an approximate size distribution per sample to be arrived at.

The following sections show the results obtained from the experiments and relate the angular and size distribution of the macroparticles to the magnetic field components, and the conclusions which can be drawn from such results. The angle used is described as the angle between the normal from the surface of the cathode and the path of the macroparticles ejected from the cathode, Fig 6.3, and is represented by the symbol θ_e .

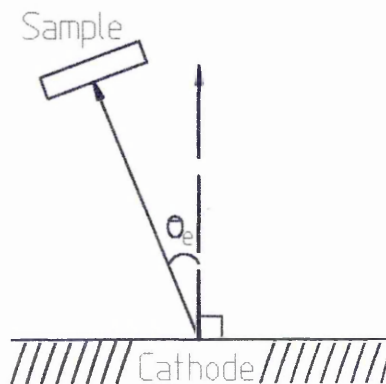


Fig 6.3, Diagram to illustrate the angle notation used in this thesis

6.5.1 ANGULAR DISTRIBUTION

Field Settings: $B_N' = 657.6 \text{ mTm}^{-1}$

$B_T = 10.46 \text{ mT}$

θ_e	$\rho_m(\times 10^{10})$	$\rho_m(\times 10^{10})$	$\rho_m(\times 10^{10})$
(\pm°)	RUN1	RUN2	RUN3
	(Particles/m ²)	(Particles/m ²)	(Particles/m ²)
0	1.78	1.77	1.80
9	1.56	1.68	1.53
25	1.59	1.57	1.58
44	1.37	1.50	1.37
63	1.13	1.14	1.14
79	0.74	0.64	0.68

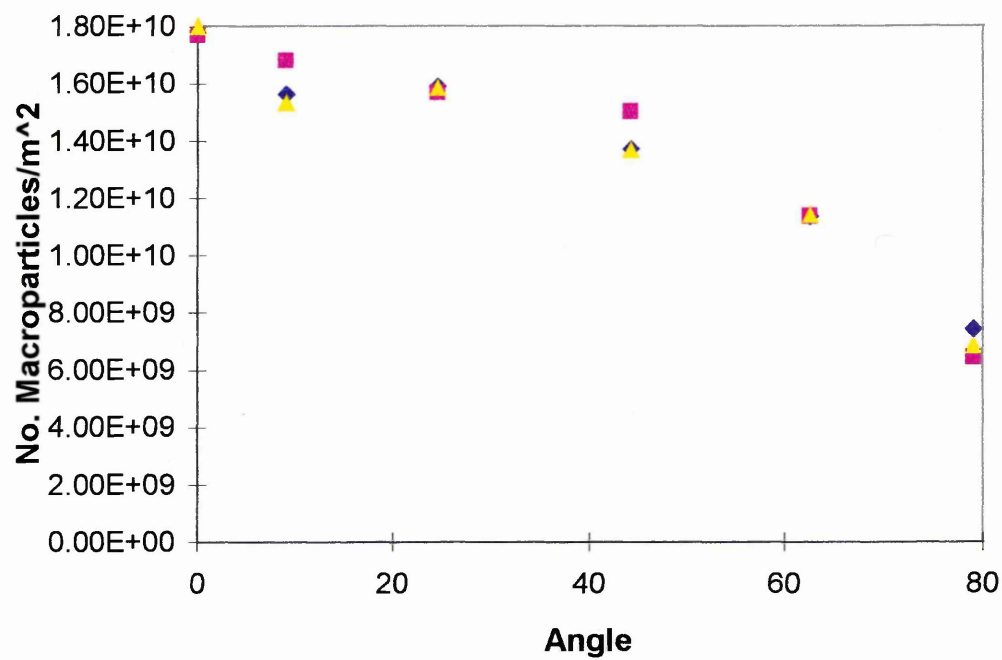


Fig 6.4, Plot of θ_e vs. ρ_m for $B_N' = 657.6 \text{ mTm}^{-1}$, $B_T = 10.46 \text{ mT}$

Field Settings: $B_N = 490.0 \text{ mTm}^{-1}$

$B_T = 7.45 \text{ mT}$

θ_e	$\rho_m(\times 10^{10})$	$\rho_m(\times 10^{10})$	$\rho_m(\times 10^{10})$
(\pm°)	RUN1	RUN2	RUN3
	(Particles/m ²)	(Particles/m ²)	(Particles/m ²)
0	2.78	2.72	2.74
9	2.65	2.70	2.56
25	2.50	2.53	2.5
44	2.04	1.92	2.00
63	1.29	1.27	1.24
79	0.85	0.92	0.78

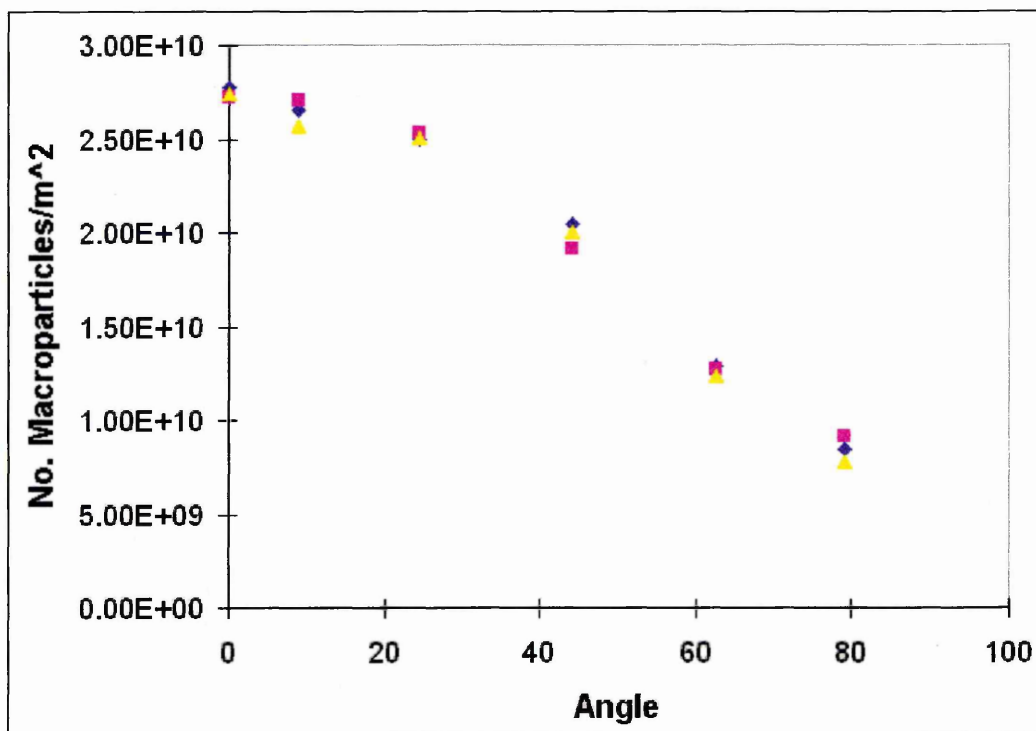


Fig 6.5, Plot of θ_e vs. ρ_m for $B_N = 490.0 \text{ mTm}^{-1}$, $B_T = 7.45 \text{ mT}$

Field Settings: $B_N' = 413.8 \text{ mTm}^{-1}$

$B_T = 6.52 \text{ mT}$

θ_e	$\rho_m(\times 10^{10})$	$\rho_m(\times 10^{10})$	$\rho_m(\times 10^{10})$
(\pm°)	RUN1	RUN2	RUN3
	(Particles/m ²)	(Particles/m ²)	(Particles/m ²)
0	3.42	3.42	3.41
9	3.22	3.21	3.02
25	2.65	2.83	2.75
44	2.62	2.57	2.33
63	1.38	1.46	1.45
79	0.93	0.91	0.73

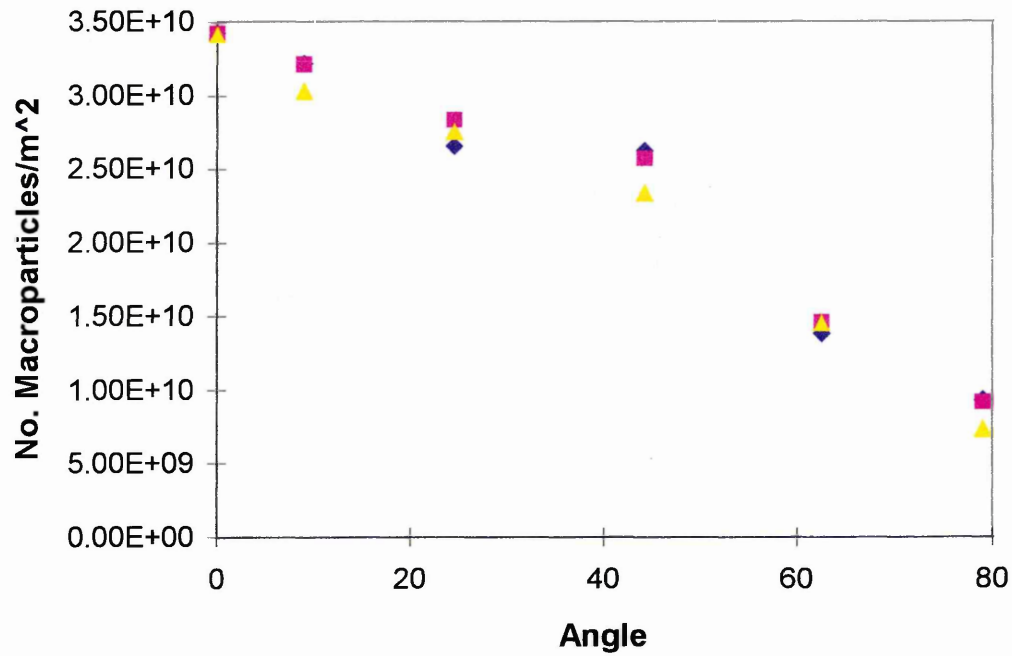


Fig 6.6, Plot of θ_e vs. ρ_m for $B_N' = 413.8 \text{ mTm}^{-1}$, $B_T = 6.52 \text{ mT}$

The effect of the magnetic field settings on angular distribution of the macroparticles can be seen in Fig 6.7, which combines Figs 6.3 to 6.6 onto a single set of axes.

As can be seen the magnitude of both the normal field gradient and transverse field components are given for each experimental set, this is so that a complete understanding of the effect of the applied magnetic field on the cathode spot can be arrived at.

It should also be noted that the values obtained for ρ_m for the three runs per experimental set are consistent with each other, such agreement leads to even greater confidence in the “blind” counting method used to obtain the results.

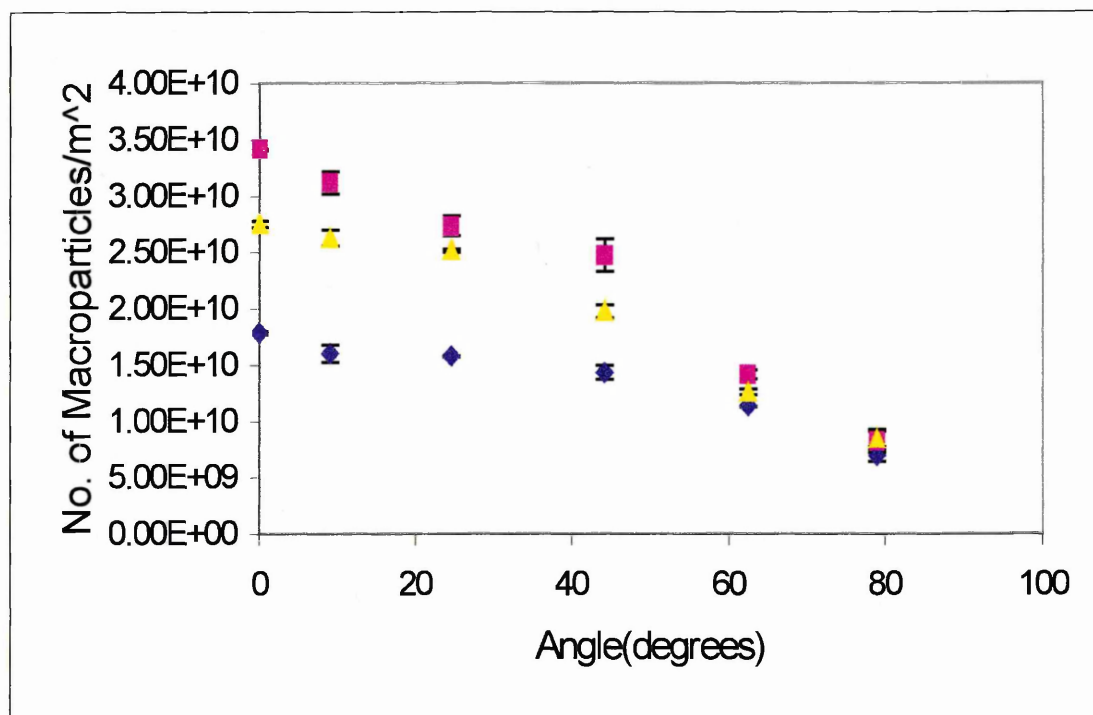


Fig 6.7, Plot of θ_e vs. ρ_m for the range of magnetic field settings

From this plot it is clear that as the magnitude of both B_N' and B_T increase then the macroparticle density decreases. To assess the effect fully it is necessary to investigate the behaviour of the cathode spot under these conditions, hence the following table derives a value for velocity of the arc (v) and also standard deviation of the arc spot from $B_N=0$ position (σ) from Fig 5.18 and 5.13 respectively.

$B_N'(\text{mTm}^{-1})$	$B_T(\text{mT})$	$B_N'/B_T(\text{m}^{-1})$	$v(\text{m/s})$	σ
658	10.5	62.7	27	1.3
490	7.5	65.3	20.7	1.8
414	6.5	63.7	18	2.2

From the above the implications of the variation in applied magnetic field can be seen in terms of the effect on the motion of the arc. Thus the decrease in ρ_m occurs whilst the velocity of the arc increases and the confinement of the arc decreases. Since the production of macroparticles increases as the temperature of the cathode increases[1] then it follows that an increase in velocity would mean that the dwell time of the arc is reduced, and hence the temperature of the cathode is reduced. In addition to this the effect of the change in σ must also be considered, since as the magnetic field is increased the deviation of the arc from its path decreases thus also affecting the dwell time of the arc spot. From these results it would seem that the parameter which dominates the macroparticle density is the velocity at which the arc moves around the cathode. To make certain of this relationship it is envisaged that more experimental investigation is required, see chapter 7 for greater detail.

Figure 6.7 also has a bearing on work if we examine the results from a coating viewpoint. Since the aim of the production of a film is to minimise the surface roughness, and hence macroparticle content, then the results indicate the best geometry between the samples and cathode. The data presented here shows that by judicious choice of θ_c it is possible to reduce ρ_m by approximately 50%, with the largest reduction being at low angles and high speed.

If we now consider comparing the results presented here to ones obtained by other authors[1,2,3] we find difficulties. Some of these are due to the operating conditions/geometry of the experimental apparatus, whilst others are due to the lack of variety of angles investigated; Swift[2] for example only considered one angle, $\theta_c=80^\circ$. In the experiments presented in chapter 5 variations in B_N/B_T are demonstrated which exceed the ability of previous authors[4], 25% instead of 8%. In the case of results presented here only a small variance was achieved, though if further work was to be considered this would be an avenue to investigate(see chapter 7).

If we put aside such reservations and consider the comparison of this work to previous studies then it can be seen that there is broad agreement between the work of Swift[2] and current work(table 6.1), with the results being of less than an order of magnitude different despite variations in operating conditions and apparatus geometry. The results also concur with those obtained by other authors such as Tai[5] who obtained a value of

$\rho_m = (1.4 \pm 0.3) \times 10^{10}$ macroparticles/ m^2 and Münz et al [6] with $\rho_m = 2.4 \times 10^{10}$ macroparticles/ m^2 . In addition to this our results also exhibit the well documented trend of ρ_m decreasing as B_T increases as has been observed by other authors[1, 2, 3, 5].

Table 6.1, Comparison of ρ_m vs. B_T for θ_e of 79° and 80° .

B_T mT	V_{arc} (± 1.1m/s)	Approx. $\rho_m(AC)$ $\times 10^{10}$ macro's/m^2	$(\rho_m * V_{arc})_{AC}$ $\times 10^{10}$ macro's/ms	Approx. $\rho_m(Swift)$ $\times 10^{10}$ macro's/m^2	$(\rho_m * V_{arc})_{Swift}$ $\times 10^{10}$ macro's/ms
10.5	23.1	0.7	15.7 ± 0.8	3.5	80.8
7.5	19.8	0.85	16.9 ± 1.0	4.2	83.2
6.5	18.1	0.93	16.0 ± 1.0	4.3	72.83

Swift also makes the observation that for his results the value of $(\rho_m * V_{arc})$ is a constant. If we examine the results presented here, and in the paper by Swift, then it is possible to derive values for V_{arc} and ρ_m from graphical sources with the errors being due to the scatter of the experimental data. Thus upon calculation it can be seen that our values of $(\rho_m * V_{arc})$ also remain constant, within experimental error, thus agreeing with the observation of Swift.

6.4.2 SIZE DISTRIBUTION

As was mentioned previously 2 frames from each sample were analysed using the "Featurescan" software to give an approximate size distribution of macroparticles, in relation to both angle and magnetic field settings. The cross sectional area of the macroparticle is used to describe the size of a particle.

The frequency of occurrence of the macroparticles, expressed as the relative frequency, is then plotted against the area for the range of angles being studied.

Field Settings: $B_N' = 657.6 \text{ mTm}^{-1}$

$B_T = 10.46 \text{ mT}$

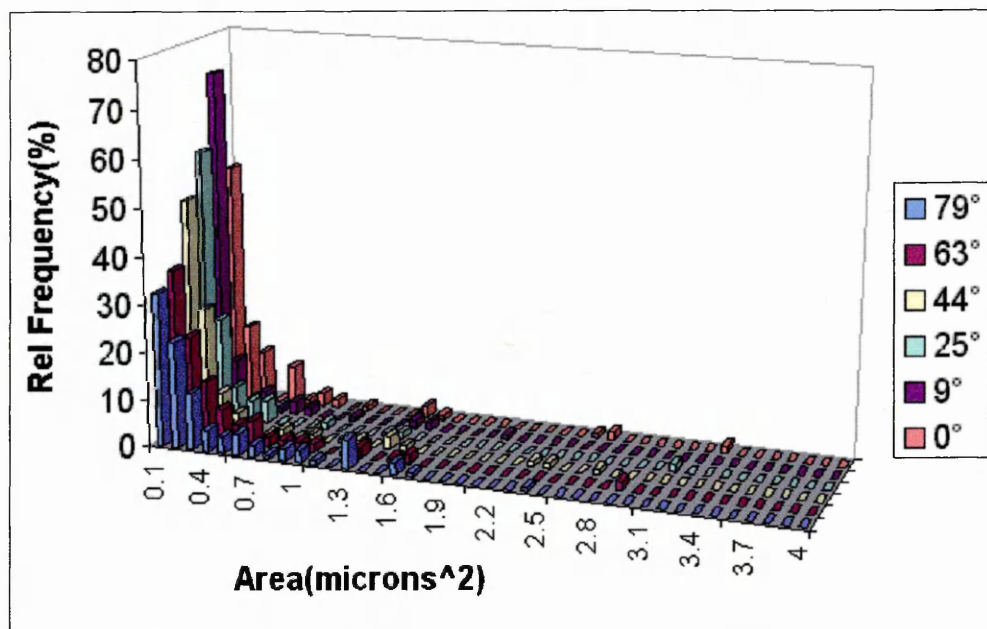


Fig 6.8, Plot of Cross sectional area vs. Relative frequency of occurrence for the various angles

Field Settings: $B_N' = 490.0 \text{ mTm}^{-1}$

$B_T = 7.45 \text{ mT}$

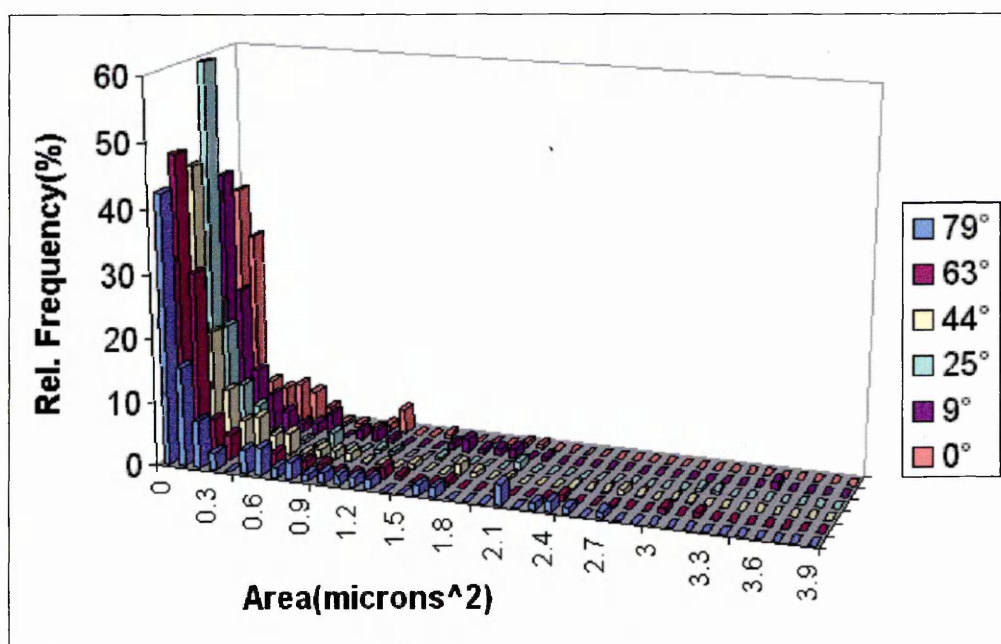


Fig 6.9, Plot of Cross sectional area vs. Relative frequency of occurrence for the various angles

Field Settings: $B_N' = 413.8 \text{ mTm}^{-1}$,
 $B_T = 6.52 \text{ mT}$

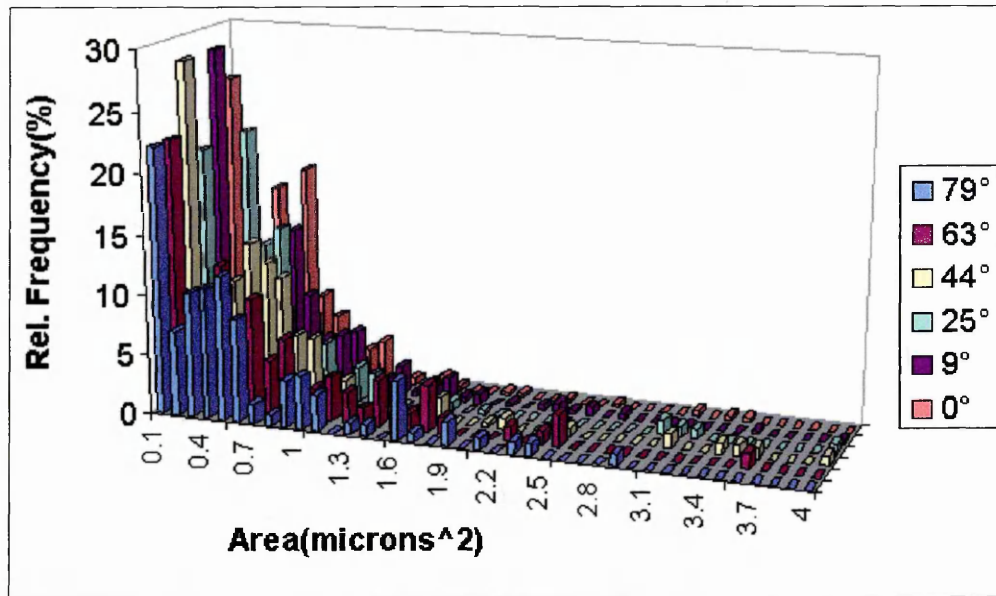
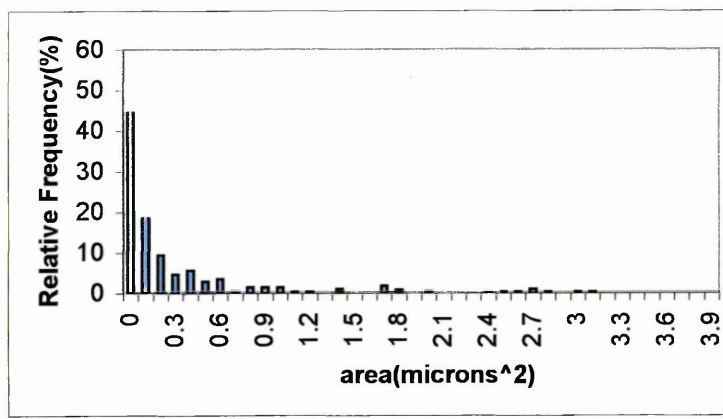


Fig 6.10, Plot of Cross sectional area vs. Relative frequency of occurrence for the various angles

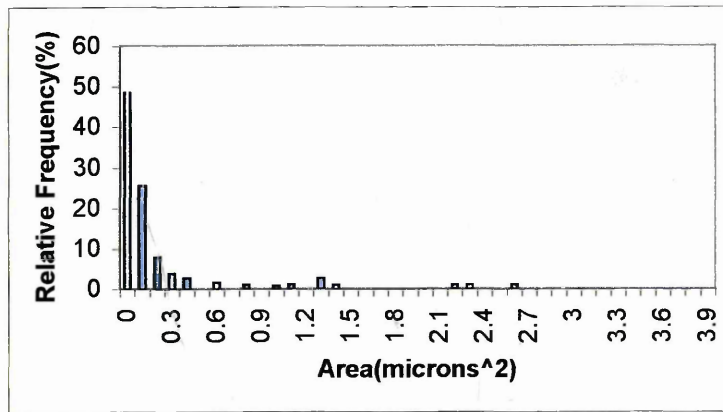
From Figs. 6.8-6.10 we can see three main points:

1. The rapid tail off of the number of macroparticles as their area increases
2. A peak in the relative frequency of the macroparticles in the range 9°-25°.
3. The shift towards larger area macroparticles as B_T is decreased. Such a shift agrees well with other authors[2, 3] and is thought to be due to the decrease in velocity of the cathode spot, and hence an increase in spot temperature, of the arc.

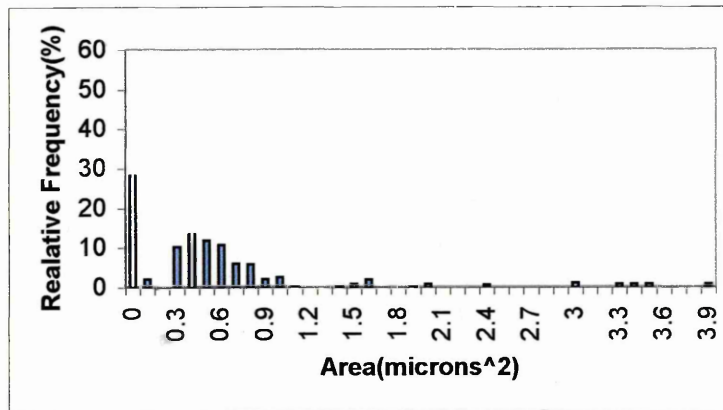
In order that these points can be viewed more clearly plots of relative frequency of occurrence vs. macroparticle area at $\theta_c = 44^\circ$ for the variety of B_T settings are shown as Fig 6.11.



$$B_N' = 657.8 \text{ mTm}^{-1}, B_T = 10.46 \text{ mT}$$



$$B_N' = 490.0 \text{ mTm}^{-1}, B_T = 7.45 \text{ mT}$$



$$B_N' = 413.8 \text{ mTm}^{-1}, B_T = 6.52 \text{ mT}$$

Fig 6.11, Plot of Cross sectional area vs. Relative frequency of occurrence for $\theta_e = 44^\circ$, for a range of magnetic fields

In addition to these plots data has been drawn together which provides values for the average area of macroparticles for each set of experiments, and is presented as Table 6.2. This table, as well as showing data for the average area of macroparticles, also has a value for average radius. Such a figure is arrived at by assuming the image of the macroparticle is circular.

B_T	Angle, $\theta_e(^{\circ})$					
	79	63	44	25	9	0
10.5	0.50 (0.07)	0.27 (0.05)	0.34 (0.05)	0.21 (0.04)	0.36 (0.06)	0.27 (0.03)
7.5	0.38 (0.05)	0.34 (0.05)	0.28 (0.05)	0.21 (0.04)	0.18 (0.03)	0.33 (0.06)
6.5	0.57 (0.06)	0.69 (0.07)	0.63 (0.07)	0.54 (0.06)	0.56 (0.06)	0.50 (0.05)

Table 6.2, values for average area(μm^2) and average radius(μm) of macroparticles, radius signified by (value).

The above results are shown graphically as Fig 6.12

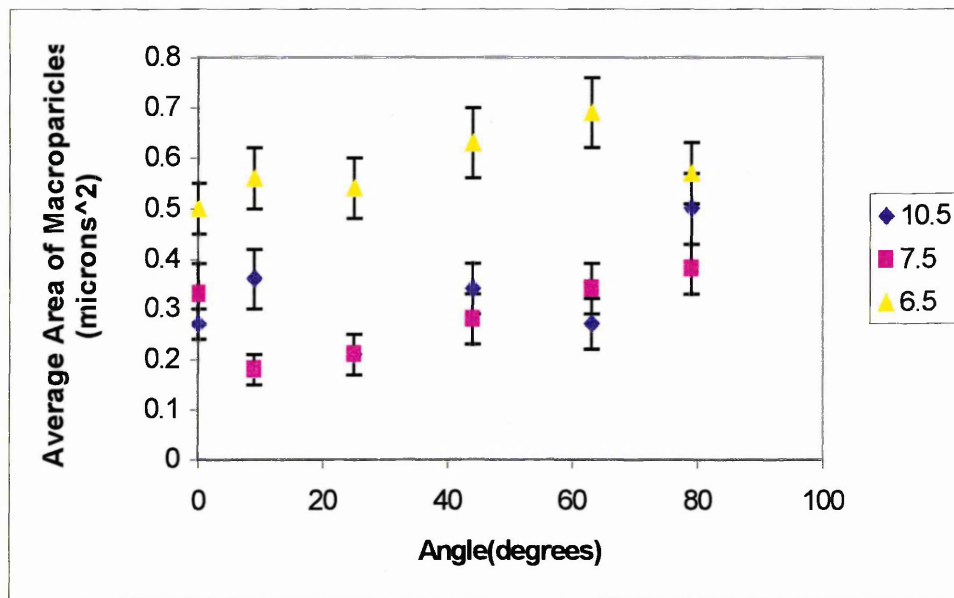


Fig 6.12, Plot of the average area of macroparticle vs. θ_e for a range of B_T values

The most notable conclusion from these plots is the increase in average size of the macroparticles as the angles increases, as found by Disatnik et al[7], thus indicating the most advantageous placement of samples if smooth coatings were required. In addition to this the data obtained also suggest that the relationship between B_T and macroparticle size is not a straight forward one.

From the experimental results presented here it is seen that there is a general agreement with the work of previous authors on the size and number density distributions of macroparticles. However this work goes further than others by showing the distributions for a range of angles (0° - 79°) highlighting the implications for the use of CAPVD in coating systems. Such an experimental arrangement also holds the prospect of the analysis of the effect of the variation of the B_N'/B_T ratio on the macroparticle flux, since using this apparatus the ability to vary this ratio by 25% has been demonstrated.

REFERENCES

- [1] E Ertürk, H S Heuval, H G Dederichs
Surface & Coatings Technology 39/40 (1989) 455

- [2] P D Swift
Journal of Physics D: Applied Physics 29 (1996) 2025

- [3] A W Baouchi, A J Perry
Surface & Coatings Technology 49 (1991) 253

- [4] P J Walke
PhD Thesis, Sheffield Hallam University, September 1994

- [5] C N Tai, E S Koh, K Akari
Surface & Coatings Technology 43/44 (1990) 324

- [6] W D Münz, I J Smith, D B Lewis, S Creasey
Vacuum 48(5) (1997) 473

- [7] G Disatnik, R Boxman, S Goldsmith
IEEE Transactions on Plasma Science 15(5) (1987) 520

7.0 SUMMARY AND FURTHER WORK

The aim of this chapter can be divided into two distinct parts; firstly there is the summary of experimental work performed (presented in chapters 5 and 6) and secondly there are suggestions for further work which are considered useful avenues of study. These suggestions not only encompass work which would allow points presented here to be clarified, but also covers research which it is hoped would lead to the further advancement of cathodic arc as a viable method of producing thin film coatings.

7.1 Summary Of The Results

Chapter 4 describes the design and construction of a novel three coil electromagnetic steering array for the control for the motion of the cathodic arc. It was initially hoped that such an array would permit comprehensive testing of the stochastic model proposed by Care[1], but due to the dimensional limitations of the vacuum system being used this was not possible. However such a steering system was designed and constructed which significantly extended the scope of the magnetic field settings available, leading to a significantly wider range in the ratio of B_N'/B_T than was previously obtainable. The chapter also describes the work which was undertaken which enabled the existing vacuum chamber to be utilised for longer periods of time. Such an extension in usable time of operation led to the possibility of producing/studying the coating process, in particular the production of macroparticles.

Chapter 5 describes the study of the motion of the arc given the extra control from the steering array. Several parameters were of interest which would add to results of previous authors[2,3,4], as well as furthering the testing of the stochastic model. These parameters are:

- Standard deviation of the arc radius(σ) as a function of magnetic field
- Orbital period of the arc(thus velocity) as a function of magnetic field
- Diffusion constant of the arc motion(α) as a function of magnetic field

The investigation of the above parameters was enhanced by the design and construction of new arc monitoring equipment, and software. Such apparatus allowed the standard deviation of the arc radius and orbital period to be measured in a single experiment. The equipment consisted of a linear photodiode array whose outputs, after suitable processing, were passed to a personal computer via two data acquisition cards.

(a) σ vs. magnetic steering fields

The orbital radius of the arc was measured as it passed the detector array and hence by studying many orbits a value of σ could be arrived at. By varying the coil current settings it was possible to change the magnetic field profile, whilst still keeping the mean radius of 2.2cm. In the model proposed by Care[1] it is hypothesised that the arc is controlled by a combination of B_N' and B_T , with a plot of σ vs. $(B_N'B_T)^{-0.5}$ expected to be linear and passing through the origin. Using the experimental data an appraisal of

the relationship was undertaken to ascertain whether the relationship between σ and the magnetic field was as predicted by the stochastic model. The result of this appraisal was that there was close agreement as outlined in the expression below,

$$\sigma \propto B_N^{-(0.47 \pm 0.02)} B_T^{-(0.54 \pm 0.02)}$$

(b) *velocity(v) vs. magnetic field & diffusion constant(α) vs. magnetic field*

The second part of chapter 5 deals with analysis of the velocity of the arc and the diffusion constant vs. the magnetic field. Such a study was undertaken by producing a frequency distribution of the orbital period of the arc motion and comparing it with that of the distribution predicted by the stochastic model. This was performed using a Kologmorov-Smirnov test which allowed the comparison of a continuous function to grouped data. It was found that in all cases the fit between experimental values and those predicted by the model were in agreement to within 1% confidence, thus strongly supporting the stochastic model of arc motion proposed by Care.

During the fitting routine values for v and α were produced, the values of v generated showed good agreement with previous authors[2,4,5], once corrections for differences in arc current and backing gas pressure had been accounted for.

The results for α however displayed a discrepancy between previously obtained values. It is thought that the operational parameters, such as arc current and pressure, could account for such variations. Further areas of research are suggested to clarify this position in 7.2(b).

In conclusion it may be said that the work presented here supports the stochastic description of arc motion as proposed by Care. However further work is required before the level of support of the model can be gauged. Section 7.2 outlines a number of areas of investigation which it is thought will allow the unambiguous testing of the model of arc motion.

Chapter 6 concentrates on one of the drawbacks when using cathodic arc PVD in a commercial system, in particular the study of the generation of macroparticles from the cathode spot. Such macroparticles have been studied previously but not with the ability to vary the magnetic field profiles in such a way. The work presented here brings together the examination of macroparticle size and number density as a function of angle of emission as well as looking into the effect of variation in the magnitude of the

magnetic field. It showed that as the magnetic field was decreased there was an increase in number density of macroparticles. These observations were then examined taking account of v and σ , leading to the observation that the velocity of the arc is the primary factor affecting macroparticle generation, since as the velocity of the arc decreases then the dwell time of the arc increases leading to an increase in the local temperature of the cathode. The macroparticle densities also showed that most of the macroparticle flux consists of smaller droplets. When a comparison of results presented was made with those of previous authors, in terms of macroparticle densities, then it could be seen that there was good agreement.

In terms of size distribution of the macroparticles, a representative sample of frames was taken and analysed using image processing software. Plots of cross sectional area vs. relative frequency for a range of angles were produced. Such plots highlighted a peak in the macroparticle number density in the 9° - 25° range of angles, in addition it was also possible to see a shift to large cross sectional areas as B_T was decreased agreeing with others authors[8,12].

7.2 RECOMMENDATIONS FOR FURTHER WORK

After studying the results presented in chapters 5 and 6 areas of further interest became apparent. The following is a list of ideas which would either help in the testing of the model of the arc or alternatively provide useful avenues for further research. This section is divided into two distinct parts:

(i) Work to study the motion of the arc

- Results for a larger combination of field settings. Although a number of settings have been used throughout the study it is thought that additional work should extend the field variations further. Increased variation would enable a more in depth picture to be provided for the behaviour of σ, v and α as a function of field. It is thought that such extra field settings will not be possible using the current magnet arrangement and that in fact a new coil assembly will be required to provide the necessary variation.
- Study of the effect of an erosion track on the motion and behaviour of the arc. This could be performed by using a single coil setting and repeatably running the arc around the same track, thus as the track erodes any changes in σ, v and α can be analysed. In addition to this it may also be of interest to study the effect of the gradient of the side of the trench on the motion of the arc. Such a study could be performed using machined trenches of various gradients, from flat cathodes to vertical sided trenches.
- Further study/testing of the stochastic model of arc motion. Such study would require the construction of a new vacuum chamber, the size of which would be determined by the dimensions of the new three coil steering array. The philosophy behind this would be to allow a set of electromagnets to be constructed whose combination of field profiles would allow significantly wider control of the arc. Such a system should also be designed to allow coating/macroparticle studies to be undertaken.

- Study of the effect of variations in pressure and arc current on the motion of the arc under an applied electromagnetic steering field. These parameters are of interest in resolving the discrepancy which was found in the values of diffusion constant.

(ii) work to study macroparticle and coating production

- Use of a new chamber and magnetic steering to further examine the effect of the magnetic field on the macroparticle emission. Such a coil system would be able to offer the prospect of B_N'/B_T settings radically different from those available from the current steering array, allowing the field elements to be changed independently of each other.
- Continuing the work of Donohue[9] by studying the production of coatings using a segmented cathode. Such work would require the investigation of field modifying coils to overcome the reluctance of the arc to cross material boundaries.
- Production of software and a computer interface to provide computer control of the cathodic arc. Once a three coil magnetic steering array has been constructed then the next phase for coatings is to provide a means of control of the arc which when given vital parameters could sweep the arc radii producing a vapour flux of consistent parameters. Such a system would be able to increase usage of the cathode, as well as producing a flux with a known level of macroparticle contamination.

REFERENCES

- [1] C M Care
Journal of Physics D: Applied Physics 25(1992)1841

- [2] P J Walke
PhD Thesis, Sheffield Hallam University, September 1994

- [3] P J Walke, R New, C M Care
Surface and Coatings Technology 59(1993)126

- [4] P J Walke, R New, C M Care
Surface and Coatings Technology 68/69(1994)352

- [5] P D Swift
Journal of Physics D: Applied Physics 29(1996)2025

- [6] W D Münz, I J Smith, D B Lewis, S Creasey
Vacuum 48(5) (1997) 473

- [7] C N Tai, E S Koh, K Akari
Surface and Coatings Technology 43/44(1990)324

- [8] A W Baouchi, A J Perry
Surface and Coatings Technology 49(1991)253

- [9] L A Donohue
PhD Thesis, Sheffield Hallam University, November 1995

APPENDIX A

TWO & THREE COIL MAGNETIC EQUATION

Mathematics Of The Two Coil System

Checking on work done by Dr R New

$B_T^{(x)}$ - Transverse magnetic field component in the x_{th} coil

$B_N^{(x)}$ - Normal magnetic field component in the x_{th} coil

$B_N'^{(x)}$ - Gradient of the normal field in the x_{th} coil

$K_N^{(x)}$ - A value which varies with radius and describes the shape of the field in the normal direction, in the x_{th} coil

$I^{(x)}$ - A value which varies with the radius and describes the shape of the field in the transverse direction, in the x_{th} coil

$k_T^{(x)}$ - A value dependant on the radius of orbit, for the x_{th} coil

$$B_T = B_T^{(1)} + B_T^{(2)}$$

$$= k_T^{(1)} I^{(1)} + k_T^{(2)} I^{(2)}$$

$$\& B_N = k_N^{(1)} I^{(1)} + k_N^{(2)} I^{(2)}$$

Since the K's are dependant upon the radius. Thus there is a value of r for which $B_N=0$, at this point

$$\frac{I^{(1)}}{I^{(2)}} = \frac{-k_N^{(2)}}{k_N^{(1)}}$$

The above can be rearranged to give a formula for $I^{(2)}$ which can be substituted into the equation for

B_T giving

$$B_T = \left(k_T^{(1)} - \frac{k_T^{(2)} k_N^{(1)}}{k_N^{(2)}} \right) I^{(1)}$$

$$ie \quad B_T \propto I^{(1)}$$

Also differentiating the equation for B_N gives

$$\frac{dB_N}{dr} = \frac{dk_N^{(1)}}{dr} I^{(1)} + \frac{dk_N^{(2)}}{dr} I^{(2)}$$

substituting in for $I^{(2)}$ and rearranging gives

$$\frac{dB_N}{dr} = I^{(1)} \left(\frac{dk_N^{(1)}}{dr} - \frac{dk_N^{(2)}}{dr} \frac{k_N^{(1)}}{k_N^{(2)}} \right)$$

$$ie \quad B_T \propto B_N'$$

Mathematics Of The Three Coil System

Checking on work done by Dr R New

$B_T^{(x)}$ - Transverse magnetic field component in the x_{th} coil

$B_N^{(x)}$ - Normal magnetic field component in the x_{th} coil

$B_N'^{(x)}$ - Gradient of the normal field in the x_{th} coil

$K_N^{(x)}$ - A value which varies with radius and describes the shape of the field in the normal direction, in the x_{th} coil

$I^{(x)}$ - A value which varies with the radius and describes the shape of the field in the transverse direction, in the x_{th} coil

$\frac{dK_N^{(x)}}{dr}$ - Gradient of the shape constant for the x_{th} coil

$$B_N = 0 \text{ when } \sum_{i=1}^{i=x} K_N^{(i)} I^{(i)} = 0$$

ie for the three coil case, $x=3$

$$K_N^{(1)} I^{(1)} + K_N^{(2)} I^{(2)} + K_N^{(3)} I^{(3)} = 0$$

rearranging the above gives

$$I^{(1)} = -(K_N^{(2)} I^{(2)} + K_N^{(3)} I^{(3)}) / K_N^{(1)}$$

Using this in the equation for B_N gives

$$B_N = K_N^{(1)} (-K_N^{(2)} I^{(2)} + K_N^{(3)} I^{(3)} / K_N^{(1)}) + K_N^{(2)} I^{(2)} + K_N^{(3)} I^{(3)}$$

differentiating this with respect to r gives

$$\begin{aligned} \frac{dB_N}{dr} &= B_N' = -\frac{dK_N^{(1)}}{dr} (K_N^{(2)} I^{(2)} - K_N^{(3)} I^{(3)} / K_N^{(1)}) + \frac{dK_N^{(2)}}{dr} I^{(2)} + \frac{dK_N^{(3)}}{dr} I^{(3)} \\ &= \frac{dK_N^{(2)}}{dr} I^{(2)} - \frac{dK_N^{(1)}}{dr} \frac{K_N^{(2)} I^{(2)}}{K_N^{(1)}} + \frac{dK_N^{(3)}}{dr} I^{(3)} - \frac{dK_N^{(1)}}{dr} \frac{K_N^{(3)} I^{(3)}}{K_N^{(1)}} \\ &= I^{(2)} \left(\frac{dK_N^{(2)}}{dr} - \frac{dK_N^{(1)}}{dr} \frac{K_N^{(2)}}{K_N^{(1)}} \right) + I^{(3)} \left(\frac{dK_N^{(3)}}{dr} - \frac{dK_N^{(1)}}{dr} \frac{K_N^{(3)}}{K_N^{(1)}} \right) \end{aligned}$$

To simplify the equations let us define

$$\alpha_N^{(21)} = \left(\frac{dK_N^{(2)}}{dr} - \frac{dK_N^{(1)}}{dr} \frac{K_N^{(2)}}{K_N^{(1)}} \right)$$

$$\alpha_N^{(31)} = \left(\frac{dK_N^{(3)}}{dr} - \frac{dK_N^{(1)}}{dr} \frac{K_N^{(3)}}{K_N^{(1)}} \right)$$

$$\text{ie } B'_N = I^{(2)}\alpha^{(21)} + I^{(3)}\alpha^{(31)}$$

$$\begin{aligned} \text{Also } B_T &= B_T^{(1)} + B_T^{(2)} + B_T^{(3)} \\ &= K_T^{(1)}I^{(1)} + K_T^{(2)}I^{(2)} + K_T^{(3)}I^{(3)} \end{aligned}$$

substituting in into the above for $I^{(1)}$ gives

$$\begin{aligned} B_T &= -K_T^{(1)}\left(K_N^{(2)}I^{(2)} + K_N^{(3)}I^{(3)} / K_N^{(1)}\right) + K_T^{(2)}I^{(2)} + K_T^{(3)}I^{(3)} \\ &= K_T^{(2)}I^{(2)} - \frac{K_T^{(1)}K_N^{(2)}}{K_N^{(1)}}I^{(2)} + K_T^{(3)}I^{(3)} - \frac{K_T^{(1)}K_N^{(3)}}{K_N^{(1)}}I^{(3)} \\ &\equiv I^{(2)}\left(K_T^{(2)} - \frac{K_T^{(1)}K_N^{(2)}}{K_N^{(1)}}\right) + I^{(3)}\left(K_T^{(3)} - \frac{K_T^{(1)}K_N^{(3)}}{K_N^{(1)}}\right) \end{aligned}$$

Again we define the following to simplify the equations

$$\alpha_T^{(21)} = \left(K_T^{(2)} - \frac{K_T^{(1)}K_N^{(2)}}{K_N^{(1)}}\right)$$

$$\alpha_T^{(31)} = \left(K_T^{(3)} - \frac{K_T^{(1)}K_N^{(3)}}{K_N^{(1)}}\right)$$

$$\text{ie } B_T = I^{(2)}\alpha_T^{(21)} + I^{(3)}\alpha_T^{(31)}$$

Thus we now have two equations, one for B'_N and one for B_T

$$B'_N = I^{(2)}\alpha_N^{(21)} + I^{(3)}\alpha_N^{(31)}$$

and

$$B_T = I^{(2)}\alpha_T^{(21)} + I^{(3)}\alpha_T^{(31)}$$

APPENDIX B

PROGRAM DOCUMENTATION

```

REM*****
REM PROGRAM NAME:      ATMEX.BAS
REM AUTHOR:           ADRIAN CRAVEN
REM DATE LAST MODIFIED: 28/3/1996
REM
REM FUNCTION:  THIS PROGRAM IS BASED ON THE ARCTIME PROGRAM WRITTEN
REM            BY P.WALKE(1993/4). IT USES COUNTERS ON ATMIO16 BOARD TO
REM            TIME THE ARC PULSES, BUT NOW ALSO USES A PCDIO96 TO
REM            READ THE DETECTOR OUTPUTS TO CHECK FOR CONFINEMENT
REM            OF THE ARC
REM*****

```

REM DEFINING OF ARRAYS AND OTHER VARIABLES

```

DIM SHARED period#(4000), sumdif#(8), totdif#(8), sortper#(3000)
DIM SHARED pt0#(4000), pt1#(4000)
DIM fs AS STRING * 9
DIM ffn AS STRING * 30
DIM ffnpt0 AS STRING * 30
DIM ffnpt1 AS STRING * 30
drive$ = "e:\pwprogs\"
ext$ = ".dat"
ext0$ = ".pt0"
ext1$ = ".pt1"

```

REM CONFIGURING THE COUNTERS AND DIGITAL PORTS

```

i..dummy% = CTR.Config(2, 1, 1, 0, 0, 0)
i..dummy% = CTR.Config(2, 2, 0, 3, 0, 0)
i..dummy% = CTR.Config(2, 5, 0, 3, 0, 0)
i..ret% = DIG.Prt.Config(1, 0, 0, 0)
i..ret% = DIG.Prt.Config(1, 1, 0, 0)
WHILE dummy% = 0
CLS

```

REM START OF PROGRAM

```

INPUT "How many pulses"; adi%

```

```

n% = 2000
n2% = 4000
FOR i% = 0 TO adi%

```

REM START COUNTER1 COUNTING EVENTS AT GATE 1

```

i..dummy% = CTR.EvCount(2, 1, 11, 0)

```

REM WAIT UNTIL EVENT OCCURS AT GATE 1

```
WHILE evnt% = 0
  i..dummy% = CTR.EvRead(2, 1, dumm%, evnt%)
WEND
```

REM RESET COUNTER1

```
evnt% = 0
i..dummy% = CTR.Reset(2, 1, 1)
```

REM READ TIME AT COUNTER2 & SAVE TO ARRAY

REM ALSO READ THE DIGITAL INPUT PORTS & SAVE TO ARRAY

```
i..dummy% = CTR.EvRead(2, 2, dumm2%, pertemp1%)
i..ret% = DIG.In.Port(1, 0, port0%)
i..ret% = DIG.In.Port(1, 1, port1%)
cnt% = cnt% + 1
period#(cnt%) = CINT(pertemp1%)
pt0#(cnt%) = CINT(port0%)
pt1#(cnt%) = CINT(port1%)
```

REM CONFIGURE COUNTER2 TO MEASURE PERIOD WITH 1MHz CLOCK

```
i..dummy% = CTR.Period(2, 2, 1)
```

REM START COUNTER1 COUNTING EVENTS AT GATE1

```
i..dummy% = CTR.EvCount(2, 1, 11, 0)
```

REM WAIT UNTIL EVENT OCCURS AT GATE1

```
WHILE evnt% = 0
  i..dummy% = CTR.EvRead(2, 1, dumm%, evnt%)
WEND
```

REM RESET COUNTER1

```
evnt% = 0
i..dummy% = CTR.Reset(2, 1, 1)
```

REM READ TIME AT COUNTER5 & SAVE TO ARRAY

REM ALSO READ DIGITAL INPUT PORTS & SAVE TO ARRAY

```
i..dummy% = CTR.EvRead(2, 5, dumm2%, pertemp2%)
i..ret% = DIG.In.Port(1, 0, port0%)
i..ret% = DIG.In.Port(1, 1, port1%)

cnt% = cnt% + 1
period#(cnt%) = CINT(pertemp2%)
```

```
pt0#(cnt%) = CINT(port0%)
pt1#(cnt%) = CINT(port1%)
```

REM CONFIGURE COUNTER5 TO MEASURE PERIOD WITH 1MHz CLOCK

```
i..dummy% = CTR.Period(2, 5, 1)
print i%
NEXT i%
```

```
PRINT "done"
BEEP
```

```
CALL StdDev(period#(), cnt%, meanie#, sd#)
PRINT "Mean and SD"; meanie#, sd#
```

REM SAVE THE ARRAYS TO FILE ON DISK

```
INPUT "File name please"; fs$
```

```
z% = fmt(ffn$, "%s<%s%s%s", drive$, fs$, ext$)
h% = 1
h% = OpenFile(ffn$, 2, 0, 1)
FOR i% = 0 TO adi%
  Zz% = FmtFile(h%, "%s<%f", period#(i%))
NEXT i%
i..dummy% = CloseFile(h%)
```

```
z1% = fmt(ffnpt0$, "%s<%s%s%s", drive$, fs$, ext0$)
z2% = fmt(ffnpt1$, "%s<%s%s%s", drive$, fs$, ext1$)
h1% = 1
h2% = 1
h1% = OpenFile(ffnpt0$, 2, 0, 1)
h2% = OpenFile(ffnpt1$, 2, 0, 1)
```

```
FOR i% = 0 TO adi%
  zz1% = FmtFile(h1%, "%s<%f", pt0#(i%))
  zz2% = FmtFile(h2%, "%s<%f", pt1#(i%))
NEXT i%
i..dummy% = CloseFile(h1%)
i..dummy% = CloseFile(h2%)
cnt% = 0
WEND
```

```

REM*****
REM
REM PROGRAM NAME:      DATAANAL.BAS
REM AUTHOR:           ADRIAN CRAVEN
REM DATE LAST MODIFIED: 14/5/97
REM
REM FUNCTION:  THIS PROGRAM IS BASED UPON A PREVIOUS PROGRAM BY
REM P.WALKE AND READS IN A SERIES OF ORBITAL PERIODS COLLECTED BY THE
REM ARC TIMING PROGRAM. IT THEN FILTERS THE DATA OF ERRONEOUS VALUES
REM AND PRODUCES FREQUENCY DISTRIBUTION. ONCE THIS IS DONE THE MEAN,
REM STANDARD DEVIATION, STANDARD ERROR AND SKEW ARE CALCULATED
REM AND THE RELEVANT INFORMATION IS SAVED TO FILES.
REM
REM*****

```

```

DIM SHARED V(2000), FLTR1(1000), FLTR2(1000), EXPY(20), XMBND(20), NRMV(20)

```

```

DRIV$ = "C:\ADISTUFF\THES_RES\"
EXT$ = ".DAT"
EXTOP$ = ".PER"

```

```

REM DECLARE VARIABLES AND THEIR START VALUES

```

```

CNT = 1
RAWNUM = 0
NUMSAMPS = 0
MAXVAL = 0
MINVAL = 1000000
SUM = PSUM = 0
SD = PSD = SDSUM = PSDSUM = SERROR = PSERROR = 0
PMEAN = MEAN = 0
INCREM = 0
NUMGDS = 0
MINGD = MAXGD = 0
L1 = L2 = L3 = L4 = L5 = L6 = L7 = L8 = L9 = 0
L10 = L11 = L12 = L13 = L14 = L15 = L16 = 0
MOM = THRDMOM = SKEW = 0
NUMPTS = 17
NUMBINS = 17
CLS

```

```

REM START OF PROGRAM

```

```

INPUT "TYPE FILENAME TO BE PROCESSED "; N$

```

```

REM INPUT "TYPE NUMBER OF SAMPLE ORBITS TAKEN "; NUMSAMPS

```


NUMSAMPS = 500

```
A$ = (DRIV$ + N$ + EXT$)
OPEN A$ FOR INPUT AS #1
O$ = (DRIV$ + N$ + EXTOP$)
OPEN O$ FOR OUTPUT AS #2
B$ = (DRIV$ + "X" + N$ + EXT$)
OPEN B$ FOR OUTPUT AS #3
C$ = (DRIV$ + "Y" + N$ + EXT$)
OPEN C$ FOR OUTPUT AS #4
D$ = (DRIV$ + "N" + N$ + EXT$)
OPEN D$ FOR OUTPUT AS #5
```

REM IMPORTING DATA FROM FILE GENERATED BY ARCTIMING PROGRAM

```
WHILE CNT < NUMSAMPS
  INPUT #1, A
  V(CNT) = A
  CNT = CNT + 1
WEND
```

CLOSE #1

REM FIRST DATA FILTER - (BAND PASS)

```
FOR CNT = 1 TO NUMSAMPS
  IF V(CNT) > 500 AND V(CNT) < 20000 THEN
    RAWNUM = RAWNUM + 1
    FLTR1(RAWNUM) = V(CNT)
    PSUM = PSUM + V(CNT)
  END IF
NEXT CNT
```

**REM CALCULATING PROVISIONAL MEAN, SD & SERROR OF THE DATA FOR
REM SECOND FILTER PROCESS. HERE THE DATA ARE FILTERED TO REMOVE
REM VALUES GREATER THAN ± 3 STANDARD DEVIATIONS OF THE MEAN**

PMEAN = PSUM / RAWNUM

```
FOR CNT = 1 TO RAWNUM
  PSDSUM = PSDSUM + ((FLTR1(CNT) - PMEAN) ^ 2)
NEXT CNT
```

```
PSD = (PSDSUM / (RAWNUM - 1)) ^ .5
PSERROR = PSD / ((RAWNUM) ^ .5)
MINGD = PMEAN - (3 * PSD)
MAXGD = PMEAN + (3 * PSD)
```

REM SECOND DATA FILTER - (+OR- 3SD)

```
FOR CNT = 1 TO RAWNUM
  IF FLTR1(CNT) > MINGD AND FLTR1(CNT) < MAXGD THEN
    NUMGDS = NUMGDS + 1
    SUM = SUM + FLTR1(CNT)
    FLTR2(NUMGDS) = FLTR1(CNT)
    IF FLTR2(NUMGDS) > MAXVAL THEN MAXVAL = FLTR2(NUMGDS)
    IF FLTR2(NUMGDS) < MINVAL THEN MINVAL = FLTR2(NUMGDS)
  END IF
NEXT CNT
```

REM CALCULATING FINAL VALUES OF SD, ERROR, MEAN & SKEW

MEAN = SUM / NUMGDS

```
FOR CNT = 1 TO NUMGDS
  MOMSUM = MOMSUM + ((FLTR2(CNT) - MEAN) ^ 3)
  SDSUM = SDSUM + ((FLTR2(CNT) - MEAN) ^ 2)
NEXT CNT
```

$SD = (SDSUM / (NUMGDS - 1)) ^ .5$
 $ERROR = SD / ((NUMGDS) ^ .5)$
 $THRDMOM = MOMSUM / NUMGDS$
 $SKEW = THRDMOM / (SD ^ 3)$

**REM CALCULATING BIN BOUNDARIES & MIDPOINTS FOR THE FREQUENCY
REM DISTRIBUTION**

```
INCREM = (MAXVAL - MINVAL) / NUMBINS
L1 = MINVAL + INCREM
XMBND(1) = (L1 + MINVAL) / 2
L2 = L1 + INCREM
XMBND(2) = (L1 + L2) / 2
L3 = L2 + INCREM
XMBND(3) = (L2 + L3) / 2
L4 = L3 + INCREM
XMBND(4) = (L3 + L4) / 2
L5 = L4 + INCREM
XMBND(5) = (L4 + L5) / 2
L6 = L5 + INCREM
XMBND(6) = (L5 + L6) / 2
L7 = L6 + INCREM
XMBND(7) = (L6 + L7) / 2
L8 = L7 + INCREM
XMBND(8) = (L7 + L8) / 2
L9 = L8 + INCREM
XMBND(9) = (L8 + L9) / 2
L10 = L9 + INCREM
XMBND(10) = (L9 + L10) / 2
```

```

L11 = L10 + INCREM
XMBND(11) = (L10 + L11) / 2
L12 = L11 + INCREM
XMBND(12) = (L11 + L12) / 2
L13 = L12 + INCREM
XMBND(13) = (L12 + L13) / 2
L14 = L13 + INCREM
XMBND(14) = (L13 + L14) / 2
L15 = L14 + INCREM
XMBND(15) = (L14 + L15) / 2
L16 = L15 + INCREM
XMBND(16) = (L15 + L16) / 2
XMBND(17) = (L16 + MAXVAL) / 2

```

REM CALCULATING FREQUENCY DISTRIBUTION

```

FOR CNT = 1 TO NUMGDS
totl = totl + FLTR2(CNT)
IF FLTR2(CNT) >= MINVAL AND FLTR2(CNT) < L1 THEN EXPY(1) = EXPY(1) + 1
IF FLTR2(CNT) >= L1 AND FLTR2(CNT) < L2 THEN EXPY(2) = EXPY(2) + 1
IF FLTR2(CNT) >= L2 AND FLTR2(CNT) < L3 THEN EXPY(3) = EXPY(3) + 1
IF FLTR2(CNT) >= L3 AND FLTR2(CNT) < L4 THEN EXPY(4) = EXPY(4) + 1
IF FLTR2(CNT) >= L4 AND FLTR2(CNT) < L5 THEN EXPY(5) = EXPY(5) + 1
IF FLTR2(CNT) >= L5 AND FLTR2(CNT) < L6 THEN EXPY(6) = EXPY(6) + 1
IF FLTR2(CNT) >= L6 AND FLTR2(CNT) < L7 THEN EXPY(7) = EXPY(7) + 1
IF FLTR2(CNT) >= L7 AND FLTR2(CNT) < L8 THEN EXPY(8) = EXPY(8) + 1
IF FLTR2(CNT) >= L8 AND FLTR2(CNT) < L9 THEN EXPY(9) = EXPY(9) + 1
IF FLTR2(CNT) >= L9 AND FLTR2(CNT) < L10 THEN EXPY(10) = EXPY(10) + 1
IF FLTR2(CNT) >= L10 AND FLTR2(CNT) < L11 THEN EXPY(11) = EXPY(11) + 1
IF FLTR2(CNT) >= L11 AND FLTR2(CNT) < L12 THEN EXPY(12) = EXPY(12) + 1
IF FLTR2(CNT) >= L12 AND FLTR2(CNT) < L13 THEN EXPY(13) = EXPY(13) + 1
IF FLTR2(CNT) >= L13 AND FLTR2(CNT) < L14 THEN EXPY(14) = EXPY(14) + 1
IF FLTR2(CNT) >= L14 AND FLTR2(CNT) < L15 THEN EXPY(15) = EXPY(15) + 1
IF FLTR2(CNT) >= L15 AND FLTR2(CNT) < L16 THEN EXPY(16) = EXPY(16) + 1
IF FLTR2(CNT) >= L16 AND FLTR2(CNT) <= MAXVAL THEN EXPY(17) = EXPY(17) + 1
NEXT CNT

```

```
CLS
```

REM DISPLAYING CALCULATED PARAMETERS

```

PRINT "NUMBER OF GOOD RESULTS= "; NUMGDS
PRINT "SD= "; SD
PRINT "SERROR= "; SERROR
PRINT "MEAN= "; MEAN
PRINT "SKEW= "; SKEW
MINV = ((2 * 22 * .02) / (7 * .000001 * (MEAN + SERROR)))
MAXV = ((2 * 22 * .02) / (7 * .000001 * (MEAN - SERROR)))
VSERR = ((MAXV - MINV) / 2)
PRINT "VEL ERROR= "; VSERR

```

```
PRINT "VEL= "; ((22 * .02 * 2 / 7) / (MEAN * .000001))
REM CALCULATING NORMAL DISTRIBUTION OF SAME MEAN AND SD AS
REM EXPERIMENT
```

```
FOR CNT = 1 TO 17
```

```
  NRMXP = .5 * (((XMBND(CNT) - MEAN) / SD) ^ 2)
  NRMY(CNT) = ((EXP(-1 * NRMXP)) / (SQR(2 * 3.14159) * SD))
NEXT CNT
```

```
REM SAVING INFORMATION TO DISK
```

```
CNT = 1
WHILE CNT < NUMSAMPS
  PRINT #2, USING "#### "; CNT;
  PRINT #2, USING "#####.## "; V(CNT)
  CNT = CNT + 1
WEND
```

```
CLOSE #2
```

```
FOR CNT = 1 TO 17
  PRINT #3, USING "#####.##"; XMBND(CNT)
  PRINT #4, USING "#####"; EXPY(CNT)
  PRINT #5, USING "##.#####"; NRMY(CNT)
NEXT CNT
CLOSE #3
CLOSE #4
CLOSE #5
```



```

REM*****
REM PROGRAM NAME:      DCONVX.BAS
REM AUTHOR :          ADRIAN CRAVEN
REM DATE LAST MODIFIED: 28/3/1996
REM
REM FUNCTION:  THIS PROGRAM TAKES THE DATA FROM THE ARAYTSTR.BAS
REM            PROGRAM AND CONVERTS IT TO EXCEL TAKES .PT0, .PT1 FILES
REM            CONVERTS THEM TO BINARY, PUTS THEM IN DETECTOR ORDER
REM            AND SAVES THEM AS EXCEL USABLE FILES WITH EXTENSION
REM            .CNF
REM*****

```

REM DEFINING OF ARRAYS AND OTHER VARIABLES

```

DIM SHARED V(1000), W(1000), V1(1000), W1(1000)
DIM SHARED D1(1000), D2(1000), D3(1000), D4(1000), D5(1000), D6(1000), D7(1000)
DIM SHARED D8(1000), D9(1000), D10(1000), D11(1000), D12(1000), D13(1000), D14(1000)
DIM SHARED D15(1000), D16(1000)
DIM SHARED GREADS(1000)
DRIV$ = "E:\PWPROGS\"
EXTIP0$ = ".PT0"
EXTIP1$ = ".PT1"
EXTOP$ = ".CNF"

```

```

D1 = 0: D2 = 0: D3 = 0: D4 = 0: D5 = 0: D6 = 0: D7 = 0: D8 = 0
D9 = 0: D10 = 0: D11 = 0: D12 = 0: D13 = 0: D14 = 0: D15 = 0: D16 = 0
X = 0
CNT = 1
TBIT = 0
DETCNT = 0
SPDCNT = 0
EOBFLG = 0
GD = 0
FLEN = 10.657
IDIST = 23.7

```

```

CLS

```

REM START OF PROGRAM

```

INPUT "TYPE FILENAME TO BE CONVERTED "; N$

REM INPUT "NUMBER OF SAMPLES TAKEN "; SAMP

OP0$ = (DRIV$ + N$ + EXTOP$)
IP0$ = (DRIV$ + N$ + EXTIP0$)
IP1$ = (DRIV$ + N$ + EXTIP1$)

```



```
OPEN IP0$ FOR INPUT AS #1
OPEN IP1$ FOR INPUT AS #2
OPEN OP0$ FOR OUTPUT AS #3
```

```
REM IMPORTING DATA INTO ARRAYS
WHILE CNT < SAMP
```

```
  INPUT #1, S
  INPUT #2, T
  V(CNT) = S
  W(CNT) = T
  CNT = CNT + 1
```

```
WEND
```

```
CLOSE #1
CLOSE #2
```

```
FOR X = 1 TO SAMP
```

```
  V1(X) = V(X)
  W1(X) = W(X)
```

```
NEXT X
```

```
CNT = 1
```

```
REM THIS PART CONVERTS DATA ON ILLUMINATION OF 8 OF THE 16 INDIVIDUAL
REM DETECTORS INTO AN ARRAY OF VALUES TO INDICATE THE STATE OF THE
REM DETECTORS AT EACH SAMPLE.
```

```
WHILE CNT < SAMP
```

```
  IF V(CNT) >= 128 THEN
    D15(CNT) = 1
    V(CNT) = V(CNT) - 128
  END IF
  IF V(CNT) >= 64 THEN
    D13(CNT) = 1
    V(CNT) = V(CNT) - 64
  END IF
  IF V(CNT) >= 32 THEN
    D11(CNT) = 1
    V(CNT) = V(CNT) - 32
  END IF
  IF V(CNT) >= 16 THEN
    D9(CNT) = 1
    V(CNT) = V(CNT) - 16
```

```

END IF
IF V(CNT) >= 8 THEN
  D7(CNT) = 1
  V(CNT) = V(CNT) - 8
END IF
IF V(CNT) >= 4 THEN
  D5(CNT) = 1
  V(CNT) = V(CNT) - 4
END IF
IF V(CNT) >= 2 THEN
  D3(CNT) = 1
  V(CNT) = V(CNT) - 2
END IF
IF V(CNT) = 1 THEN
  D1(CNT) = 1
END IF

```

REM THIS PART CONVERTS DATA ON ILLUMINATION OF 8 OF THE 16 INDIVIDUAL
REM DETECTORS INTO AN ARRAY OF VALUES TO INDICATE THE STATE OF THE
REM DETECTORS AT EACH SAMPLE.

```

IF W(CNT) >= 128 THEN
  D2(CNT) = 1
  W(CNT) = W(CNT) - 128
END IF
IF W(CNT) >= 64 THEN
  D4(CNT) = 1
  W(CNT) = W(CNT) - 64
END IF
IF W(CNT) >= 32 THEN
  D6(CNT) = 1
  W(CNT) = W(CNT) - 32
END IF
IF W(CNT) >= 16 THEN
  D8(CNT) = 1
  W(CNT) = W(CNT) - 16
END IF
IF W(CNT) >= 8 THEN
  D10(CNT) = 1
  W(CNT) = W(CNT) - 8
END IF
IF W(CNT) >= 4 THEN
  D12(CNT) = 1
  W(CNT) = W(CNT) - 4
END IF
IF W(CNT) >= 2 THEN
  D14(CNT) = 1
  W(CNT) = W(CNT) - 2
END IF

```

```

IF W(CNT) = 1 THEN
  D16(CNT) = 1
END IF

PRINT #3, USING "#### "; CNT;
PRINT #3, USING "# "; D1(CNT); D2(CNT); D3(CNT); D4(CNT); D5(CNT); D6(CNT);
PRINT #3, USING "# "; D7(CNT); D8(CNT); D9(CNT); D10(CNT); D11(CNT);
PRINT #3, USING "# "; D12(CNT); D13(CNT); D14(CNT); D15(CNT); D16(CNT)
CNT = CNT + 1

WEND

CLOSE #3
CLOSE

REM HERE THE RESULTS ARE FILTERED TO REMOVE ENTRIES WHERE GREATER
REM THAN ONE DETECTOR WAS ILLUMINATED AT ANY GIVEN TIME
FOR CNT = 1 TO SAMP

  TBIT = 0
  DETCNT = 0
  SPDCNT = 0
  EOBFLG = 0

  IF D1(CNT) = 0 AND D2(CNT) = 0 AND D3(CNT) = 0 AND D4(CNT) = 0 AND D5(CNT) = 0
  AND D6(CNT) = 0 AND D7(CNT) = 0 AND D8(CNT) = 0 AND D9(CNT) = 0 AND
  D10(CNT) = 0 AND D11(CNT) = 0 AND D12(CNT) = 0 AND D13(CNT) = 0 AND D14(CNT)
  = 0 AND D15(CNT) = 0 AND D16(CNT) = 0 THEN TBIT = 1
  END IF

  IF D1(CNT) = 1 THEN
    DETCNT = 1
    SPDCNT = 1
  END IF

  IF D2(CNT) = 1 AND EOBFLG = 0 THEN
    DETCNT = DETCNT + 2
    SPDCNT = SPDCNT + 1
  END IF
  IF D2(CNT) = 1 AND EOBFLG = 1 THEN
    TBIT = 1
  END IF
  IF D2(CNT) = 0 AND D1(CNT) = 1 THEN
    EOBFLG = 1
  END IF

  IF D3(CNT) = 1 AND EOBFLG = 0 THEN
    DETCNT = DETCNT + 3
    SPDCNT = SPDCNT + 1
  END IF

```

```
IF D3(CNT) = 1 AND EOBFLG = 1 THEN
  TBIT = 1
END IF
IF D3(CNT) = 0 AND D2(CNT) = 1 THEN
  EOBFLG = 1
END IF
```

```
IF D4(CNT) = 1 AND EOBFLG = 0 THEN
  DETCNT = DETCNT + 4
  SPDCNT = SPDCNT + 1
END IF
IF D4(CNT) = 1 AND EOBFLG = 1 THEN
  TBIT = 1
END IF
IF D4(CNT) = 0 AND D3(CNT) = 1 THEN
  EOBFLG = 1
END IF
```

```
IF D5(CNT) = 1 AND EOBFLG = 0 THEN
  DETCNT = DETCNT + 5
  SPDCNT = SPDCNT + 1
END IF
IF D5(CNT) = 1 AND EOBFLG = 1 THEN
  TBIT = 1
END IF
IF D5(CNT) = 0 AND D4(CNT) = 1 THEN
  EOBFLG = 1
END IF
```

```
IF D6(CNT) = 1 AND EOBFLG = 0 THEN
  DETCNT = DETCNT + 6
  SPDCNT = SPDCNT + 1
END IF
IF D6(CNT) = 1 AND EOBFLG = 1 THEN
  TBIT = 1
END IF
IF D6(CNT) = 0 AND D5(CNT) = 1 THEN
  EOBFLG = 1
END IF
```

```
IF D7(CNT) = 1 AND EOBFLG = 0 THEN
  DETCNT = DETCNT + 7
  SPDCNT = SPDCNT + 1
END IF
IF D7(CNT) = 1 AND EOBFLG = 1 THEN
  TBIT = 1
END IF
IF D7(CNT) = 0 AND D6(CNT) = 1 THEN
  EOBFLG = 1
END IF
```

IF D8(CNT) = 1 AND EOBFLG = 0 THEN
DETCNT = DETCNT + 8
SPDCNT = SPDCNT + 1
END IF

IF D8(CNT) = 1 AND EOBFLG = 1 THEN
TBIT = 1
END IF
IF D8(CNT) = 0 AND D7(CNT) = 1 THEN
EOBFLG = 1
END IF

IF D9(CNT) = 1 AND EOBFLG = 0 THEN
DETCNT = DETCNT + 9
SPDCNT = SPDCNT + 1
END IF
IF D9(CNT) = 1 AND EOBFLG = 1 THEN
TBIT = 1
END IF
IF D9(CNT) = 0 AND D8(CNT) = 1 THEN
EOBFLG = 1
END IF

IF D10(CNT) = 1 AND EOBFLG = 0 THEN
DETCNT = DETCNT + 10
SPDCNT = SPDCNT + 1
END IF
IF D10(CNT) = 1 AND EOBFLG = 1 THEN
TBIT = 1
END IF
IF D10(CNT) = 0 AND D9(CNT) = 1 THEN
EOBFLG = 1
END IF

IF D11(CNT) = 1 AND EOBFLG = 0 THEN
DETCNT = DETCNT + 11
SPDCNT = SPDCNT + 1
END IF
IF D11(CNT) = 1 AND EOBFLG = 1 THEN
TBIT = 1
END IF
IF D11(CNT) = 0 AND D10(CNT) = 1 THEN
EOBFLG = 1
END IF

IF D12(CNT) = 1 AND EOBFLG = 0 THEN
DETCNT = DETCNT + 12
SPDCNT = SPDCNT + 1
END IF
IF D12(CNT) = 1 AND EOBFLG = 1 THEN


```
TBIT = 1
END IF
IF D12(CNT) = 0 AND D11(CNT) = 1 THEN
  EOBFLG = 1
END IF
```

```
IF D13(CNT) = 1 AND EOBFLG = 0 THEN
  DETCNT = DETCNT + 13
  SPDCNT = SPDCNT + 1
END IF
IF D13(CNT) = 1 AND EOBFLG = 1 THEN
  TBIT = 1
END IF
IF D13(CNT) = 0 AND D12(CNT) = 1 THEN
  EOBFLG = 1
END IF
```

```
IF D14(CNT) = 1 AND EOBFLG = 0 THEN
  DETCNT = DETCNT + 14
  SPDCNT = SPDCNT + 1
END IF
IF D14(CNT) = 1 AND EOBFLG = 1 THEN
  TBIT = 1
END IF
IF D14(CNT) = 0 AND D13(CNT) = 1 THEN
  EOBFLG = 1
END IF
```

```
IF D15(CNT) = 1 AND EOBFLG = 0 THEN
  DETCNT = DETCNT + 15
  SPDCNT = SPDCNT + 1
END IF
IF D15(CNT) = 1 AND EOBFLG = 1 THEN
  TBIT = 1
END IF
IF D15(CNT) = 0 AND D14(CNT) = 1 THEN
  EOBFLG = 1
END IF
```

```
IF D16(CNT) = 1 AND EOBFLG = 0 THEN
  DETCNT = DETCNT + 16
  SPDCNT = SPDCNT + 1
END IF
IF D16(CNT) = 1 AND EOBFLG = 1 THEN
  TBIT = 1
END IF
IF D16(CNT) = 0 AND D15(CNT) = 1 THEN
  EOBFLG = 1
END IF
```

```

IF TBIT = 0 THEN
  GD = GD + 1
REM THE REMAINING FILTERED DATA ARE THEN CONVERTED INTO FIGURES
REM WHICH REPRESENT THE DEVIATION OF THE ARC FROM THE INTENDED
REM RADIUS

```

```

  GREADS(GD) = (FLEN / (IDIST - FLEN)) * ((DETCNT / SPDCNT) - 8.5)
  END IF
  TBIT = 0
NEXT CNT

```

```

FOR X = 1 TO GD
  SUM = SUM + GREADS(X)
NEXT X
AV = SUM / GD

```

```

FOR X = 1 TO GD
  SDSUM = SDSUM + ((GREADS(X) - AV) * (GREADS(X) - AV))
NEXT X

```

```

REM HERE VALUES FOR STANDARD DEVIATION AND STANDARD ERROR ARE
REM CALCULATED AND THE RESULTS DISPLAYED ON SCREEN

```

```

SDEV = SQR(SDSUM / (GD - 1))
ERROR = SDEV / SQR(GD)

```

```

PRINT "MEAN="; AV:
PRINT "SD="; SDEV:
PRINT "STD ERROR="; ERROR:
PRINT "No OF GOOD READINGS="; GD:
INPUT XC
CLS

```

```

REM*****
REM PROGRAM:                KSFITTER
REM AUTHOR:                 ADRIAN CRAVEN
REM DATE LAST MODIFIED:    19 MAY 1997
REM FUNCTION:              THIS PROGRAM TAKES INFORMATION GENERATED
REM                        BY THE DATAANAL.BAS AND ARCTMEX.BAS
REM                        PROGRAMS AND PERFORMS A FITTING ROUTIN
REM                        OBTAIN A VALUE FOR DIFFUDION CONSTANT
REM                        AND VELOCITY
REM
REM*****

```

REM DECLARATION OF SUBROUTINES, VARIABLES ETC.

```

DECLARE SUB FITTER ()
DECLARE SUB KSCHECK ()
DECLARE SUB NORMKS ()
DECLARE SUB GRAPHER ()

```

```

DIM SHARED EXPY(20), FITY(20), NRMV(20), XMBND(20), GSIZEA(3), K(3)
DIM SHARED SD, MEAN, PASSV, PASSK, NUMSTEP, KS, K1PREV, K2PREV, CIRCUMF
DIM SHARED FKS, NUMBINS, NUMPTS, MAXY, GAREA, NFREE, FREE, ANS3$, NKS
DIM SHARED NGAREA, FGAREA, norprob(20), T

```

```

NUMPTS = 17
NUMBINS = 17
NFREE = 16
FREE = NFREE
CIRCUMF = .1257
ANS$ = "Y"
ANS1$ = "Y"
ANS2$ = "Y"
DRIV$ = "c:\Adistuff\Thes_res\"
EXT$ = ".DAT"

```

REM START OF PROGRAM

```

CLS
WHILE ANS2$ = "Y"
  INPUT "Please enter the name of the data file ... "; N$
  CLS
  PRINT "Importing data from disk ..... Please wait"
  FILX$ = (DRIV$ + "X" + N$ + EXT$)
  FIFY$ = (DRIV$ + "Y" + N$ + EXT$)
  FILN$ = (DRIV$ + "N" + N$ + EXT$)
  FILF$ = (DRIV$ + "F" + N$ + EXT$)

```

REM SETTING UP FILES FOR DATA TRANSFER AND IMPORTING THE DATA TO
REM ARRAYS

OPEN FILX\$ FOR INPUT AS #1
OPEN FILY\$ FOR INPUT AS #2
OPEN FILN\$ FOR INPUT AS #3
OPEN FILF\$ FOR OUTPUT AS #4

FOR I = 1 TO NUMPTS
INPUT #1, XMBND(I)
INPUT #2, EXPY(I)
INPUT #3, NRMY(I)
XMBND(I) = XMBND(I) / 1000000
NEXT I

CLOSE #1
CLOSE #2
CLOSE #3

INPUT " ENTER VALUE FOR SD "; SD
INPUT "ENTER VALUE FOR MEAN "; MEAN
SD = SD / 1000000
MEAN = MEAN / 1000000

FOR I = 1 TO NUMPTS
XP = ((-1 * ((XMBND(I) - MEAN) ^ 2)) / (2 * (SD ^ 2)))
NRMY(I) = (1 / (SD * ((2 * 3.14259) ^ .5))) * (EXP(XP))
NEXT I

REM NORMALISING THE DISTRIBUTION DATA

CLS
BINWID = XMBND(2) - XMBND(1)

FOR I = 1 TO (NUMPTS - 1)
GAREA = GAREA + (BINWID * ((EXPY(I + 1) + EXPY(I)) / 2))
NEXT I

FOR I = 1 TO NUMPTS
EXPY(I) = EXPY(I) / GAREA
NEXT I

REM ENTER STARTING POINT FOR VEL AND DIFFUSION CONT.

INPUT "ENTER FIRST GUESS FOR VEL ... "; K(1)
INPUT "ENTER FIRST GUESS AT DIFFUSION CONSTANT ... "; K(2)

REM CALCULATE GRID SIZE

```
GSIZEA(1) = -1 * K(1) / 20
GSIZEA(2) = -1 * K(2) / 50
CLS
```

REM FITTING FOR K & V

```
WHILE ANS1$ = "Y"

FOR J = 1 TO 2
  IF J = 1 THEN
    PASSV = PASSV + 1
  END IF
  IF J = 2 THEN
    PASSK = PASSK + 1
  END IF
  K1PREV = K(1)
  K2PREV = K(2)
  KS = 0
```

REM CALCULATE THE THEORETICAL DISTRIBUTION

```
CALL FITTER
```

REM CALCULATE THE K-S GOODNESS OF FIT FACTOR

```
CALL KSCHECK
KS1 = FKS
NUMSTEP = 0
GSIZE = GSIZEA(J)
```

REM FIND AN AREA OF CHANGING GRADIENT

```
DO
  K(J) = K(J) + GSIZE
  CALL FITTER
  CALL KSCHECK
  KS2 = FKS
  LOOP WHILE (KS1 - KS2) = 0
```

**REM ONCE FOUND GRADIENT CHANGE CHECK IF DIRECTION IS TOWARDS
REM MINIMUM**

```
CLS
IF (KS1 - KS2) < 0 THEN
  GSIZE = GSIZE * -1
  K(J) = K(J) + GSIZE
  CALL FITTER
  SAVE = KS1
  KS1 = KS2
```



```
KS2 = SAVE
END IF
CLS
```

REM INCREMENT OR DECREMENT K AND V UNTIL K-S FACTOR INCREASES

```
DO
  NUMSTEP = NUMSTEP + 1
  K(J) = K(J) + GSIZE
  CALL FITTER
  CALL KSCHECK
  KS3 = FKS
  COND = KS3 - KS2
  IF COND < 0 THEN
    KS1 = KS2
    KS2 = KS3
  END IF
LOOP WHILE COND < 0
CLS
```

REM FIND THE MINIMA OF THE PARABOLA DEFINED BY 3 POINTS

```
DUM1 = KS1 - KS2
DUM2 = KS3 - KS2

IF DUM2 <> 0 THEN
  GSIZE = GSIZE * (1 / (1 + (DUM1) / (DUM2))) + .5)
END IF
```

```
K(J) = K(J) - GSIZE
SIGMA = GSIZEA(J) * SQR(2 / (FREE * (KS3 - 2 * KS2 + KS1)))
```

REM DECREASE THE STEP SIZE ACCORDING TO THE NUMBER OF STEPS TAKEN

```
GSIZEA(J) = GSIZEA(J) * NUMSTEP / 3
CALL FITTER
CALL KSCHECK
KS = FKS
MAXY = 0
```

REM FIND THE MAXIMUM VALUE FROM THE FITTED AND EXP. DISTRIBUTIONS

```
FOR I = 1 TO NUMPTS
  IF EXPY(I) > MAXY THEN
    MAXY = EXPY(I)
  END IF
  IF FITY(I) > MAXY THEN
    MAXY = FITY(I)
  END IF
NEXT I
```

REM CALCULATE THE KS GOODNESS OF FIT FACTOR BETWEEN EXP AND NORMAL

CALL NORMKS
NKS = FKS

REM PLOT THE FUNCTIONS FOR VISUAL CHECK

CALL GRAPHER
NEXT J
CLS
PRINT "DO YOU WISH TO RECALCULATE? "
ANS1\$ = INPUT\$(1)
WEND

REM NORMALISE THE DISTRIBUTIONS

FOR I = 1 TO NUMPTS
XMBND(I) = XMBND(I) * 1000
NEXT I

AREA3 = 0
BINWID = XMBND(2) - XMBND(1)

FOR I = 1 TO (NUMPTS - 1)
AREA3 = AREA3 + ((BINWID * (EXPY(I + 1) + EXPY(I)) / 2))
NEXT I

FOR I = 1 TO NUMPTS
EXPY(I) = EXPY(I) / AREA3
FITY(I) = FITY(I) / AREA3
NRMY(I) = NRMY(I) / AREA3
NEXT I

SD = (K(1) / MEAN) * SD

REM SAVE DATA TO DISK

PRINT #4, USING "##.##;.#####;#.###"; K(1); K(2); SD

FOR I = 1 TO NUMPTS
PRINT #4, USING "##.#####;#.#####;#.#####;#.#####"; XMBND(I); EXPY(I); FITY(I);
NRMY(I)
NEXT I

CLOSE #4

CLS
PRINT "DO YOU WANT ANOTHER GO? "
ANS2\$ = INPUT\$(1)

```
CLS
WEND
```

```
SUB FITTER
```

```
REM SUBROUTINE TO CALCULATE THE FITTED DISTRIBUTION
```

```
FOR I = 1 TO NUMPTS
  ETERM = (((-1 * (K(1) * XMBND(I)) + CIRCUMF) ^ 2) / (4 * K(2) * XMBND(I)))
  FITY(I) = ((K(2) * (XMBND(I) * K(1) + CIRCUMF)) * (EXP(-1 * ETERM))) / (4 *
SQR((3.14159) * (K(2) ^ 3) * (XMBND(I) ^ 3)))
NEXT I
```

```
BINWID = XMBND(2) - XMBND(1)
```

```
END SUB
```

```
SUB GRAPHER
```

```
REM THIS SUBROUTINE DISPLAYS THE EXPERIMENTAL, FITTED AND NORMAL
REM DATA
```

```
SCREEN 9
VIEW (0, 0)-(600, 220)
WINDOW (XMBND(1), 0)-(XMBND(NUMPTS), MAXY)
```

```
REM THIS PLOTS THE EXPERIMENTAL DATA TO SCREEN
```

```
COLOR 4
PSET (XMBND(1), EXPY(1))
```

```
FOR I = 2 TO NUMPTS
  LINE (XMBND(I - 1), EXPY(I - 1))-(XMBND(I), EXPY(I))
NEXT I
```

```
REM THIS PLOTS THE FITTED DATA TO THE SCREEN
```

```
COLOR 9
PSET (XMBND(1), FITY(1))
```

```
FOR I = 2 TO NUMPTS
  LINE (XMBND(I - 1), FITY(I - 1))-(XMBND(I), FITY(I))
NEXT I
```

```
REM THIS PLOTS THE NROMAL DISTRIBUTION TO SCREEN
```

```
COLOR 14
PSET (XMBND(1), NRMV(1))
```

```

FOR I = 2 TO NUMPTS
  LINE (XMBND(I - 1), NRMY(I - 1))-(XMBND(I), NRMY(I))
NEXT I

```

```

REM THIS DISPLAYS THE RELEVANT INFORMATION FOR GOODNESS OF FIT,
REM DIFFUSION CONSTANT AND VELOCITY

```

```

COLOR 7
LOCATE 17, 1
PRINT "PASS No. "; PASSV; "FOR VELOCITY"
PRINT "PASS No. "; PASSK; "FOR DIFFUSION CONSTANT"
PRINT "VELOCITY, V= "; K(1); " CHANGED BY "; (K(1) - K1PREV)
PRINT "DIFFUSION CONSTANT, K= "; K(2); " CHANGED BY "; (K(2) - K2PREV)
PRINT "K-S FACTOR FROM MODEL TO EXP IS "; KS
PRINT "K-S FACTOR FROM NORMAL TO EXP IS "; NKS
COLOR 15
PRINT "          ***** HIT ANY KEY TO CONTINUE *****"
a$ = INPUT$(1)
SCREEN 0

```

```

END SUB

```

```

SUB KSCHECK

```

```

REM THIS SUBROUTINE CALCULATES THE KOLMOGOROV - SMIRNOV PARAMETER
REM BETWEEN DISTRIBUTIONS

```

```

CUMEXPY = 0
CUMFITY = 0
EXPYTOT = 0
FITYTOT = 0
DFIT = 0

```

```

FOR I = 1 TO NUMPTS
  EXPYTOT = EXPYTOT + EXPY(I)
  FITYTOT = FITYTOT + FITY(I)
NEXT I

```

```

REM CALCULATING MAXIMUM DIFFERENCE BETWEEN CUMULATIVE
REM DISTRIBUTIONS

```

```

FOR I = 1 TO NUMPTS
  CUMEXPY = CUMEXPY + (EXPY(I) / EXPYTOT)
  CUMFITY = CUMFITY + (FITY(I) / FITYTOT)
  CUMTST = ABS(CUMFITY - CUMEXPY)

```

```

  IF CUMTST > DFIT THEN
    DFIT = CUMTST
  END IF
NEXT I

```

```
FKS = DFIT  
END SUB
```

```
SUB NORMKS
```

```
REM THIS SUBROUTINE CALCULATES THE KOLMOGOROV - SMIRNOV FACTOR  
REM BETWEEN THE NORMAL AND EXP. DISTRIBUTIONS
```

```
NEXPYTOT = 0  
NNRMYTOT = 0  
NCUMEXPY = 0  
NCUMNRMY = 0  
DNRM = 0
```

```
FOR I = 1 TO NUMPTS  
NEXPYTOT = NEXPYTOT + EXPY(I)  
NNRMYTOT = NNRMYTOT + NRMY(I)  
NEXT I
```

```
FOR I = 1 TO NUMPTS  
NCUMEXPY = NCUMEXPY + (EXPY(I) / NEXPYTOT)  
NCUMNRMY = NCUMNRMY + (NRMY(I) / NNRMYTOT)  
NCUMTST = ABS(NCUMNRMY - NCUMEXPY)
```

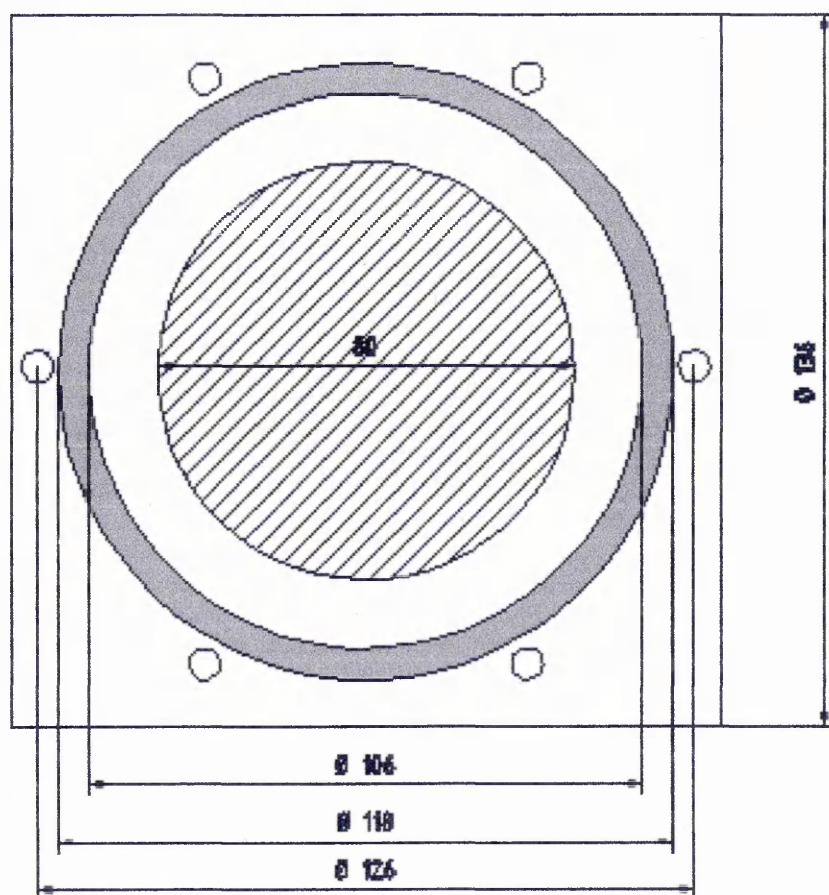
```
IF NCUMTST > DNRM THEN  
DNRM = NCUMTST  
END IF  
NEXT I
```

```
FKS = DNRM  
END SUBUB
```

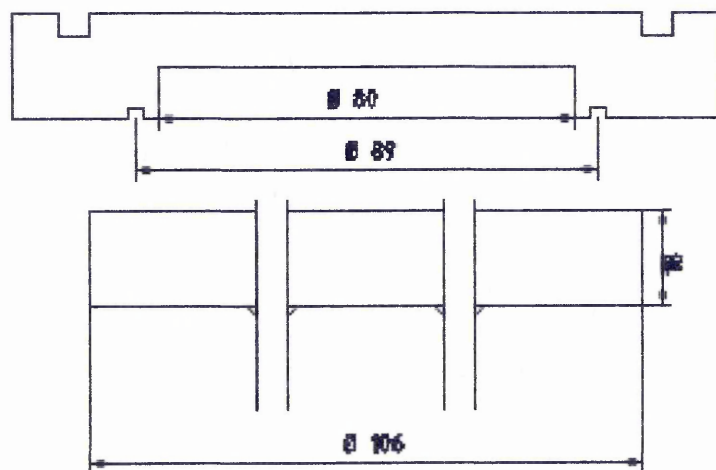

APPENDIX C

DESIGNS FOR ADDITIONAL EQUIPMENT FOR THE VACUUM SYSTEM

Water Cooled Sample Holder Plate

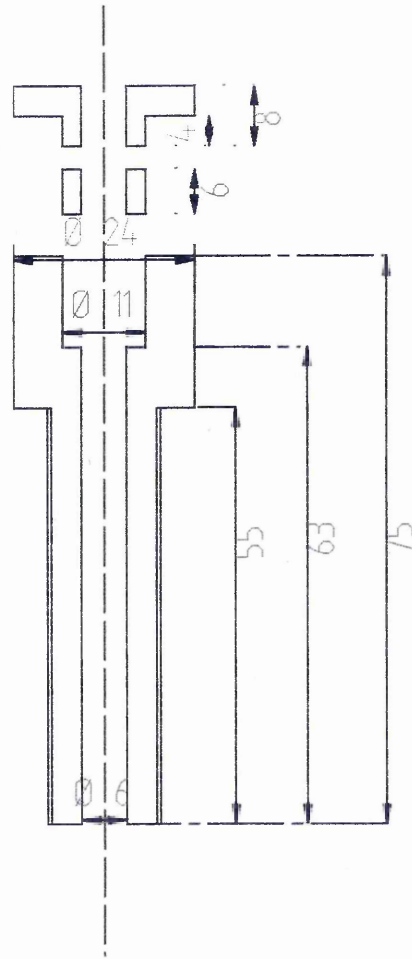


 Indicates material removal on other side



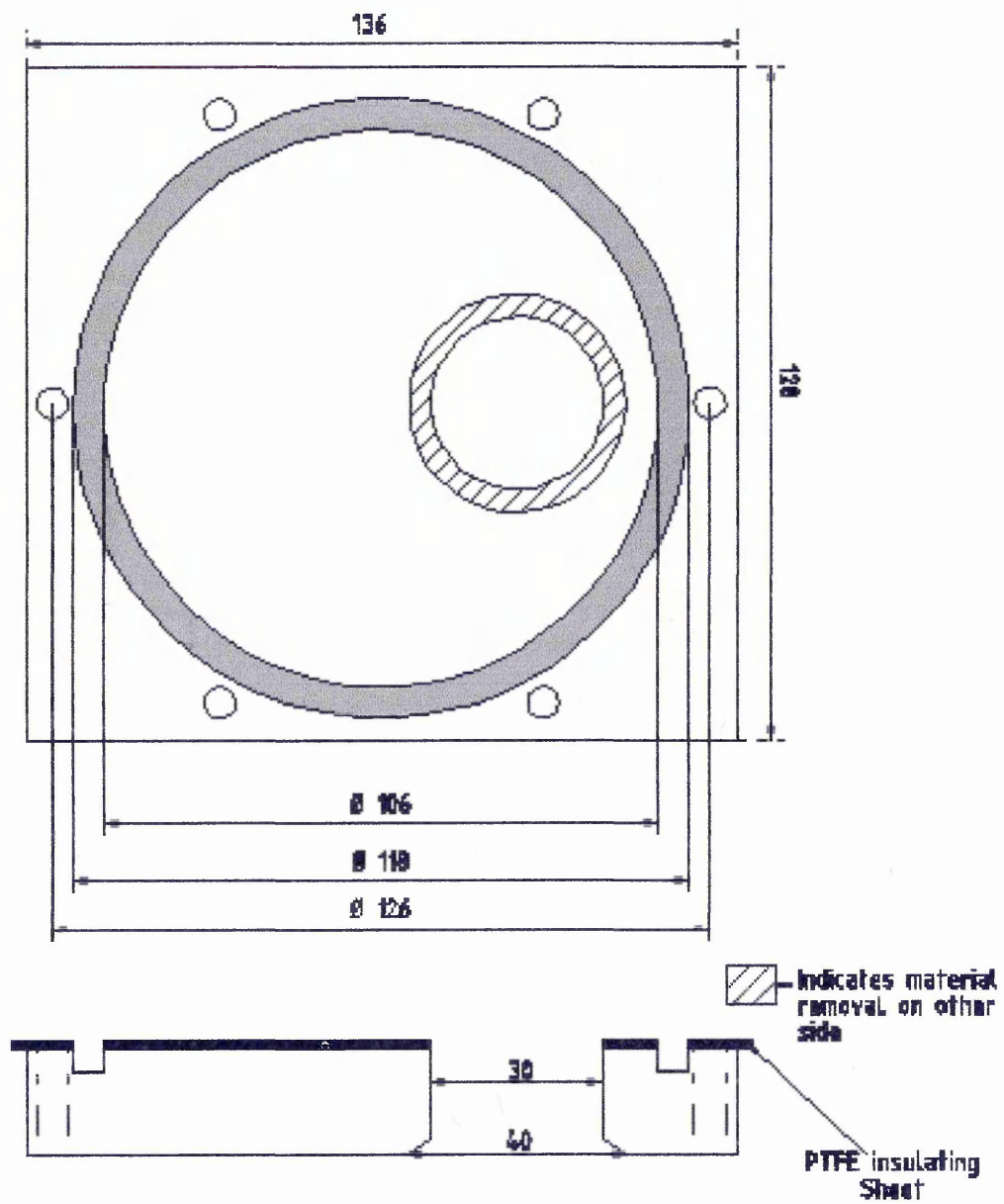
Substrate shield components

Rotational feedthrough



Water Cooled Anode

Anode Holding Plate – Plan and Side View



Complete Anode Assembly – Side View

